# The Effect of the Inter-Layer Time Interval on Selective Laser Melted Inconel 718

---

A Thesis

Presented to

the faculty of the School of Engineering and Applied Science

University of Virginia

---

in partial fulfillment
of the requirements for the degree

Master of Science

by

Bryan M. Koscielny

December 2019

# APPROVAL SHEET

This Thesis
is submitted in partial fulfillment of the requirements
for the degree of
Master of Science

Author Signature: Bryan Koscielny

This Thesis has been read and approved by the examining committee:

Advisor: Dr. James M. Fitz-Gerald

Committee Member: Dr. Ji Ma

Committee Member: Dr. Leonid Zhigilei

Committee Member: Karen Taminger

Committee Member:

Committee Member:

Accepted for the School of Engineering and Applied Science:

Craig H. Benson, School of Engineering and Applied Science

December 2019

# Abstract

The field of metal additive manufacturing (AM) has expanded in the past 10 years with several methods categorized as either fusion-based or solid-state. One of the dominant fusion-based AM methods, termed selective laser melting (SLM), is a powder-bed process that is a current topic of many studies focusing on the process parameters and how they affect the overall build quality. For this research, the alloy of specific interest is Inconel 718 (IN718). This nickel-based superalloy is widely used in high-temperature aerospace applications, such as nozzles, injectors, and other engine components where SLM offers the ability to increase the production efficiency of these complex and precise parts. Utilizing SLM as the production method for IN718 components can potentially allow for fewer manufacturing steps, less assembly, and less material waste, leading to lower costs and lead times. This process also allows for new design complexities that are not possible with traditional manufacturing, such as latticing and internal features. These capabilities have driven immense amounts of research focused on understanding the intricacies of how the SLM process affects IN718 builds.

SLM is a manufacturing method that has a large number of process parameters functioning in parallel, all of which uniquely affect the outcome of the parts produced. Key parameters include laser power, scan speed, layer thickness, and hatch spacing. Due to the broad parameter space and lack of standards, defects are commonly observed. Defects can include porosity, cracking, residual stress, and part distortion, which affect part lifetime and application. One parameter that has received minimal attention is the inter-layer time interval (ILTI). The ILTI is the amount of time it takes for the laser to return to the exact position during the building of consecutive layers, thus relating the role of heat accumulation from layer to layer. The ILTI is not a process input in SLM, since it cannot be programmed into the machine, however it can be influenced by sample geometry, and the number of parts within a build. The broad range of variations makes the impact and understanding of the ILTI complex and difficult to predict. In this research study, the impact of ILTI on a parts overall build quality was investigated. From this research data, the melt pool characteristics, microstructure, texture, and amount of porosity all showed variation, while changes in the composition and hardness were determined to be statistically insignificant. The experiments were designed such that the ILTI varied from 126 to 13 seconds, with the most prominent differences observed from the shortest time interval.

At the shorter intervals, the solidified melt pool structures changed in two aspects. The first is the degree of melt pool staggering. Melt pool staggering is referring to

the horizontal offset that melt pools have with respect to a melt pool in the previous layer. The melt pools exhibited variations in the staggered geometry along with a different shapes based on the ILTIs. Analysis of the results suggest that variations in the melt pool shape are due to changes in the laser beam characteristics from a conduction mode to a transition mode observed in laser welding, along with the keyhole mode. Secondly, the radii of curvature for the melt pools varied within a range of 91 to 131 μm for an ILTI of 126 seconds to a range of 50 to 70 μm at an ILTI of 13 seconds. The lower radius of curvature indicated that the depth-to-width ratio of the melt pool is increasing, consistent with the literature regarding a shift to the transition mode of welding. To investigate the validity of a shift in the laser beam mode, the Eagar-Tsai model for temperature fields produced by a traveling distributed heat source was calculated. The model supported the melt pool shape for the longer ILTIs, but could not accurately predict the melt pool shape for the shortest ILTI (13 seconds). Since the Eagar-Tsai model is limited to application of the conduction mode of welding, the results suggest that at shorter ILTIs, the behavior of the melt pools is more consistent with the transition mode of operation. This change of energy/penetration beam mode could also explain the why the amount of sample porosity increased as the ILTIs decreased. The average area density of porosity, as measured by x-ray computed tomography (XCT) and image analysis, ranged from 0.15 $mm^{-2}$ to 0.29 $mm^{-2}$ as a function of decreasing ILTI.

Optical and electron microscopy along with electron backscatter diffraction (EBSD) analysis showed that the grain structure is well organized in the 13 second ILTI regions. This grain structure consists of 30 μm wide grains spaced 120 μm apart, extending up the centerlines of the melt pools, with larger grains taking up the spaces between. Both grain types showed evidence of growth through multiple build layers, as opposed to the nucleation of new grains at the melt pool interface, which was observed in the longer ILTI regions. The results suggest that the epitaxial growth through multiple build layers is due to the increased depth of penetration, minimal melt pool staggering, and higher temperatures. Consistent with changes in the melt pool alignment and geometry, the crystallographic texture of the samples was found to strengthen in the reduced time interval regions. Analysis of the EBSD data showed that the two distinct grain types dominate the texture. The stronger of the two is a Goss texture, $\{110\} < 001 >$, oriented in the build direction, found in the wider to the two grain types. The weaker component was a cubic texture, $\{100\} < 001 >$, oriented in the build direction, found in the other of the two grain types. There was a strengthening of texture observed, where longer ILTIs had a maximum multiple of

uniform density (MUD) value of roughly 6, and the 13 second ILTI had a maximum MUD value of roughly 9. The change in the MUD values were attributed to a reduction in melt pool staggering and increased remelt of the previous layer, which both affect the directionality of the thermal gradients and solidification.

From this research, it is clear that the inter-layer time interval is a process input that will affect the overall quality of a SLM deposit in terms of grain morphology, texture, and porosity. For this reason, it should be a topic for further investigation including a more detailed evaluation of the mechanical properties, corrosion performance, fatigue response, and precipitate phases.

# Acknowledgements

First I would like to thank my advisor, Dr. Jim Fitz-Gerald, for his endless guidance regarding my research and providing me with the tools to grow and succeed as a scientist. Being a distance student it can be tough to have regular meetings and advisor input, but Professor Fitz-Gerald always found time to get regular updates from me and answer all of my questions.

I would also like to thank my two faculty committee members, Dr. Ji Ma and Dr. Leonid Zhigilei, for dedicating their time and support and offering valuable advice and insight into my research and thesis.

I would like to thank the NASA Langley Research Center and the National Institute of Aerospace for providing me with the opportunity to pursue my graduate education while performing my research along side NASA scientists and engineers. I would like to specifically thank the Additive Manufacturing Structural Integrity Initiative (AMSII), under which my research was funded.

I would like to thank the entire metals group within the Advanced Materials and Processing Branch at NASA Langley for all of their support during my masters research. I would like to specifically thank Karen Taminger who was my mentor/advisor at NASA, who provided me with endless guidance regarding my research along side Dr. Fit-Gerald. I would also like to thank the technicians that helped with everything that had to do with material characterization. Whether that was teaching me how to polish and etch, or how to use a certain microscope, these individuals were valuable resources.

I would also like to thank my two office-mates and fellow graduate students, Cecilia Mulvaney and Libby Urig. Both of their support throughout my graduate education was much needed and definitely appreciated. Not only were they there to bounce research ideas off of, but they were always there for a friendly conversation when I needed a break.

Lastly, I would like to thank my family and friends for all of their love and support throughout this challenging time in my life.

# Contents

# List of Figures

# List of Tables

# Chapter 1

# Introduction

## 1.1 Overall Project Description

This research is part of a NASA project called the Additive Manufacturing Structural Integrity Initiative (AMSII), which is a four-center effort that is split between the Marshall Space Flight Center (MSFC), Langley Research Center (LaRC), Glenn Research Center (GRC), and Ames Research Center (ARC) with the overall goal of developing necessary standards that allow the certification of SLM components intended for human spaceflight. The primary focus in this specific project is on Inconel 718 (IN718), since its high temperature characteristics make it a great candidate for certain spacecraft hardware, such as rocket nozzles, injectors, and other complex shaped engine components [1].

The role of the work being performed at LaRC is mainly in the area of defect characterization. With the use of Non-Destructive Evaluation (NDE), in-process monitoring, and metallurgical analysis, the characteristic types and locations of defects that occur during the SLM process are being studied. Ultimately, the ability to correlate defects to experimental data will be crucial to the development of in-process detection in future additive manufacturing processes.

## 1.2 Motivation

With the approaching possibility of commercial space launches and the plan to send humans to the moon and Mars, the need to find solutions for lower cost spacecraft hardware is extremely important. Additive manufacturing provides an avenue

to achieve large amounts of cost savings due to its net shape or near-net shape capabilities, and the ability to create more complex parts. Since higher part complexity is achievable, current hardware that used to be made in multiple pieces and processes can be made all in one. This reduces time in both the manufacturing and assembly of the hardware. Cost savings becomes even greater when it comes to materials like Inconel and Titanium since these are difficult to form or machine. A deeper understanding of additive manufacturing is needed in order to certify these parts for spaceflight and begin to reap these benefits. While the specific motivation of this project is for spaceflight, this research can be applied to many other industries that have the potential to benefit from additive manufacturing.

## 1.3 Thesis Focus

The overall goal of this research is to develop a better understanding of defects that arise while printing IN718. In order to certify SLM parts in the future, these common defects need to be well studied so that they can be avoided or corrected. Once these defects are identified and understood, routes of detection, rejection, and possibly prevention of these defects can be developed. Experiments were designed in order to look at different macroscopic defects that arise in the SLM process, exploiting common occurrences that can be seen in the printing of a complex part. This research has mainly focused on the inter-layer time interval, which is the time between build layers in the SLM process. A better understanding of this topic directly works towards the eventual certification of IN718 parts built by SLM.

# Chapter 2

# Background

## 2.1 Nickel-Based Superalloys

The need for Nickel-based superalloys came about around the 1950's when turbine engine designers were limited by the temperature constraints of stainless steels [2]. Being able to run these engines at higher temperatures increases their overall efficiency, therefore a need for a new high temperature alloy was evident. Today, nickel-based superalloys are still used in a wide variety of industries and are well known for their high temperature strength, toughness, and resistance to degradation in corrosive or oxidizing environments [3].

Nickel-based superalloys are made up primarily of face-centered cubic (FCC) Ni, however many of these alloys contain up to 40 wt% of elemental additions [3]. These elemental additions all play a role in the phase generation within a specific alloy, and in turn, its mechanical properties. The majority of the Ni forms an austenitic $\gamma$ matrix and these additions are either solid-solution strengtheners or precipitate out to be coherent or incoherent to the matrix. A more detailed description of each of the alloying elements' effects on the microstructure is shown in Table 2.1 [4].

Throughout the years, improvements were made to these alloys. The addition of significant amounts of Fe brought about nickel-iron-based superalloys, which are led by the commonly used alloy, IN718. The standard composition of IN718 is given in Table 2.2. Now instead of being $\gamma$' strengthened, these iron-nickel-based alloys are primarily $\gamma$" strengthened [2]. While this change limits the alloy to a lower operating temperature of about 650°C, the significant amount of Fe lowers the manufacturing cost considerably [5]. Even with the fact that IN718 is limited to a lower operating

Table 2.1: Alloying element effects for nickel-based superalloys. [4]

| **Element** | **Effects** |
|---|---|
| Cr | Solid-solution strengthener, $M_7C_3$ and $M_{23}C_6$ carbide former, improve oxidation and hot corrosion resistance |
| Co | Solid-solution strengthener, raises solvus temperature of $\gamma$' $Ni_3$(Al,Ti) |
| Al | Strengthening phase $\gamma$' $Ni_3$(Al,Ti) former, improve oxidation and hot corrosion resistance |
| Ti | Strengthening phase $\gamma$' $Ni_3$(Al,Ti) former |
| Nb | Strengthening phase $\gamma$" $Ni_3Nb$ former, MC and $M_6C$ carbide former |
| Fe | Solid-solution strengthener |
| Mo | Solid-solution strengthener, MC, $M_{23}C_6$ and $M_6C$ carbide former |
| W | Solid-solution strengthener, MC, $M_{23}C_6$ and $M_6C$ carbide former |
| Ta | Solid-solution strengthener, MC carbide former, improve creep properties |
| Re | Solid-solution strengthener, retard $\gamma$' coarsening |
| C | M(C,N) carbonitrides former, grain-boundary strengthener |
| N | M(C,N) carbonitrides former |
| B | Grain-boundary strengthener, improve creep properties and rupture strength |

temperature, it is still used in a wide variety of applications. Its initial use at Pratt and Whitney in 1963 was for the diffuser case of the J58 engine in the SR-71 Blackbird, and now it is one of the most widely used nickel alloys in jet engines [6].

While many of the phases in Table 2.1 are present in IN718, there are also additional phases that arise with this alloy system. The main secondary phases observed in IN718 are $\gamma$', $\gamma$", $\delta$, Laves, and MC carbides. These phases' crystal structures, lattice parameters, formulas, and appearances are summarized in Table 2.3. IN718 is primarily strengthened by $\gamma$' and $\gamma$" which both precipitate coherently into the $\gamma$ matrix. $\gamma$' forms when Ni reacts with either Al or Ti. $\gamma$" forms when Ni and Nb combine, providing very high strength at low to intermediate temperatures. $\gamma$" is metastable and becomes unstable at temperatures above 650°C, limiting this alloy's maximum operating temperature. Above 650°C, $\delta$ precipitates of the same composition ($Ni_3Nb$) form, reducing the amount of $\gamma$". The $\delta$ phase is incoherent and is deleterious to the materials strength at large quantities. However, small amounts can be used to control and refine grain size. Carbides come from the reaction between C and Ti or Nb. These can either form on grain boundaries, strengthening and preventing their motion; precipitate in the matrix, improving strength; or tie up other elements that would otherwise promote phase instability, such as Laves precipitates

Table 2.2: Standard compositional ranges for Inconel 718. [7]

| **Element** | **Weight Percent [wt%]** |
|---|---|
| Ni + Co | 50.0 - 55.0 |
| Cr | 17.0 - 21.0 |
| Nb | 4.75 - 5.50 |
| Mo | 2.80 - 3.30 |
| Ti | 0.65 - 1.15 |
| Al | 0.20 - 0.80 |
| Co | 1.00 max |
| C | 0.08 max |
| Mn | 0.35 max |
| Si | 0.35 max |
| P | 0.015 |
| S | 0.015 |
| B | 0.006 |
| Cu | 0.30 max |
| Fe | balance |

that form when Fe reacts with either Nb, Ti, or Mo, causing lowered rupture strength and ductility [4].

As stated before, Nickel-based superalloys have great high temperature mechanical properties. At room temperature IN718 has a tensile strength of 180 ksi, a yield strength of 150 ksi, and an elongation of 12 percent [8]. These properties exhibit very little change as temperature increases as shown in Figure 2.1. Figure 2.1a and 2.1b show the effect of temperature on the tensile ultimate and yield strength of wrought IN718, respectively. It can be seen that both properties remain relatively unchanged from room temperature to 540°C (approx. 1000°F), and the steep drop off doesn't occur until about 650°C (approx. 1200°F). As mentioned before, at 650°C the $\gamma$" phase becomes unstable and $\delta$ begins to form, hence the drop in mechanical properties.

Superalloys are currently processed in several different ways. Pollock and Tin [3] sum these up well. Superalloys are mainly used in cast, directionally solidified, and wrought forms. Each of these have their benefits and limitations. Cast alloys allow the manufacturing of more complex geometries, and directionally solidified alloys are able to control grain orientation or be made as a single crystal to increase mechanical properties. Machining is another option for shaping superalloys, but many are deemed to be difficult-to-machine because of their high strength, tendency to harden during machining, and low thermal conductivity, leading to increased tool wear [10].

Table 2.3: Common secondary phases found in IN718. [4]

| **Phase** | **Crystal Structure** | **Lattice Parameter [nm]** | **Formula** | **Appearance** |
|---|---|---|---|---|
| $\gamma$' | FCC (ordered $L1_2$) | 0.3561 for pure $Ni_3Al$ to 0.3568 for $Ni_3(Al_{0.5}Ti_{0.5})$ | $Ni_3$(Al,Ti) | Coherent spherical particles |
| $\gamma$" | BCT (ordered $D0_{22}$) | $a_0$=0.3624 $c_0$=0.7406 | $Ni_3Nb$ | Coherent disk-shaped particles |
| $\delta$ | Orthorhombic (ordered $Cu_3Ti$) | $a_0$=0.5106-0.511 $b_0$=0.421-0.4251 $c_0$=0.452-0.4556 | $Ni_3Nb$ | Incoherent Acicular shaped particles |
| MC Carbide | Cubic | $a_0$=0.430-0.470 | (Ti,Nb)C | Globular, irregularly shaped particles that are grey to lavender |
| Laves | Hexagonal | $a_0$=0.475-0.495 $c_0$=0.770-0.815 | $Fe_2Nb$ $Fe_2Ti$ $Fe_2Mo$ | Irregularly shaped globules, often elongated, or as platelets |

## 2.2 Additive Manufacturing

Dating back to the late 1980s, additive manufacturing (AM) has developed into an immense suite of technologies that are currently changing the way design and manufacturing is viewed [11]. Additive manufacturing is defined by ASTM as the "process of joining materials to make parts from 3D model data, usually layer upon layer, as opposed to subtractive manufacturing and formative manufacturing methodologies" [12]. This layer by layer manufacturing opens new doors to what can be designed and successfully made. When compared to traditional subtractive manufacturing, AM has the potential to reduce waste, reduce lead time and cost, and give the ability to design products with complex and intricate features [13]. One example of these complex geometries that are made possible with AM is a copper rocket nozzle made by NASA. As seen in Figure 2.2, the rocket nozzle has more than 200 channels built into its wall for regenerative cooling of the nozzle in its extreme environment [14]. This exact design would be impossible to make if it weren't for AM. There is no

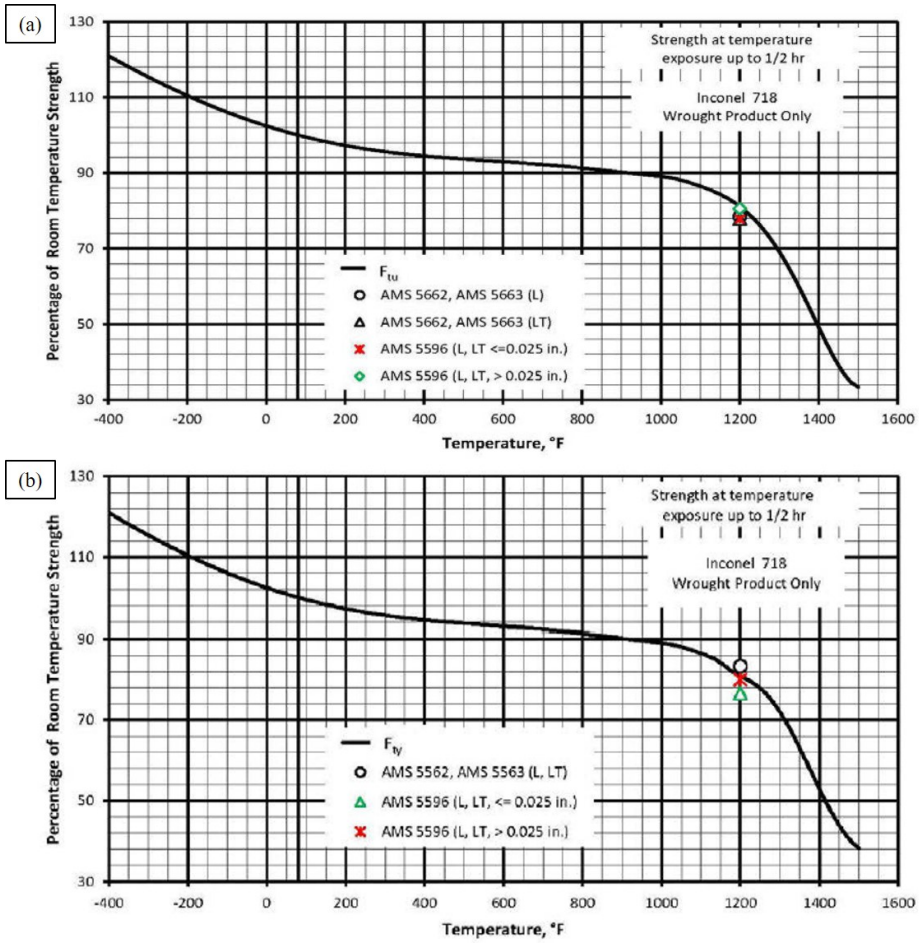


Figure 2.1: The effect of temperature on mechanical properties of wrought Inconel 718 [9], where (a) is the effect of temperature on the tensile ultimate strength and (b) is the effect on the tensile yield strength.

tooling or processing that would be able to machine those channels, and they would be too small and intricate for casting. Other than the cooling channels, AM provides other benefits for manufacturing this part, such as reduced waste. Starting from a large piece of copper round stock, subtractive manufacturing methods would need to remove a lot of material that would go to waste. AM on the other hand can selectively solidify the powder feed stock, and the non-solidified powder can essentially be used in the next build, greatly reducing waste.

These benefits and many more are the reasons why many different industries are becoming very interested in AM. Two industries that are currently using AM technologies are the aerospace and medical industries. GE Aviation has fully introduced 3-D printed fuel nozzle tips for their LEAP engines. As seen in Figure 2.3, the additively maufactured fuel nozzle tip, designated by the red arrow, was reduced from

Figure 2.2: 3-D printed copper rocket nozzle made at NASA Marshall Space Flight Center. [14]

20 pieces previously welded together to one single piece, which resulted in a weight savings of about 25 percent [15]. This reduction in the number of parts is another major benefit of AM. This reduces the amount of assembly, which in turn saves time, money, and resources.

The medical industry has been using AM to produce intricate porous orthopedic implants that help with bone ingrowth [16]. An example of these orthopedic implants is shown in Figure 2.4. Additively manufactured orthopedic implants have been around for more than a decade now and benefit mainly from the ability to easily create porous structures and the ability to customize the implants for specific patients [17].

The broad definition of AM provided above encompasses many different processes that can be first separated into two categories relating to metal AM, fusion-based AM and solid-state AM. This classification is made based on the processes' temperatures. Fusion-based processes reach temperatures above the material's melting temperature, while solid-state processes do not. Two popular solid-state processes today are Additive Friction Stir (AFS) and Ultrasonic Additive Manufacturing (UAM). UAM is said to operate between 30-50 percent of the material's melting temperature [18, 19]. While solid-state technologies are emerging in today's industry, the focus of this review will be on fusion-based AM processes.

Figure 2.3: GE Aviation LEAP engine fuel nozzle produced out of a CoCr alloy using selective laser melting. [15]

### 2.2.1 Fusion-Based AM Processes

Fusion-based additive manufacturing, as mentioned before, is performed at temperatures above the material's melting temperature in order to fuse the layers together. There are many different fusion-based AM processes that can be split up between powder bed, powder feed and wire feed processes [20]. The two main powder bed processes are Selective Laser Melting (SLM) and Electron Beam Melting (EBM). The main powder feed process is called Laser Engineered Net Shaping (LENS). Lastly two popular wire feed processes are Wire and Arc Additive Manufacturing (WAAM) and Electron Beam Free Form Fabrication ($EBF^3$), also known as Electron Beam Additive Manufacturing (EBAM). Each of these processes have either a laser, an arc, or an electron beam energy source. Typically wire feed and powder feed processes have a higher deposition rate and are more near-net-shape as opposed to net-shape, while powder bed processes have lower deposition rates, but are more accurate requiring little to no post-print machining. Powder bed processes are known to have finer detail and more precise due to their small spot size energy sources and smaller melt pools.

### 2.2.2 Selective Laser Melting Process

Selective Laser Melting (SLM) is a powder bed fusion process that uses a high intensity laser to melt and consolidate the powder on a layer by layer basis with

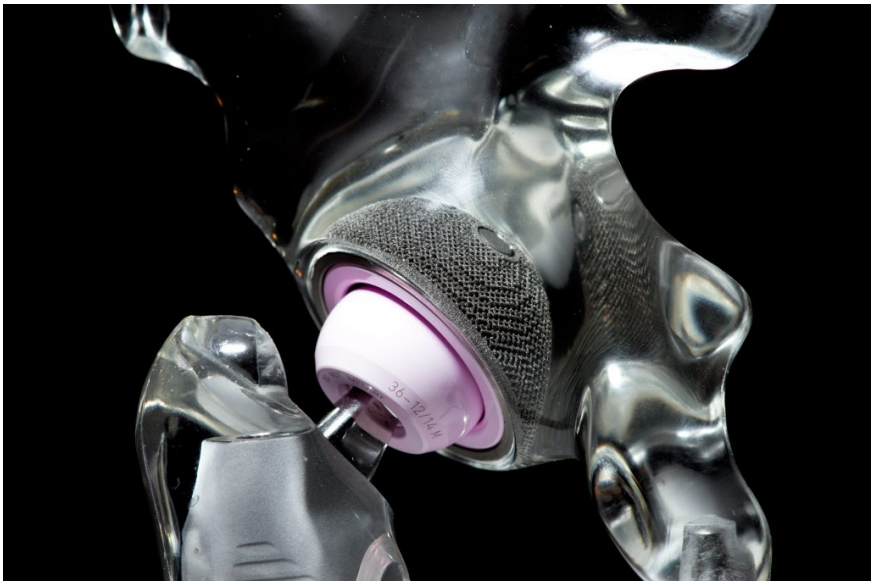

Figure 2.4: Additively manufactured (Electron Beam Melting) hip implant made out of titanium with a porous surface for bone ingrowth. [17]

reference to computer aided design (CAD) data [13]. This process is arguably the most developed and widely used of the metal AM technologies [21]. Figure 2.5 shows a schematic of the SLM process. The process starts with a thin layer of metal powder spread over a baseplate. The laser is then scanned over the powder layer to melt specific areas of the powder bed in accordance to the CAD data. When the laser is finished, the build plate moves down by an increment equal to the layer thickness, and a new powder layer is spread by the recoating system. Recoating systems can vary from machine to machine but they all work in a similar way, pushing powder onto the build plate and spreading it to form an even layer. When there is left over powder after, it is swept into powder overflow containers for future use. Once a new layer of powder is evenly spread, the laser scans the next layer and this process is repeated continuously until the desired part is completed.

### Process Inputs

In SLM there are many different process inputs that all play a role in the overall quality of the final build, including laser power, scan speed, hatch spacing, layer thickness, scan strategy, size and shape of powder, build atmosphere, build layout etc. All of these inputs have an effect on the output, which is the final part. The effect of each of these parameters needs to be fully understood in order to eventually certify SLM for industry use. Many of these parameters and their effects on the final

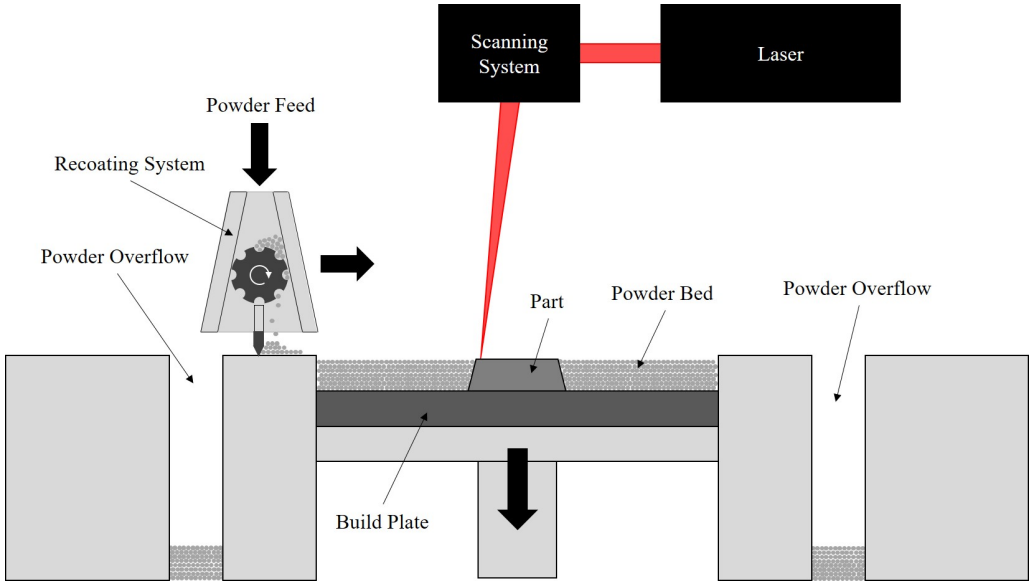


Figure 2.5: SLM system schematic modeled after SLM Solutions' machines.

build have been topics of research over the past few years.

**Laser energy density** is a metric that combines laser power, scan speed, hatch spacing, and layer thickness into one single parameter. This parameter has been widely used in recent research studies [22, 23] and is calculated using Equation 2.2.1,

$$E = \frac{P}{vht} \tag{2.2.1}$$

where $E$ is the laser energy density in J/mm$^3$, $P$ is the laser power in watts, $v$ is the laser scan speed in mm/sec, $h$ is the hatch spacing between adjacent scan tracks in millimeters, and $t$ is the layer thickness in millimeters. This parameter is often referred to as the volumetric energy density (VED) and expresses the amount of energy delivered per unit volume of powder [24]. Other studies use the same formula, however instead of using the hatch spacing, they replace it with the laser spot size measured in millimeters [25].

Yakout et al. explored the effect of laser energy density on the final part quality, focusing on Invar 36 [22]. In this study they produced 225 cubes that all varied in laser powder, scan speed, and hatch spacing. From this study they found that parts built with extremely high or extremely low laser energy densities cause major issues with the recoating system. These parts would hit the reocater blade as it passed over, causing vibration to occur and uneven powder layers to be produced. After these troublesome parts were removed from the study it was found that as laser energy density increases, the part density increases as shown in Figure 2.6. However, at a

certain point parts began to show signs of over melting and distortion. It was shown that the optimal laser energy density for Invar 36 was between 60-75 J/mm$^3$.

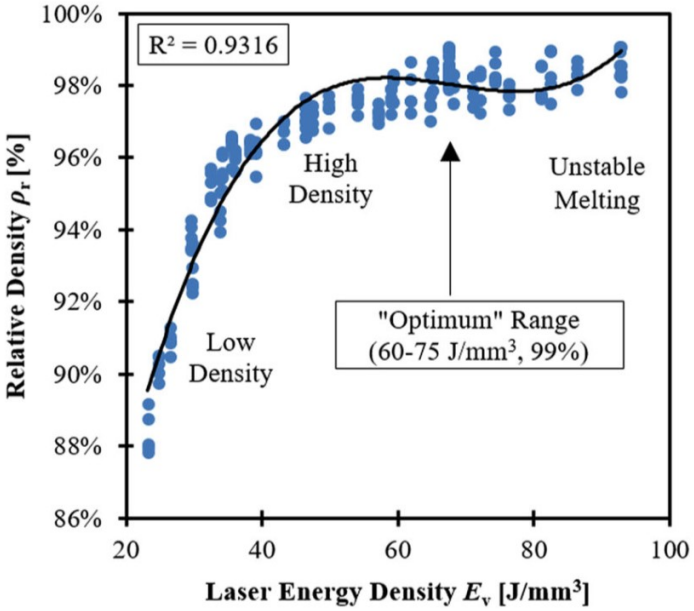


Figure 2.6: The effect of laser energy density on the part's relative density. [22]

Jia and Gu explored the effect of linear laser energy density on SLM Inconel 718 [26]. Linear laser energy density is similar to the parameter discussed above, but only takes into account the laser power and scan speed. In this study, four different linear laser energy densities were used; 180 J/m, 275 J/m, 300 J/m, and 330 J/m. It was found that with increasing linear laser energy density the phases, relative density of the part, microhardness, wear resistance, and oxidation resistance all were affected. X-ray diffraction (XRD) results showed that as the linear laser energy density increased, both $\gamma$ and $\gamma$' intensities were decreased and the peaks were broadened. Relative density measurements showed a decrease in porosity levels as the linear laser energy density increased, obtaining a maximum relative density of 98.4 percent at 330 J/m. Microhardness was also shown to increased from 331.9 $HV_{0.2}$ to 395.8 $HV_{0.2}$ as the linear laser energy density was increased from 180 J/m to 330 J/m. Along with these changes, as the energy density increased, both the wear resistance and oxidation resistance increased.

Another similar parameter called power density, usually measured in MW/cm$^2$, has influence on the mode of welding that occurs during the SLM process. In laser welding there are three modes that change the shape and stability of the melt pool. The modes are conduction, transition, and keyhole mode. Assuncao et al. show how

the power density affects the mode of welding as well as the depth-to-width ratio of the melt pool [27] for the different modes.

While the effects of laser energy density can be material dependent, it is clear that the effects are present and can play a major role in the overall quality of final parts built through SLM. However, this parameter may not give all the neccessary information to describe the cause of the build quality. Bertoli et al. show that the laser energy density is a thermodynamic quantity and is not able to capture some of the complex physics that take place in the SLM process [24].

**Scan strategy** is another very important process input that can dramatically affect the quality of the final part. Scan strategy is the term used to describe the path at which the laser scans the powder. Popular scan strategies that are used in many machines today are 'stripes' patterns, 'chessboard' or 'island' patterns, and 'back and forth' patterns. Each of these scan strategies are depicted in Figure 2.7. The effect of different scan strategies on the final part in SLM has been a topic of research in the past [28, 29, 30, 31, 32].

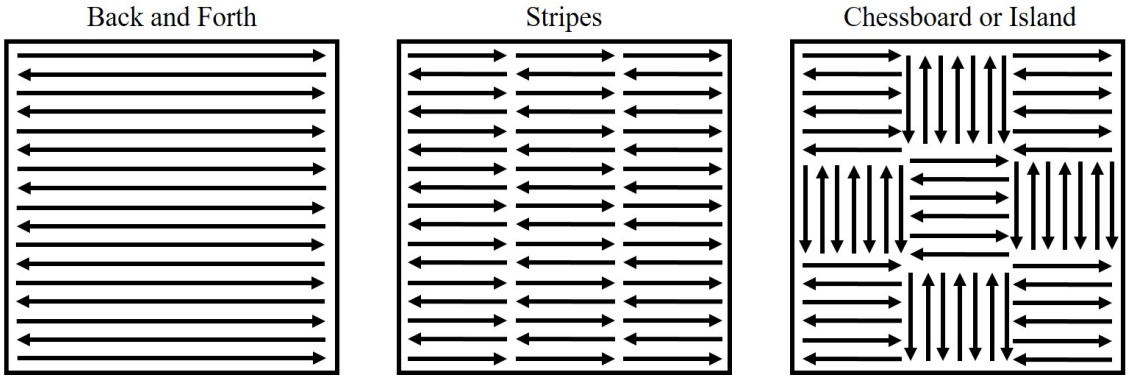


Figure 2.7: Schematic of various scan strategies that are commonly used. Each of these scan strategies can have some sort of rotation or translation from layer to layer to avoid scan track overlap.

Carter et al. investigated the effect of differing scan strategies on the microstructure of SLM CM247LC, a nickel superalloy [28]. For this study they used two different scan strategies; the 'island' scan strategy and a 'back and forth' scan strategy. The 'island' scan strategy takes a two dimensional slice of the part and divides it into squares forming a chessboard pattern. An island size of 5 mm was used. For each subsequent layer the island pattern was shifted by 1 mm in both the x and y-directions and the whole pattern is rotated 45 degrees. The 'back and forth' scan strategy consisted of scan tracks that spanned the entire width of the part and was unchanged from layer to layer. They concluded that the 'island' scan strategy resulted in a 1 mm repeating

square pattern of fine grained regions caused by the island shift after every layer. These fine grained regions were surrounded by columnar grain regions, resulting in a bimodal grain structure. They show that electron backscatter diffraction (EBSD) results indicate that there is a bimodal texture as well. They also concluded that the 'back and forth' scan strategy produces a much more homogeneous grain structure with larger columnar grains. This demonstrates that changes in scan strategy can have dramatic effects on the microstructure of the final build.

Lu et al. also investigated the island scan strategy, but in this study they explored the effects of changing the island size using Inconel 718 [29]. Island sizes of 2 mm, 3 mm, 5 mm, and 7 mm were used. They found that the 5 mm and 7 mm islands resulted in the best relative density, and that severe cracking occurred in the 2 mm island specimen. It was also found that residual stress in the specimens were as follows: 2 mm $<$ 5 mm $<$ 7 mm $<$ 3 mm; however the 2 mm specimen likely had the lowest residual stress due to relief from cracking. Lastly, they concluded that ultimate tensile strength and yield strength were similar from specimen to specimen, however there was a change in elongation, likely due to differing levels of porosity. In addition to its effects on microstructure shown by Carter et al., scan strategy also has an effect on porosity and residual stress.

Mancisidor et al. explored the cause of residual porosity even with optimized parameters using both the 'island' scan strategy and a 'stripes' scan strategy [30]. In both of these scan strategies the laser has to change directions many times requiring the laser to start and stop its motion. When this happens the laser needs to accelerate and decelerate. Looking back at Equation 2.2.1, as the scan speed of the laser is decreased, the laser energy density increases dramatically. At these extremely high laser energy densities, keyhole melt pools can form and resulting material evaporation is thought to occur causing pores to form. In this study they correlated residual porosity to the starts and stops of the laser in both scan strategies. For the 'island' scan strategy, porosity was observed at the borders of the islands themselves, meaning porosity was both at the edges of the part as well as in the bulk. For the 'stripes' scan strategy, porosity was only observed at the edges of the part since this scan strategy consisted of scan tracks that stretched the width of the part. They go on to show that a function called skywriting reduces this porosity by never stopping the laser motion. Instead of stopping and starting to change directions, the laser would turn off at the end of the scan track, make a loop to the next adjacent scan track, and then turn back on once desired scan speed was reached. This ensures that the entire part is scanned with the exact same scan speed and the laser energy density

does not reach extremely high values. This study shows that porosity can occur in SLM simply based on the scan strategy chosen and not on the processing parameters themselves. It also highlights one way that scan strategies can be modified in the future to make better quality final parts.

There has also been research done showing the effect that scan strategy has on the material's texture. Both Geiger et al. [31] and Sun et al. [32] explore how the different scanning rotations affect the texture formation in two different material systems; IN738LC and Ni-25 at.%Mo, respectively. Rotating the scan strategy from layer to layer is very common in order to prevent scan tracks from being directly on top of one another. Both studies showed that texture control is possible by changing from no sample rotation to rotating a certain amount after each layer. This strong texture was shown by different Young's moduli measured in the principal directions [31].

Overall, research has shown that the scan strategy used in SLM affects many different aspects of the final build. In order to fully understand the SLM process in an effort increase its repeatability and reliability, developing and optimizing scan strategies will be extremely important.

**Powder** characteristics or powder quality is another process input that plays a large role in the outcome of the SLM build. These characteristics include particle size, size distribution, shape, surface morphology, and internal porosity. Figure 2.8 shows some of these powder defects that are of interest when characterizing powders for SLM. Understanding how these characteristics affect SLM builds has been a large topic of research in order to reduce the occurrence of defects and work towards high quality SLM builds.

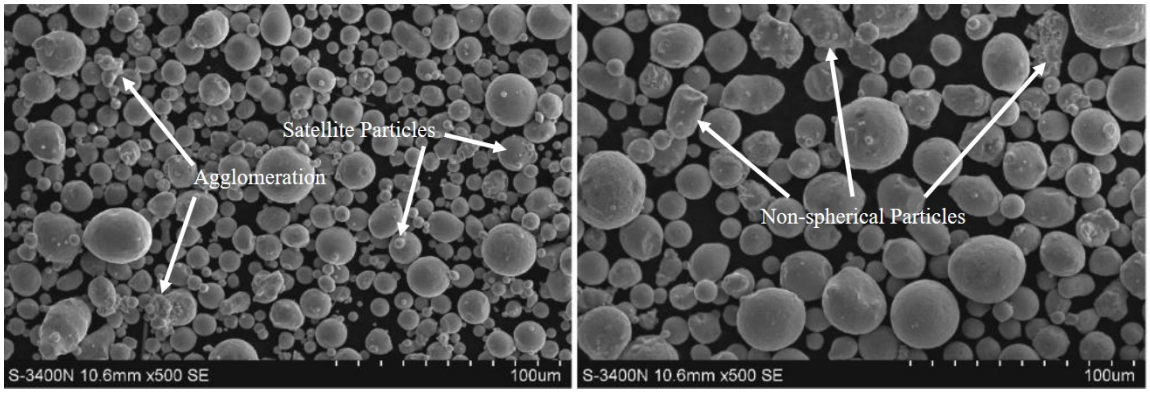


Figure 2.8: Gas atomized SS316L powder showing some common powder defects. (Images used from Chen et al. [33])

Focusing on how these powders are made can be important to their quality, and

also the quality of the SLM build. Most SLM powders are manufactured by gas atomization. Two typical gasses that are used in this process are argon and nitrogen, but depending on the material, this choice in gas can be critical. It has been seen in research that the gas used in the atomization process can affect the chemistry and phases of the resulting powder. Murr et al. have found that the difference in the atomizing gas on 17-4 PH stainless steel can change the phases seen in the powder. For Ar-atomized powder, the phase was completely bcc ($\alpha$-Fe), while the $N_2$-atomized powder was primarily in the form of fcc ($\gamma$-Fe) with roughly 6% bcc ($\alpha$-Fe) [34]. This is said to be caused by the fact that $N_2$ has 40% greater thermal conductivity than Ar, which will affect cooling rates. They continued on to show that this difference in powder phases can translate to the final build under certain conditions. For a different material system, Sudbrack et al. showed that nitrogen atomized Inconel 718 powder resulted in the final build experiencing grain boundary pinning from TiN particles that came from the atomization process [35]. Therefore, depending on the material system in question, the gas in which the powder is atomized could be very important.

Many of the powder characteristics listed above, such as powder size, shape, and distribution will affect the powder's flowability. Flow properties of the powder are important to ensure an even and uniform layer across the build platform and subsequent layers. Yablokova et al. have shown that poor flowability characteristics lead to inhomogeneous distributions of powder, leading to lower dimensional accuracy [36]. These poor flow properties can be attributed to many different aspects of the powder, such as powder size and shape. Baitimerov et al. state that in general, finer powder particles have a tendency to form agglomerates and reduce flowability. They also state that in their study they observe the best flowability from the powder that is most spherical in shape [37].

In addition to the powder's flowability, the apparent density, or how well the powder packs, is also very important. This is mainly influenced by the powder particle distribution. Having only larger particles leads to poor packing or poor apparent density, which results in more porosity in the final build. Chen et al. show in their study that increasing particle size increases the amount of porosity in the sample built [33]. For this reason, powder used in the SLM process has a particle size distribution in order to increase the apparent density of the powder bed by using the smaller particles to fill in the gaps between the larger ones. Aside from size, apparent density is also affected by particle shape. Baitinmerov et al. shows that irregular shaped powder particles inhibits the packing of the powder and results in a lower apparent

density [37].

Porosity within the powder particles can also cause issues within SLM builds. This porosity occurs during the gas atomization process in which the powder is manufactured. Iebba et al. discovered two different types of porosity when examining powder cross-sections; gas filled pores and solidification shrinkage pores, which are shown in Figure 2.9 [38]. In this study it was found that spherical shaped porosity in the SLM build, indicative of a gas pore, was of similar size to the gas pores found in the powder. This indicates that the pores within the powder have a chance of influencing the final build.

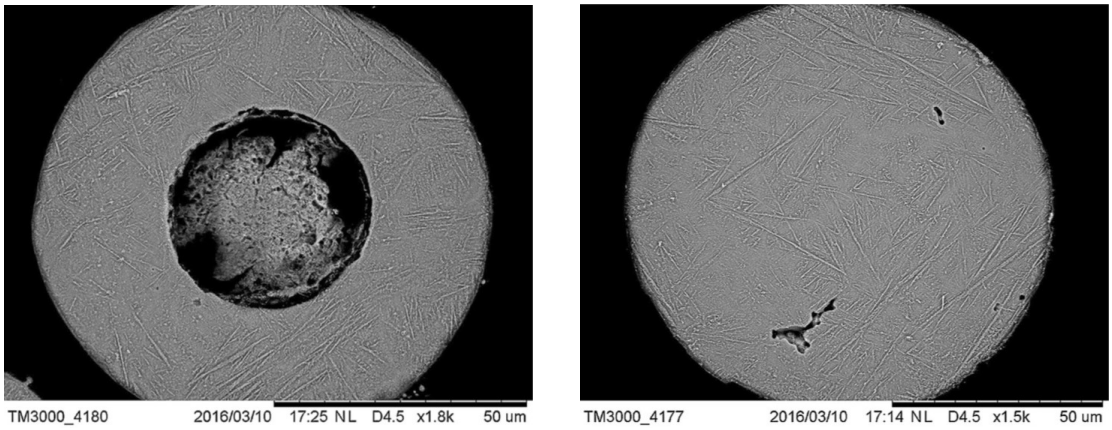


(a) Gas Filled Pore (b) Shrinkage Pore

Figure 2.9: Two types of porosity found within powder particles produced by gas atomization [38].

From the research that has been done on SLM powders, it can be seen that the quality of powder is extremely important in order to ensure a quality build. For eventual certification of the SLM process to happen, how the quality of the powder affects the build needs to be fully understood. Once this happens, the powder provided for SLM can have strict requirements in order to ensure desired part quality. Also, understanding how the powder affects the final build will help separate defects caused by powder from suboptimal process parameters.

**Build atmosphere** is another process input that has been shown to affect the outcome of an SLM build. The SLM process takes place in an inert gas environment; usually either argon or nitrogen. Not only is the build chamber filled with inert gas to bring the oxygen levels down to about 0.1-0.2% [39, 40] and avoid oxidation at high temperatures [41], but inert gas is also cycled just over the build plate in order to further protect the melt pool and powder bed from ejected particles. It has been shown in research that the type of inert gas and the flow to the inert gas can affect

different aspects of the final parts [34, 39, 40, 42, 43].

Murr et al. have shown that the gas in which the SLM process takes place can affect the outcome of the build. In this study both Ar-atomized and $N_2$-atomized 17-4 PH stainless steel powders were used in both Ar and $N_2$ filled build chambers. It was found that $N_2$-atomized powder within a $N_2$ filled build chamber resulted in an fcc-austenitic primary phase whereas all other combinations formed a bcc-martensitic phase [34]. This can be due to the fact that $N_2$ is not inert and can react with certain elements. On the contrary, Wang et al. have shown that for an Al-12Si alloy manufactured in argon, nitrogen, and helium, no significant differences in density or hardness were observed [42]. This shows that depending on the material system, the type of gas environment can factor into the final build.

Other than the type of gas used in the build chamber, the flow of this gas has also been shown to be extremely important. Dadbakhsh et al. discovered that temperature distributions and cooling rates can be affected by the part layout and gas flow, leading to deformations in the final build [43]. Ferrar et al. have shown that the flow of gas over the build plate can be non-uniform, affecting the density and compression strength of the samples [39]. Figure 2.10 shows their results relating gas flow uniformity to part density variation across the build plate. They observed that the more uniform the flow is, the more uniform the part density is. Also, Anwar et al. found that the direction of laser scanning with respect to the gas flow direction can have an impact on the quality of the build. They discovered that scanning in the same direction of the gas flow caused ejected particles to be carried into the beam path resulting in heat loss leading to incomplete melting and a lower ultimate tensile strength [40].

From this research, it is clear that the type of gas and the gas flow has a large impact on the overall quality of the build. The type of gas can be chosen so that no problems are caused and the gas flow can be improved by altering the delivery system. However, a deeper understanding of how both of these factors impact all material systems is needed for the future use of SLM.

**Build Location** is yet another process input that has the potential to cause intra-build variation. As previously discussed, Ferrar et al. have shown that the amount of porosity in a part can change based on its build location and the uniformity of the gas flow that passes over it [39]. Fitzgerald et al. have come to some similar conclusions by discovering small differences in tensile properties of SLM 316L stainless steel. They found that the largest variation was in the x-direction of the build plate, which happened to be the same direction of the gas flow in the machine used. They also

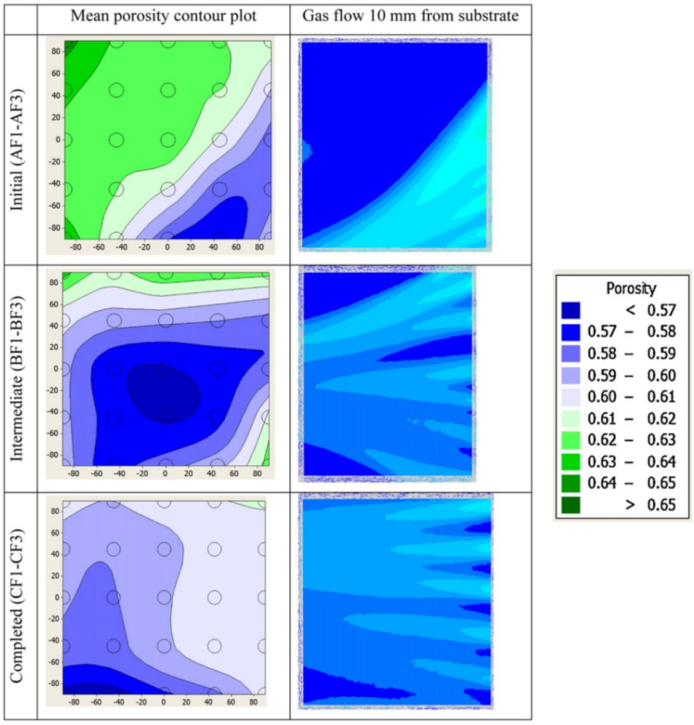


Figure 2.10: The effect of gas flow uniformity on the porosity measured throughout the build plate. The gas flow (right column) becomes more uniform from top to bottom causing the resulting build's porosity levels (left column) also becomes more uniform. [39]

investigated several other build quality factors, such as chemistry and grain size, all of which showed no change or insignificant trends [44]. Wang also investigated the variation in tensile properties due to build location using Hastelloy X alloy. He finds that the yield stress, ultimate tensile stress, and elongation are almost identical for samples that were built in the corners of the build plate and in the center of the build plate [45].

Build location variation has also been investigated in this research, however it will not be evaluated in depth in this thesis. The amount of porosity was evaluated using both optical microscopy and x-ray computed tomography for samples that ranged from the center of the build plate to the edge of the build plate. The preliminary results are shown below in Figures 2.11 and 2.12. From these figures it can be seen that porosity varies from part to part, but it not possible to develop a trend without more data.

This is just a brief summary of some of the inputs that go into the SLM process. There are many more that were not talked about, all of which play a role in the overall quality of a build. This overall quality of SLM builds that has been referred

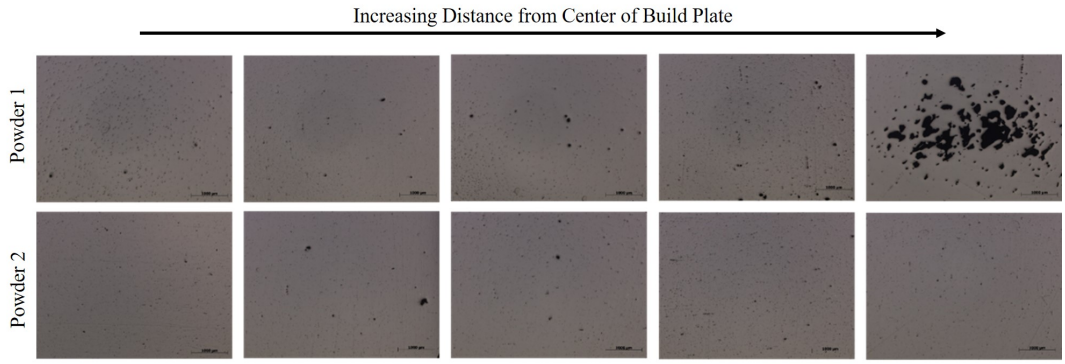


Figure 2.11: Preliminary results showing the variation in the amount of porosity as a part is built further from the center of the build plate. The rows of optical micrographs differ in the powder that they were made from. Each column represents a sample location, where the left most is closest to the center of the build plate and the right most is the closest to edge of the build plate.

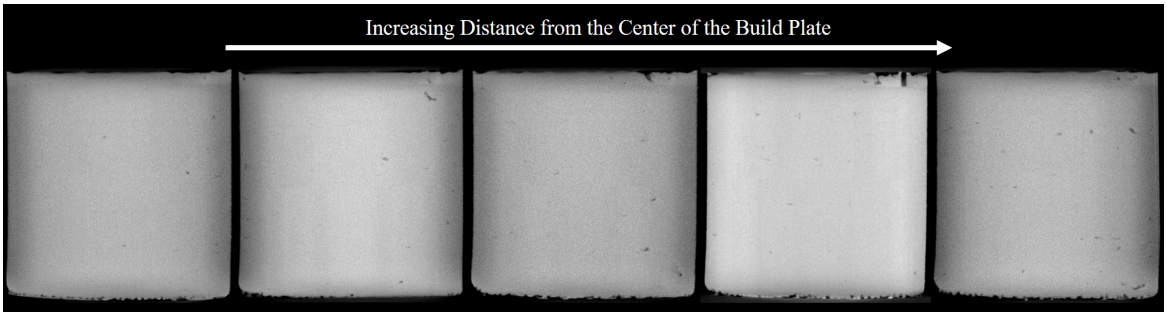


Figure 2.12: Preliminary results showing the variation in the amount of porosity as a part is built further from the center of the build plate using x-ray computed tomography

to in this section is referring to the many defects that can arise throughout the build process. In order to understand where these defects come from it is important to first understand the process inputs that cause them.

### Common Defects

Like any manufacturing process, SLM has its fair share of problems when it comes to process defects. Since the SLM process has so many input variables, the defects that arise in the final part are inevitable. This is why the control and optimization of the process inputs are so important to fully understand. The main defects found in SLM parts are porosity, cracking, and residual stress. There has been an immense amount of research focused on these defects that arise during the SLM process.

Arguably the most common defect in SLM is porosity. Porosity can come in two

different forms; either gas-filled porosity or lack-of-fusion (LOF) porosity. Gas-filled porosity, characterized by spherical pores, can form in a multitude of different ways. The first way is caused by the packing density of the powder bed. With poor packing density the gas present between powder particles is dissolved in the melt pool and is entrapped in the part because of SLM's high solidification rates [46]. Another mechanism leading to gas-filled porosity arises from the presence of gas-filled pores within the powder. This was talked about above where Iebba et al. have shown that this porosity in the powder can lead to porosity in the final part [38]. Gong et al. have also shown that gas-filled pores can be generated when high laser energy is applied, leading to the vaporization of low melting point constituents [23]. Lastly, gas-filled pores have been shown to come about due to melt pool instability. This is commonly referred to as keyhole porosity. This type of porosity has been found to occur at high laser energy densities, usually caused by poor process parameters and/or scan strategies, where the melt pool enters the keyhole regime, at which point it becomes unstable and collapses entrapping build atmosphere gas within the melt [47, 48]. This mechanism is shown in Figure 2.13 below. After this porosity is formed, it has the chance to make its way to the surface and escape, but because of the high solidification rates of SLM, not all of this entrapped gas is able to do so. The ability for this porosity to escape is material dependent. Huang et al. state that aluminum alloys have higher solidification rates and longer escaping distances, making it less likely for the porosity to escape [48].

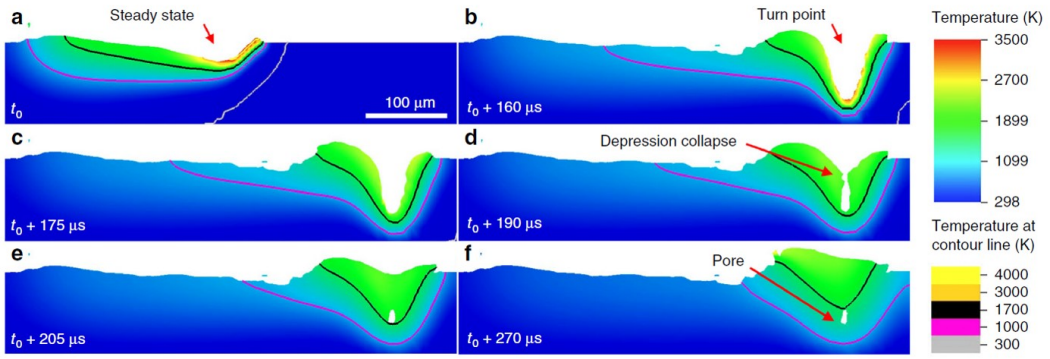


Figure 2.13: Step by step depiction of the formation of keyhole porosity. [47]

LOF porosity, characterized by irregularly shaped voids, are a common defect that arise when the laser energy density is too low. Li et al. state that at high linear laser energy densities the molten track is continuous due to the improved wettability [49]. Also, in a previous publication, Li et al. state that at lower laser energy density

the SLM process tends to exhibit a worsened wettabililty, leading to agglomerates or balls between which porosity is formed [50]. Recalling Equation 2.2.1, laser energy density is a function of laser power, scan speed, hatch spacing, and layer thickness. Any of these parameters can have an effect on the degree of balling and porosity in an SLM part. Yang et al. found that irregularly shaped defects are aligned either perpendicular or parallel to the building direction due to lack of fusion. They state that insufficient energy density leading to poor inter-layer fusion causes horizontally aligned defects, and insufficient overlap of the melt tracks cause vertically aligned defects [51].

Other common defects that arise from the SLM process are due to residual stresses. These defects include cracking and distortion. The main mechanism in which residual stresses come about is from the solidification and shrinking of the newly deposited layer due to thermal contraction, while the previously deposited layers inhibit this contraction [52]. These opposing forces instill stresses within the part. Any material with residual stresses will need to be relieved of them, and this occurs in two main ways; cracking and distortion. Part deformation due to residual stresses is shown by Liu et al. It can be seen in Figure 2.14 that parts with high residual stress will delaminate from the build surface and warp or deform. Liu et al. state that compressive stress occurs at the interface between subsequent layers and is enhanced due to subsequent thermal cycling, leading to the curling of the part [53]. Other than overall part deformation, residual stresses can be relieved through internal cracking. Li et al. state that the rapid SLM process induces large thermal gradients and a resultant high stress field, leading to cracks within the part in order to relieve this stress [50]. Zhao et al. state that these cracks will decrease tensile properties, however hot isostatic pressing (HIP) can greatly improve the properties by closing the cracks [54].

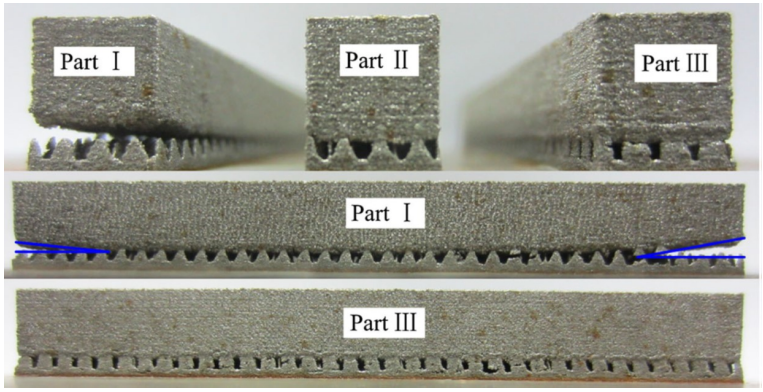


Figure 2.14: Part distortion seen in SLM parts due to high residual stresses. [53]

Another aspect of SLM parts that may be considered a defect is surface finish. While SLM surface finishes are not as bad as other AM techniques and can be easily machined away or polished, the surface finish of hard to reach areas such as internal features can be deleterious to part strength. Not only is the surface finish of internal features a possible issue, but the accuracy and their ability to be successfully built are a few others. Gunther et al. have shown that samples with internal channels have slightly lower fatigue limits as compared to their solid counterparts. They found that the fatigue failure is mainly due to the rough surface of the internal channel [55].

As for the accuracy of these internal features, Jansson et al. state that the ability to place features where they were designed to be is good, however the ability to manufacture small spheres was limited. They found that SLM was able to create internal spheres as small as 0.25 mm and state that when decreasing the size of features the accuracy rapidly decreases [56]. Kempen get into the accuracy of these internal features a bit more, stating that vertically produced features have to compensate for the width of the melt pool since the contours of the CAD data represent the center of the melt pool [57]. The width of the melt pool is determined by process parameters and the material itself, making the accuracy of this compensation difficult. They also state that for the top of horizontally produced features there needs to be compensation for dross formation. Dross formation occurs when scanning on top of loose powder material and the melt pool penetrates deeper than it would when normally scanned over a single layer of powder. This is even more difficult to compensate for because it depends on the packing of the powder and the varying heat conductivity [57].

The accuracy of the SLM process and specifically the accuracy of internal features was a part of this research, however it will not be covered in depth in this thesis. Samples were printed with both spherical and cylindrical internal features and were evaluated for accuracy. Figures 2.15 and 2.16 show some of the preliminary data. The spheres that were designed ranged from 100 to 800 microns. The 100 and 200 micron spheres were not successfully manufactured and the 300 to 800 micron spheres are seen in Figure 2.15. In the figure the maximum dimension is measured for each sphere. It can be seen that the 300 and 400 micron spheres are undersized, while the 500 to 800 micron sphere are relatively accurate. It is important to note that the 600, 700 and 800 micron spheres are filled in by what my be dross formation as talked about by Kempen [57]. The cylinders are presented in the same way in Figure 2.16. They are slightly over sized, but are relatively close to the designed dimension. It can also be seen that in both the spheres and cylinders that they all exhibit some

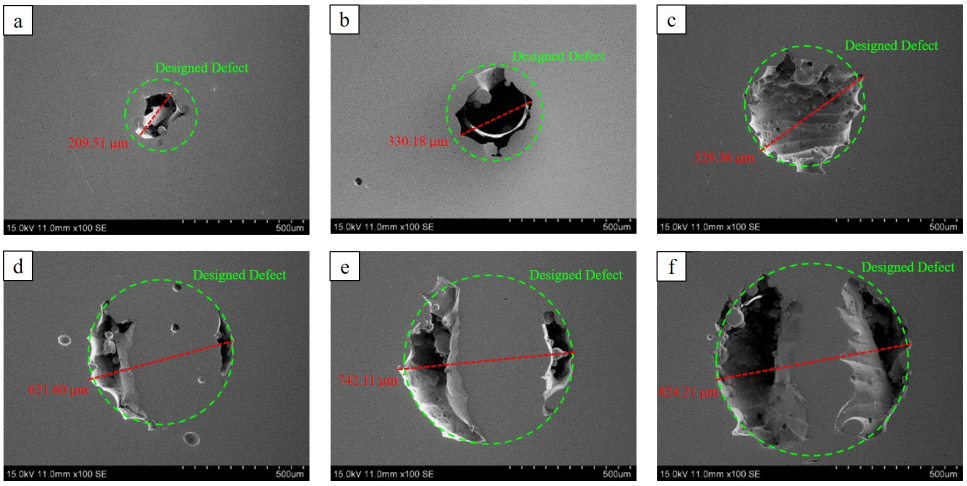


Figure 2.15: Spherical internal features and their actual size compared to their design. These spheres had the following designed diameter (a) 300 micron; (b) 400 micron; (c) 500 micron; (d) 600 micron; (e) 700 micron; (f) 800 micron.

level of surface roughness either due to scan tracks or unmelted powder.

From this highlighted research it can be seen that defects are common in SLM and they are of very high priority to alleviate. In order for SLM to make its push into industry, this process needs to be able to reliably produce defect free parts. These defects that arise in the SLM process are continuously being discovered and researched in the effort to fully understand where they come from and how to prevent them.

## 2.3 Selective Laser Melting of Inconel 718

SLM has a wide variety of benefits, many of which are accentuated when applied to Inconel 718. Inconel 718 is known as a difficult to machine alloy due to its high hardness and low thermal conductivity [58]. This, plus the fact that Inconel 718 would be used to produce complex and precise aerospace parts, it would be extremely difficult to manufacture with conventional methods. Not only will SLM make the manufacturing of current complex IN718 parts much easier, it will allow for the design of more complex components in order to reduce the total number of parts. This in turn reduces lead time, cost, and weight. This has already been proven by GE with the LEAP fuel nozzle made from CoCr [15].

In order to reap these benefits, there needs to be a complete understanding of the influence that the SLM process has on IN718. In an effort to achieve this under-

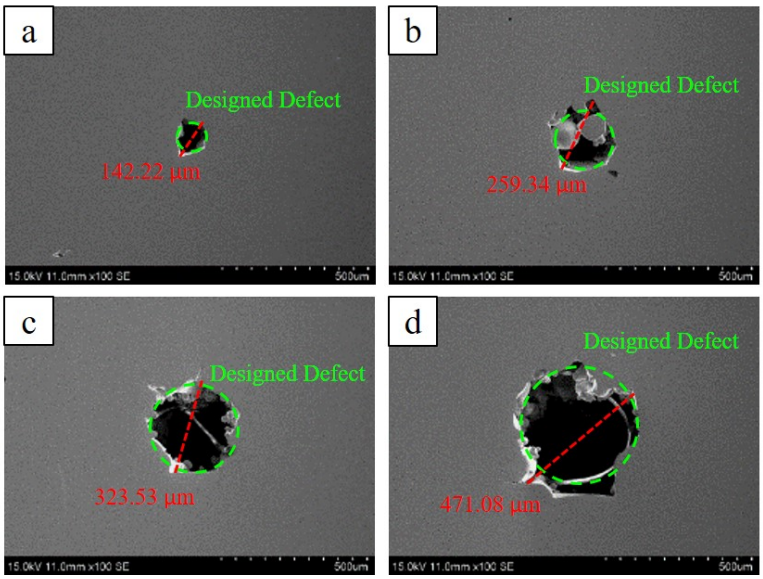


Figure 2.16: Cylindrical internal features and their actual size compared to their design. These cylinders had the following designed diameter (a) 100 micron; (b) 200 micron; (c) 300 micron; (d) 400 micron.

standing there has been an immense amount of interest focused on IN718 in SLM. Everything from process parameter development, to post process heat treatments have been explored as of late in order to produce the best SLM part possible.

### 2.3.1 Typical Microstructures

It is first important to understand what type of microstructure is obtained when producing IN718 parts in the SLM process. SLM Inconel 718 exhibits a columnar dendritic microstructure oriented parallel to the build direction in the as-built state [59]. These columnar grains tend to extend through multiple layers and contain a cellular structure and very fine dendrites. This is common of most materials produced through SLM. In terms of different phases, Sarley et al. report that the thermal cycling of the SLM process precipitates the deleterious δ-phase, as well as the primary strenthening phases of $\gamma$' and $\gamma$" [60]. Raza et al. add to this and state that other precipitates form in the interdendritic regions, such as MC-carbides and the laves phase [61]. These phases were covered in detail in Section 2.1.

While the types of precipitates are almost always found in as-built samples, the amounts of each of them can vary due to different input parameters. Tucho et al. observed about a 13% decrease in hardness between the bottom and top of the sample. They claim this is due to the precipitation of small $\gamma$' and $\gamma$" precipitates in the

bottom portion caused by the repetitive heating process in SLM [62]. This repetitive heating serves as an age-hardening process. On the contrary, Sarley et al. state that a greater amount of $\delta$ phase is found further up the build direction caused by that region being at a higher temperature for a longer time. They also show that the amount of $\gamma$' and $\gamma$" remain relatively unchanged up the build height [60]. This difference can simply be due to a difference in part geometry. Tucho et al. state that their shorter sample showed no difference in the amount of $\gamma$' and $\gamma$" as well, attributing it to a small height gradient [62]. The material's microstructure also can be affected by the scanning parameters. Moussaoui et al. state that at higher volumetric energy densities, the dendrites become longer and tighter, as well as more oriented along the build axis [59].

The texture of SLM IN718 is discussed by Nadammal et. al [63]. They find that the build direction-scan direction (BD-SD) plane is dominated by a rotated cube texture. In the scan direction-hatch direction (SD-HD) plane they observed a strong Goss texture ($\{110\} < 001 >$) with small contributions from the cube component. However this study points out that the strength of this texture is dependent on the scan strategy.

With all of these microstructural inconsistencies due to the manufacturing of IN718 through SLM, it is important to understand how post-process heat treatments can change the microstructure into something certifiable and consistent. There has been plenty of research in the area of the post-process treatment of SLM IN718, with the goal to find a heat treatment that will change the material to be comparable with conventional manufacturing processes. Popovich et al. explored the effects of heat treatment and hot isostatic pressing (HIP) on the microstructure and properties of SLM IN718. They found that recrystallization was not achieved during the heat treatment process, resulting in a preserved grain morphology and texture [64]. However, they observe decreased elongation due to a large amount of needle-like $\delta$ precipitates and undissolved Laves phases, as well as increased yield strength due to grain boundary precipitates. Similar to the results observed in the heat treatment, they find that HIPing retains both the grain structure and the preferred $\{100\}$ texture as well, but this process achieves dissolution of both the Laves and $\delta$ phases, improving mechanical properties. Lastly, they combined the two by heat treating after the HIP process. They noted a increase in the size and density of the carbides as well as a retained microstructure. Sarley et al. state that after their heat treatments XRD shows a decrease in $\delta$ phase as well as growth of $\gamma$" [60], which both benefit overall mechanical properties. Overall, different heat treatments have different effects

on the microstructure of SLM IN718, and finding the right one to reduce δ phase and Laves phase, while increasing or maintaining strengthening phases is crucial to the implementation of SLM IN718 parts in today's industry.

### 2.3.2 Mechanical Properties

As stated in the previous section, SLM IN718 parts can have a wide variety of microstructures and phases depending on the many process inputs. This in turn leads to a variety of properties from part to part and from build to build. Wang et al. nicely summarize some of the research that has already been done on the mechanical properties of SLM IN718. They have concluded that tensile strength of as-deposited material is comparable or superior to that of cast material, but inferior to wrought [58], where the range of yield strengths was from 723 MPa [65] to 903 MPa [66]. This wide range goes to show that differences in process parameters can have a large effect on the as deposited microstructure and defects. On the contrary, Wang et al. report that ultimate tensile strength and Young's Modulus are fairly consistent between the different studies, with ranges of 1117 MPa [65] to 1142.5 MPa [66] and 200 GPa [67] to 208 GPa [65], respectively. In addition, it is also shown that microhardness tends to vary from study to study as well, ranging anywhere from 3.07 GPa [65] to 3.90 GPa [68].

Since some of these properties are inferior to wrought or inconsistent, post-process heat treatments are necessary as talked about in the previous section. Wang et al. again summarize several studies and the effects of their different heat treatments. It is shown in all studies that the different heat treatments increase the yield and ultimate tensile strengths, as well as the microhardness to be comparable or superior to wrought properties.

## 2.4 Inter-Layer Time Interval in AM

The inter-layer time interval can be defined as the time it takes for the energy source to return to identical positions in subsequent layers. This is also best described as a single part's "beam off" time between layers. During this time the part is given the opportunity to dissipate heat before the energy source is scanned over it again. The main ways that this time interval can be controlled is either by a difference in the number of parts on the build plate and/or the geometry of these parts. Figure 2.17 depicts these two situations. Both of these scenarios are based on the idea that the

more scan area per layer, the longer the inter-layer time interval will be. The control of this time interval can be different for different AM processes. Some processes, such as LENS, allows for this time interval to be set, regardless of the scan area. This would add an additional pause at the end of a layer in order to let the heat dissipate even more. SLM on the other hand does not have this feature. There have been various research studies exploring the effects of this inter-layer time interval in direct energy deposition (DED) processes, however there have not been many focusing on SLM.

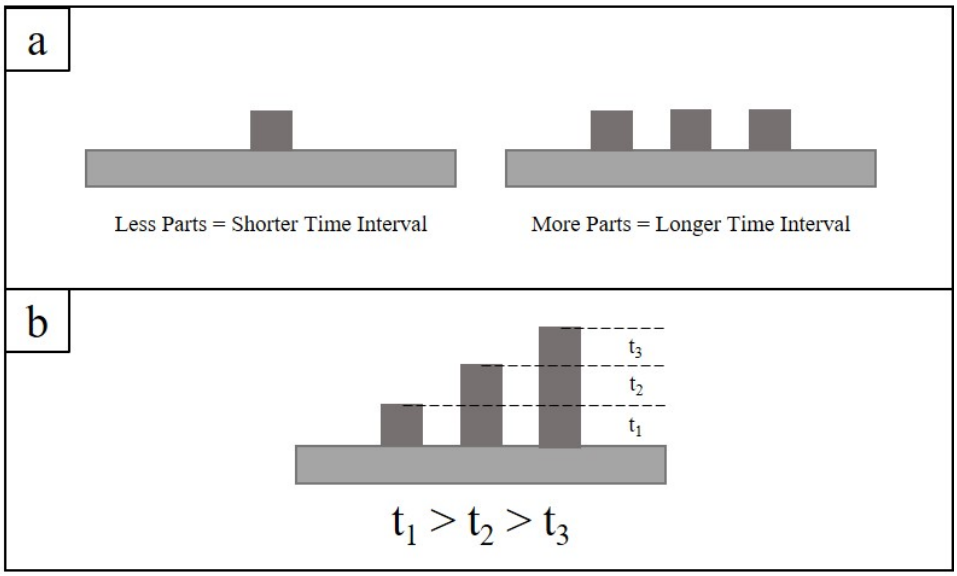


Figure 2.17: Depiction of two ways that the inter-layer time interval can be changed; (a) The number of parts, and (b) the heights/geometries of parts

### 2.4.1 Inter-Layer Time Interval in DED

DED is a form of additive manufacturing where material, in the form of either powder or wire, is fed into the energy source in order to build up material in a layer-wise fashion. This material fed process, as opposed to a powder bed process, typically results in higher deposition rates, higher energy input, and slower cooling rates. One common DED system is Laser Engineered Net Shaping (LENS). This system utilizes blown powder and a laser energy source to deposit material. It has been shown in research that this process is sensitive to the heat accumulation caused by the inter-layer time interval [69, 70, 71, 72, 73].

Costa et al. have developed a model to study the influence of substrate size and idle time on the microstructure and hardness of a ten layer AISI 420 steel wall built

by laser powder deposition. They had found that uniformity of the temperature distribution within the wall before the deposition of a new layer depends on the inter-layer time interval [69]. This has to do with the heat accumulation caused by the time given for the wall to cool. Lower inter-layer time intervals cause the average temperature of the material to increase as the wall is built up, leading to an increase of the melt pool size as build height increases [69]. Costa et al. also discover that with an inter-layer time interval greater than 10 seconds, the temperature of the layer will be such that austenite will tranform into martensite [69]. Therefor the inter-layer time interval will have an effect on the amounts of martensite and austenite in the final build. As a result, the hardness of the material will vary with the change in the volume fraction of martensite.

Yadollahi et al. explored the effects of inter-layer time interval using LENS for fabricating cylindrical specimens out of 316L stainless steel. The time interval was altered by either building one or nine cylindrical samples per build plate. They found that longer inter-layer time intervals increase cooling and solidification rates leading to finer microstructures. They also found that this led to higher yield and tensile strengths, as well as a reduction in elongation [70]. This increase in cooling rate is due to the fact that the part has time to cool, increasing the temperature gradient when the next layer is deposited. In addition, they state that the occurrence of imperfections, such as porosity, was more prevalent in specimens with longer inter-layer time intervals [70].

Torries et al. show the effect that the inter-layer time interval has on the fatigue behavior of Ti-6Al-4V produced by LENS. In this study they alter the time interval by building either one or two samples per build plate. They found that the samples built with a longer inter-layer time interval exhibited shorter fatigue life. They attribute this to the lower ductility and presence of large lack-of-fusion pores. They found that the samples built with a shorter time interval had smaller, more spherical pores that had less of an impact on the fatigue life [71].

It has also been shown by several researchers that the inter-time interval with-ing the LENS system has an effect on the distortion of the substrate and deposit [72, 73]. Bandari et al. conclude from their study looking at Ti-6Al-4V in LENS, that with longer inter-layer time intervals, larger distortions will be seen [72]. However, Denlinger el al. prove that this relationship can be material dependent. While Denlinger et al. concludes the same trend for Ti-6Al-4V, he also that the opposite trend happens in Inconel 625. They go on to measure residual stresses in each of the two materials, and find that residual stresses reach a minimum in Ti-6Al-4V when

there is no inter-layer time interval, while residual stresses decrease as the inter-layer time interval is increased [73].

From this highlighted research, it can be seen that the inter-layer time interval has a significant effect on the overall quality of DED builds. The control of this parameter is important to maintain a uniform temperature distribution. Since this parameter is so vital to DED processes, it poses the question, how does the inter-layer time interval effect other forms of AM?

### 2.4.2 Inter-Layer Time Interval in SLM

When compared to DED processes, SLM has much faster cooling rates and less heat accumulation through multiple layers. For this reason it is expected that the inter-layer time interval will have less of an effect on the SLM process. One difference from SLM to DED that makes the research of this effect that much more important is that unlike DED, the inter-layer time interval cannot be set to a specific value in SLM. This time interval in controlled through the number of parts and/or the geometry of the parts, therefor with a set build layout, the time interval cannot be changed. Since this is somewhat of an uncontrollable parameter, understanding its effects on the overall build quality is very improtant.

Mahmoudi et al. investigated the effect of the inter-layer time interval on the mechanical properties and microstructure of SLM 17-4 PH stainless steel. Their study altered the inter-layer time interval by changing the number of cylindrical samples that were built in a single build. One build had one cylindrical sample on it, resulting in an inter-layer time interval of 10 seconds, while the other build had 10 cylindrical samples on it, resulting in an inter-layer time interval of 50 seconds. They found that at the shorter inter-layer time interval the initial layer temperatures were higher, causing a reduction in the thermal gradient and cooling rate, leading to coarser grain sizes. They also show that shorter time intervals allow for higher austenite content due to the lower cooling rates. This higher austenite content results in the decrease of the material's microhardness. While this study highlighted some important differences in microstructure, they found that the tensile properties were not significantly affected by the inter-layer time interval [74].

The inter-layer time interval has not been as heavily researched in SLM as it has been in DED processes. As seen in DED, the time interval can have different effects on different material systems, therefore it is important to build on this research, and explore the effects on a variety of materials.

# Chapter 3

# Experimental Setup

This chapter will describe the setup of experiments that were used in this research. It will first start with the methods of sample preparation and characterization techniques in order to be able to investigate the starting material for the SLM builds. It will then go into the setup and design of the several SLM builds themselves.

## 3.1 Methods of Sample Preparation

Samples were prepared in a variety of different ways depending on the characterization technique. They were first sectioned using either a Buehler low speed saw or a wire electrical discharge machine (EDM) depending on whether they needed straight or 45° cuts, respectively. Depending on the characterization technique, some samples required mounting. These samples were hot mounted with Buehler black phenolic powder using a Buehler Pneumet I Mounting Press.

All samples were polished using a series of SiC paper grits (400, 600, 800, and 1200). This was either done by hand on a Pace Technologies NANO 1200T polisher, or automatically on an Allied METPREP 4 Grinder/Polisher with Power Head. For precise polishes, an Allied MultiPrep Micro-Polishing System was used. Depending on the needed finish, different combinations of final polish solutions were used. All samples were finished with Buehler MasterPrep 0.05 μm alumina suspension, but some samples needed intermediate steps with 3 μm and 1 μm diamond slurries.

For EBSD samples, a separate polishing procedure was used. Using the Allied MultiPrep Micro-Polishing System, samples were ground/polished in the following steps; 600 grit SiC paper at 125 rpm and a load of 300 grams until the sample was

flat, 1200 grit SiC paper at 125 rpm and a load of 300 grams for 7-8 minutes, 3 μm diamond slurry with a nylon polishing cloth at 75 rpm and a load of 200 grams for 8 minutes, and 1 μm diamond slurry with a nylon polishing cloth at 75 rpm and a load of 200 grams for 12 minutes. The final polishing step used Buehler MasterPrep 0.05 μm alumina suspension and a velvet polishing cloth on a Buehler Vibromet I polisher for several hours.

To look at melt pool and general grain structures, the polished surfaces were electrolytically etched in Lucas' reagent (50 mL lactic acid, 150 mL HCl, 3 g oxalic acid) for 10 seconds at 1.5 volts [75]. This etch was viewed under both polarized and non-polarized light, depending on the aspects of the microstructure being investigated.

## 3.2 Characterization Techniques

Given the variation in characterization needs, several microscopes were used in this research. A Leica MeF4 M inverted metallurgical microscope was used for bright field imaging and a Reichert-Jung MeF3 A inverted metallurgical microscope was used for polarized light imaging. For higher resolution micrographs, a FEI Helios plasma focused ion beam scanning electron microscope (PFIB-SEM) and a Hitachi S-3700N SEM were used.

EBSD was either carried out in a TESCAN VEGA3 SEM or a Hitachi S-3700N SEM that were both outfitted with EDAX EBSD systems. Grain size and texture analysis was carried out using OIM post processing software. The EBSD data was cleaned with post processing software, where the cleaned percentage ranged from 10 to 15 % depending on the scan.

X-ray computed tomography (XCT) scans were obtained on either a X-TEK HMXST225 or a Nikon Metrology C2 depending on machine availability. Both machines were equipped with an open chamber tungsten filament x-ray source and were able to obtain a resolution of approximately 10 to 11 μm for the samples of interest.

Melt pool average radius of curvature was measured using ImageJ and a series of optical micrographs. Each micrograph of interest was imported into ImageJ where between 10 and 14 circles were best fit to randomly selected melt pools. The circles were first made tangent to the bottom of the melt pool, then expanded until they fit the curvature. These circles were then measured, averaged, and divided by two, resulting in the average radius of curvature.

Microhardness was measured using a Stuers Duramin-100 automated microhardness tester. Measurements were obtained on the Vickers scale with a load of 200

grams and a dwell time of 10 seconds.

Tensile testing and modulus testing was carried out using a xx tensile test stand. A load rate of 0.010 in/min was used until sample failure. Data was collected at a frequency of 2 Hz. Elongation was measured using back to back one inch gage length extensometers.

Pore density [#/mm$^2$] was obtained through the analysis of XCT slices using ImageJ. First, an area of interest was marked out on each slice avoiding edges of the sample and focusing on the bulk of the material. The number of pores within this region is counted and recorded. The number of pores divided by the area of interest yields a pore density of a single slice. For a more accurate representation of a certain region multiple slices were taken and averaged.

## 3.3 Starting Material

Inconel 718 powder was obtained from Praxair Surface Technologies at a size distribution of 15 to 45 microns. The powder was manufactured by inert gas atomization, where the inert gas was Ar. Previous studies discussed in Section 2.2.2 have shown that powders can come with a variety of quality features, such as chemistry, size, shape, morphology, etc. These features can sometimes have a major effect on the overall quality of the final part. Therefore, in order to fully understand everything observed in the final build, the starting material needs to be characterized.

A small sample of the powder was sent out to analyze its chemistry using Direct Current Plasma Atomic Emission Spectroscopy (DCP-AES). Only the major alloying elements were analyzed for in this process. The results are shown in Table 3.1 along with the desired composition from ASTM F3055-14. It can be concluded that the powder for this study conforms to the standard.

Table 3.1: Inconel 718 powder compositions compared to ASTM standard.[A]

| **Element** | **ASTM F3055-14 [76]** | | **DCP-AES** |
|---|---|---|---|
| | **Minimum** | **Maximum** | **Analysis (Praxair)** |
| Carbon | - | 0.08 | |
| Manganese | - | 0.35 | |
| Silicon | - | 0.35 | |
| Phosphorous | - | 0.015 | |
| Sulfur | - | 0.015 | |
| Chromium | 17.00 | 21.00 | 18.50 |
| Cobalt | - | 1.00 | |
| Molybdenum | 2.80 | 3.30 | 2.97 |
| Niobium + Tantalum | 4.75 | 5.50 | 5.08 |
| Titanium | 0.65 | 1.15 | 0.92 |
| Aluminum | 0.20 | 0.80 | 0.52 |
| Iron | remainder | | 18.24 |
| Copper | - | 0.10 | |
| Nickel | 50.00 | 55.00 | 53.61 |
| Boron | - | 0.006 | |

[A] All values are in weight percent.

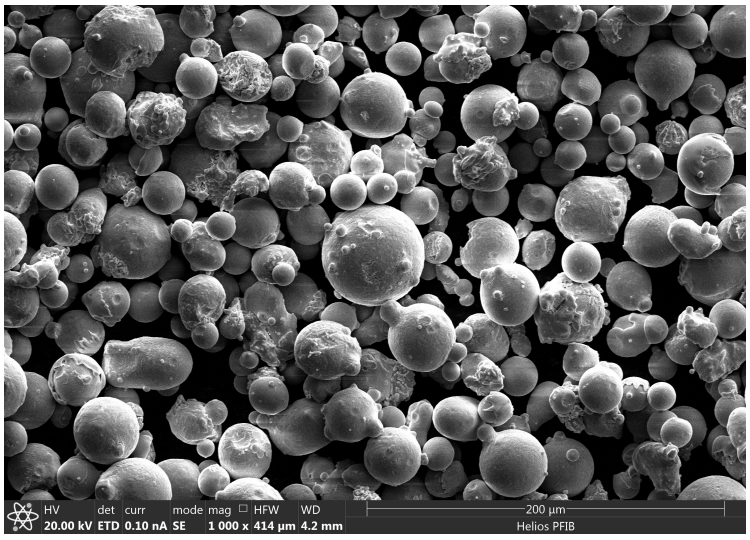


Figure 3.1: Praxair powder secondary electron micrograph imaged on FEI Helios PFIB.

The powders was mounted on carbon tape and looked at using a FEI Helios PFIB. Figure 3.1 shows a secondary electron micrograph obtained at 1000x magnification with the Everhart-Thornley detector (ETD). Looking at this micrograph it can be observed that the powder particles are relatively spherical and have a consistent surface morphology. The micrograph shows evidence of smaller satellite particles attached, as well as mixed regions of agglomeration. By visual inspection, the Praxair powder appears to have a wide particle size distribution. Measurements were taken from SEM micrographs using ImageJ resulting in particle size distributions of roughly 11-57 μm.

The powder was mounted in cold-mount epoxy and polished in order to image its cross-section. Figure 3.2 shows a backscatter electron micrograph of the cross-section at 2000x magnification on a Hitachi S-3700N SEM. It can be observed that there are very slight amounts of porosity within the powder particles shown by white arrows. It can also be observed that the Praxair powder has a fine dendrite structure.

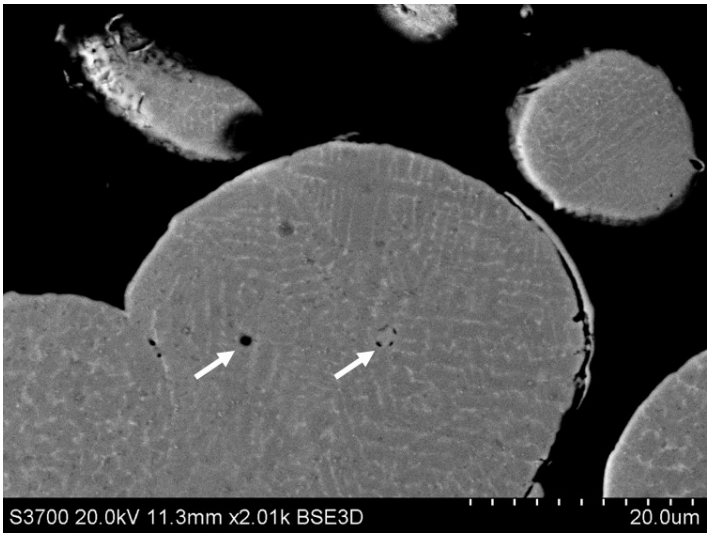


Figure 3.2: Praxair powder cross-section backscatter electron micrograph, where the white arrows denote porosity.

## 3.4 SLM Builds

The samples in this thesis were made in a SLM Solutions SLM280$^{HL}$. This machine is equipped with a 400 W fiber laser and has a build envelope of 280 mm by 280 mm by 350 mm. The laser spot size is approximately 80 μm. All builds were manufactured with a layer thickness of 30 μm, using the default process parameters and stripes scan

strategy that SLM Solutions provides. The stripes scan strategy is shown in Figure 3.3. It starts with a double contour scan which melts the border of the part, then fills that contour with 45° stripes that are approximately 7.5 mm wide. The stripes are made up of a hatch that has a spacing of 120 µm. The hatching parameters, which compose the bulk of the build, were as follows; laser power of 200 W and scan speed of 900 mm/s. From these parameters the laser energy density used in the bulk of the samples can be calculated using Equation 2.2.1. This results in a laser energy density of 62 J/mm$^3$.

From layer to layer this scan strategy does not rotate and the scan tracks do not move, therefore each scan track is programmed to be directly on top of the one from the previous layer. However, the stripes themselves move by approximately 650 µm every layer in order to keep the starts and stops from being stacked on top of each other throughout the entire build. For all builds, every sample was built on top of 4 mm of support material.

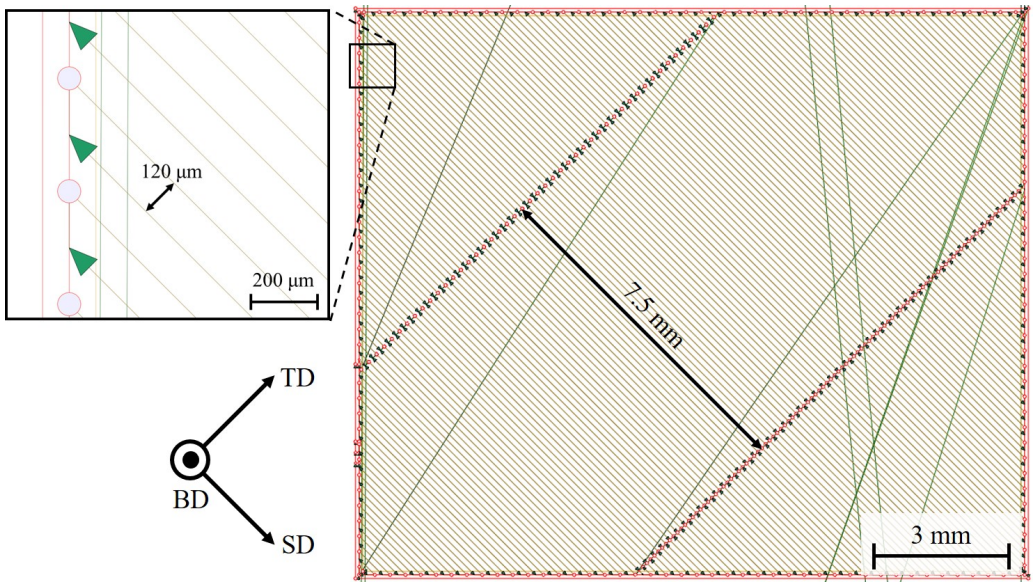


Figure 3.3: Stripes scan strategy used for all builds; All lines represent laser scan paths except the green are laser off traverses

### 3.4.1 Initial Build Design

The initial build was designed to induce and mimic some of the various defects that arise in the SLM process. This was done through three different sample geometries; a solid control cube, a seeded defect cube, and a triangular prism. All three of these geometries are shown in Figure 3.4.

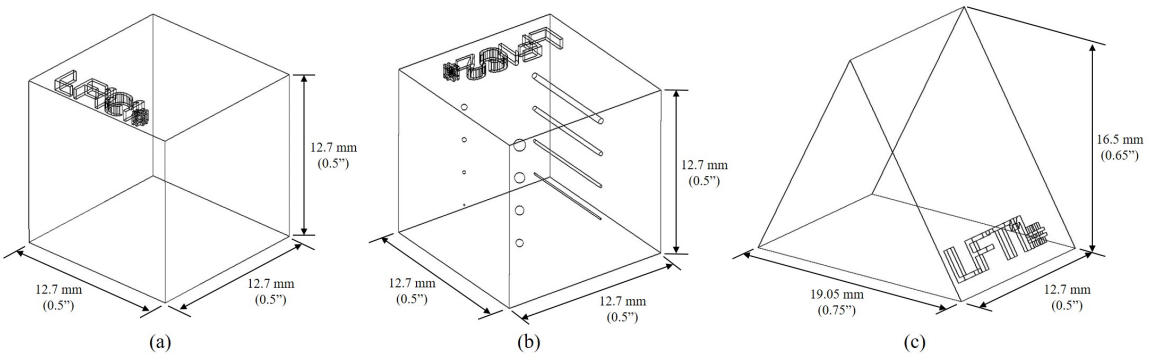


Figure 3.4: Initial build sample geometries. These samples are referred to as (a) control cube, (b) seeded defect cube, and (c) trinagular prism.

The control cube, shown in Figure 3.4a, is a solid 12.7 mm (0.5") cube intended to give a baseline of IN718 in this SLM machine. Undisturbed grains structures, melt pool behavior, and natural defect formation can be observed in this sample. The seeded defect cube, shown in Figure 3.4b, is a 12.7 mm (0.5") cube with various sized internal features. The cube consists of eight spheres and four cylinders intended to mimic point and line defects, respectively. The spherical defects range from 100 µm to 800 µm in diameter, and the cylindrical defects range from 100 µm to 400 µm in diameter. The drawing that includes full dimensions of this seeded defect cube is in Appendix A. These seeded defects will allow the investigation of the build process around an existing defect as well as allow the exploration of internal feature limitations. The triangle sample, shown in Figure 3.4c, is a triangular prism with a 19.05 mm by 12.7 mm (0.5" by 0.75") base and an overall height of approximately 16.5 mm (0.65"). These samples were designed taller than all other samples in order to intentionally force more heat build up in upper layers. By reducing the amount of area that the laser needs to scan in a single layer, the time between layers, or the inter-layer time interval, will be reduced, giving less time for the sample to dissipate heat. This inter-layer time interval and the specific times for this geometry will be covered in more detail in the next chapter.

The layout of these samples is shown in Figure 3.5. This layout was designed to test how the location of the sample affects its overall quality. In most SLM systems the laser source is located above the center of the build plate and is deflected to reach the outer portions of the build plate. In this layout, the location of the samples are varied radially from the center of the build plate, to test if the laser-powder interaction angle will have an effect on build quality. There are five control cubes and five seeded defect cubes that are positioned starting at 30.2 mm from the center of the build plate

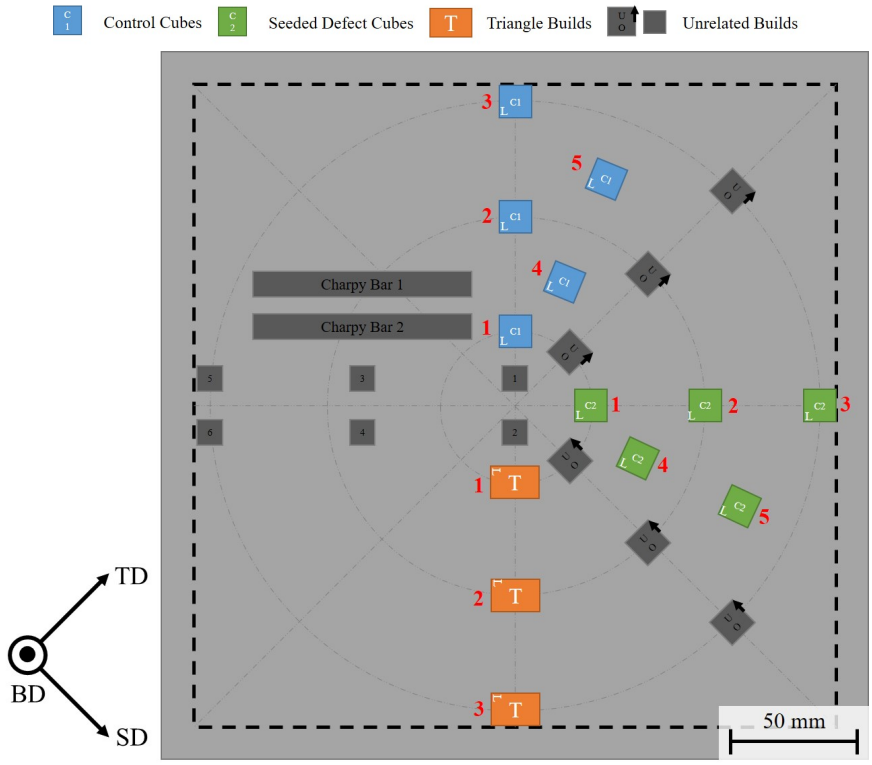


Figure 3.5: Initial build layout for sample generation; Sample orientation is denoted by the 'L' in the corner of each sample indicating where the label was located.

and increment by 22.3 mm towards the edge of the build plate. As for the triangle samples, there are three of them positioned starting at 30.2 mm from the center of the build plate and increment by 44.6 mm towards the edge of the build plate. All other samples seen in Figure 3.5 are unrelated to this research, however play a role in the influence of the inter-layer time interval. For this reason it is important to know that all samples marked unrelated in Figure 3.5 are 12.7 mm in height or less.

### 3.4.2 Second Build Design

A second build was designed with the intent of eliminating some variables from the initial build and focussing in on the inter-layer time interval. Geometries are simplified to solid samples with constant cross-sectional areas of 12.7 mm (0.5") by 12.7 mm (0.5") that varied in height. There are three step changes in height, where the shortest samples are 6.35 mm (0.25") tall, the middle samples are 12.7 mm (0.5") tall, and the tallest samples are 19.05 mm (0.75") tall. These sample geometries are shown in Figure 3.6. In addition to the aforementioned samples, subsized tensile samples are also included in this build. Their dimensions are shown in Figure 3.6d.

These dimensions comply with ASTM E8/8M-16 [77]. There are two different tensile samples in the fact that they are built to two different heights. Three of the six samples are built to a thickness or height of 6.35 mm (0.25"), while the other three are built to a height of 12.7 mm (0.5"). Post-process wire EDM extracted a 2.5 mm (0.1") thick tensile sample from each of the builds. This leaves the as-built surface on the sides while the top and bottom faces will have an EDM finish. These two different tensile samples are intended to test the difference between the inter-layer time intervals.

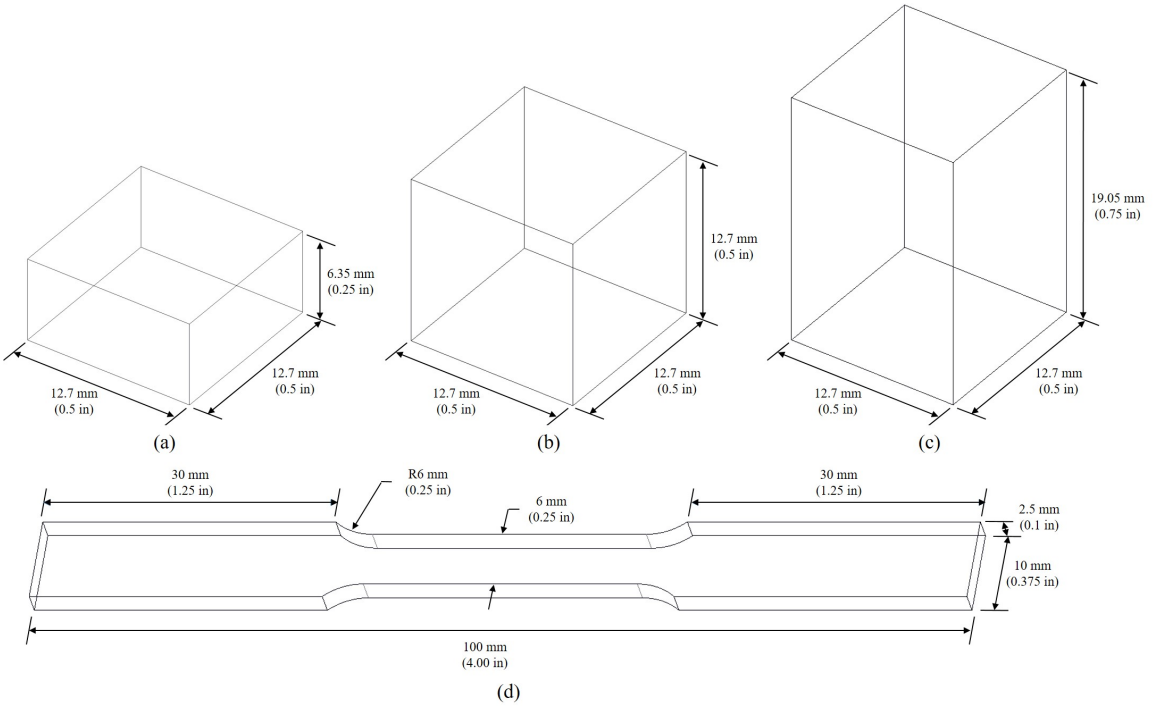


Figure 3.6: Second build sample geometries. These samples are referred to as (a) short rectangular prism, (b) cube, (c) tall rectangular prism, and (d) is a subsized tensile specimen as per ASTM E8/8M-16.

The layout of these samples is shown in Figure 3.7. Similar to the first layout, this was designed to look at how build location affects the build's overall quality. The difference here is that instead of a radial layout, this is a grid layout, where the samples are spaced out by 5.6 mm in both directions. This will give a more complete representation of the entire build plate and how the build quality changes throughout. It will allow for the investigation of gas flow effects as well as laser-powder interaction angle. In addition to the grid, the subsize tensile samples are inserted in the open spaces towards the outside of the build plate and the tall rectangular prism samples are positioned close to the center of the build plate.

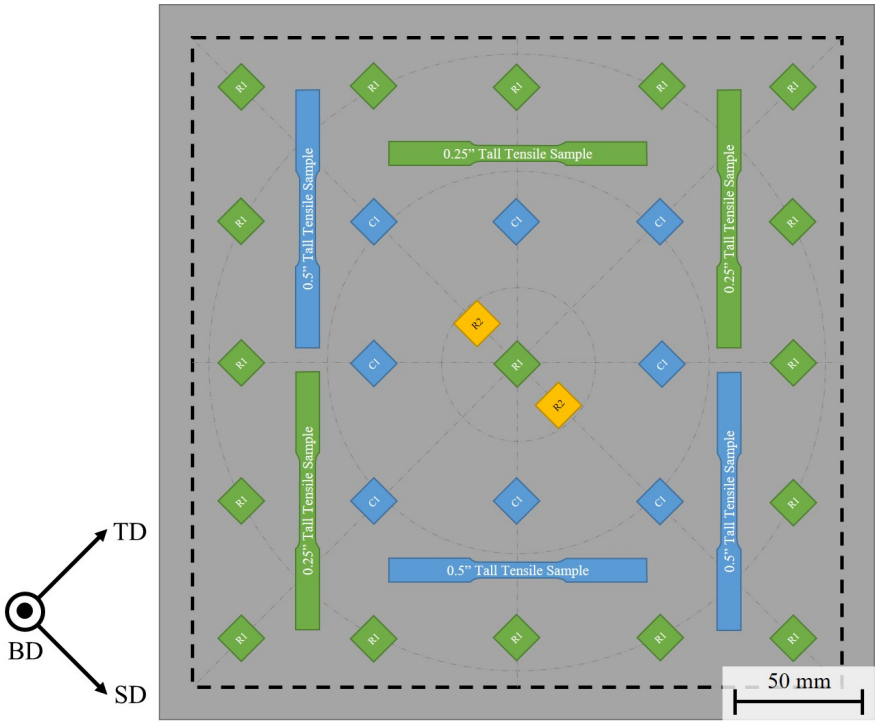


Figure 3.7: Second build layout for additional sample generation. Sample colors represent their heights; green samples are 6.35 mm (0.25") tall, blue samples are 12.7 mm (0.5") tall, and yellow samples are 19.05 mm (0.75") tall.

# Chapter 4

# Effects of the Inter-Layer Time Interval

Introduced in Section 2.4, the inter-layer time interval (ILTI) is a process parameter that describes the time it takes for the laser to return to identical locations on successive layers. As described earlier, the SLM process scans each layer part by part, giving the first part a certain amount of "beam off time" before the next layer of powder is spread and the laser scans again. This amount of time between build layers plays a role in the heat accumulation in the part, which can affect certain aspects of the build.

The ILTI is dependent on the number of parts on the build plate, the part geometry, and/or part orientation. This dependency comes from the amount of cross-sectional scan area per layer. More parts will increase the total cross-sectional scan area, thereby increasing the amount of time between build layers. The geometry of parts influences the ILTI by either varying build heights in a single build, or varying cross-sectional area of a single part. The former leads to a decrease in the time interval when a shorter part on the build plate completes, but a taller part continues, resulting in a reduction of total cross-sectional area. This will cause the taller part to be built with less time between build layers for the remainder of its height. The latter leads impacts the time interval to either increase or decrease depending on the changing cross-sectional area. Both of these scenarios will cause time interval differences within a single part, potentially leading to inter-part variability. Lastly, part orientation can also play a role in altering the ILTI. If a high aspect ratio part is built standing up versus laying down, the cross-sectional area to be scanned changes,

leading to a difference in the ILTI.

It is suspected that when this time significantly changes there could be detrimental effects to the microstructure, properties, and overall build quality, making this an important topic of research. This section will explore the effects of the ILTI on a part's overall build quality.

## 4.1 Results

### 4.1.1 Results from Initial Build Design

The samples of interest from this build are the triangular prism samples discussed in Section 3.4.1. These samples had a step change in the ILTI that occurred when all other samples on the build plate were completed. Figure 4.1 shows the triangular prism geometry with the time intervals as the build height increases. At the base of the triangle the ILTI is 69 seconds, just before the transition it is 39 seconds, and from the transition to the tip it is 13 seconds. In addition to the step changes, the ILTI for this sample is constantly changing because of its geometry. Since the cross-sectional area of the triangle gradually gets smaller as the build height increases, the ILTI will gradually decrease as well. However, once the ILTI reaches 13 seconds, as it does in the upper region, it will not go any lower regardless of how small the cross-sectional area gets due to the amount of time it takes the machine to spread a new powder layer. Each region was characterized using various techniques to evaluate the effect of the ILTI.

#### Microstructural Characterization

Initial investigations on these triangles revealed an abrupt change in both melt pool shape and melt pool stacking when the ILTI dropped to 13 seconds. This change can be seen in Figure 4.2.

The change in melt pool shape occurs 3.8 mm from the tip of the triangle, which is equal to 12.7 mm from the base. This is precisely where the ILTI changed from 39 seconds to 13 seconds. The melt pools in the upper region are observed to be deeper than the ones before the transition. It is also worth noting that the melt pools before the transition seem to be staggered, not stacked directly on top of each other. Recalling the scan strategy that was used in this build, discussed in Section 3.4, the scan tracks were programmed to be vertically aligned with respect to successive layers.

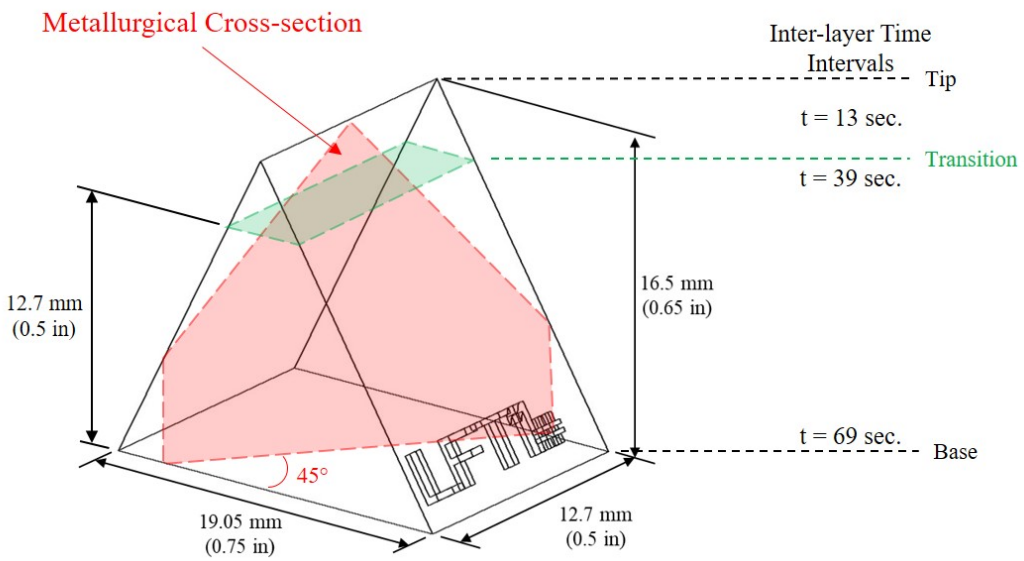


Figure 4.1: Triangular prism sample with inter-layer time intervals at different heights in the build. The red plane is where the samples were EDM cut and polished for metallurgical analysis. The green plane represents the build height at which all other samples on the build plate completed.

In order to quantify the difference in melt pool shape, the radii of curvature (ROC) at the bottom of the melt pools were measured as described in Section 3.2. Since a multi-layer build makes it difficult to obtain conventional measurements such as width and depth, the ROC was used as an alternative way to quantify shape. The idea is that with a smaller ROC, the melt pool is deeper and not as wide, while a larger ROC is shallower and wider. The results of these measurements are shown in Figure 4.3.

From Figure 4.3 it can be observed that there is a sudden drop in the melt pool radius of curvature near the build height at which the ILTI changes. The ILTI transition and the melt pool change do not match up perfectly most likely due to error in build height measurements made on the optical microscope. However, it can be noted that at lower ILTIs the melt pool radius of curvature is smaller, indicating the melt pools are deeper. The melt pool radius of curvature decreases in the bottom region from approximately 160 microns to 119 microns, then drops to approximately 70 microns and continues to fall to about 59 microns at the tip.

The microstructure was investigated further with EBSD in order to get information about the grain size and shape, as well as texture. Three separate regions positioned along the build height were scanned. They are labeled bottom, middle, and top, where the bottom and middle scans are before the ILTI transition, and the

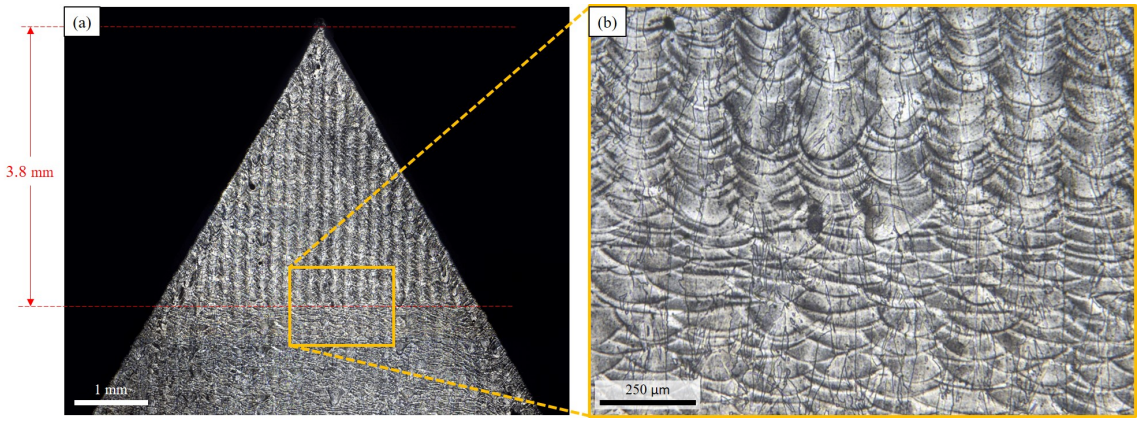


Figure 4.2: Melt pool shape and stacking differences observed in triangular prism samples due to the change in the inter-layer time interval. (a) Macroscopic image of upper region of triangular prism capturing the transition (b) 50x micrograph of the inter-layer time interval transition.

top scan is after. The scan direction inverse pole figure (SD-IPF) maps are shown in Figure 4.4.

It can be observed in Figure 4.4 that the general grain structure is composed of grains elongated in the build direction. Comparing the bottom and middle sections, there is minimal difference in terms of grain shape, however, in the top region grains become more elongated, creating very organized columns of grains separated by other very thin or fine grains. In comparing the two samples, the bottom and middle regions are very similar, while the top region of the LF1T13 sample has a larger population of fine grains than that of the LF1T11 sample. This is apparent when you look at the grain area averages presented in Table 4.1. For the LF1T11 sample, the average grain area increases with build height and has a larger increase in the top region due to the ILTI. For the LF1T13 sample, the average grain area remains relatively unchanged due to the large amounts of fine grains. The only difference between the two samples is the build location, refer back to Figure 3.5, potentially resulting in a different melt pool shape caused by the angle at which the laser is deflected. The different melt pool shape will result in different thermal gradients, potentially more susceptible to nucleation of new grains instead of epitaxial growth. Table 4.1 also gives information on grain size and shape. From the bottom to the top region of the LF1T11 sample the grains get slightly larger in both the horizontal and vertical directions, while LF1T13's grain shape stays relatively the same from bottom to top.

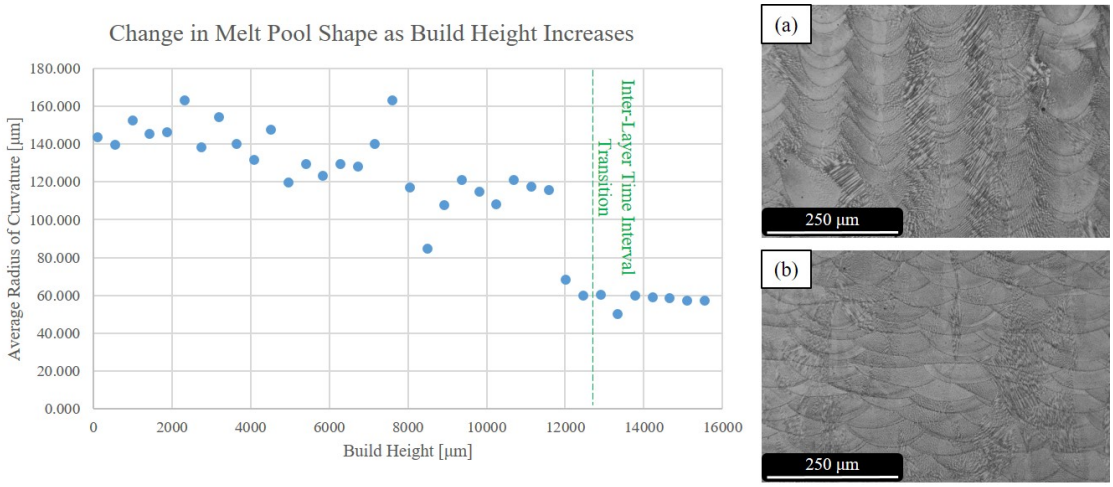


Figure 4.3: Melt pool radius of curvature as a function of build height for the triangular prism samples built from the initial build design. (a) Micrograph of melt pools above the transition, and (b) micrograph of melt pools below the transition.

Table 4.1: Average grain sizes for the triangular prism samples obtained from OIM post-processing software.

| **Grain Size Information** | **LF1T11** | | | **LF1T13** | | |
|---|---|---|---|---|---|---|
| | **Bottom** | **Middle** | **Top** | **Bottom** | **Middle** | **Top** |
| Horizontal Intercept Length [µm] | 21 | 23 | 29 | 19 | 20 | 22 |
| Vertical Intercept Length [µm] | 38 | 41 | 48 | 36 | 32 | 31 |
| Average Grain Area [µm$^2$] | 978 | 1179 | 1546 | 833 | 790 | 828 |

Pole figures were also obtained through the OIM post-processing software in order to provide information about the material's texture. The pole figures represent texture in the transverse direction-build direction (TD-BD) plane and are shown in Figure 4.5. The texture that developed in the SLM process is a 45 degree rotated cube texture, (001)[100] oriented in the scan direction. It can be seen by the maximum values of the pole figures that the texture strengthens when the ILTI decreases.

Electron dispersive spectroscopy (EDS) was performed on both triangular prism samples at each of the regions; bottom, middle, and top. Area scans were taken in

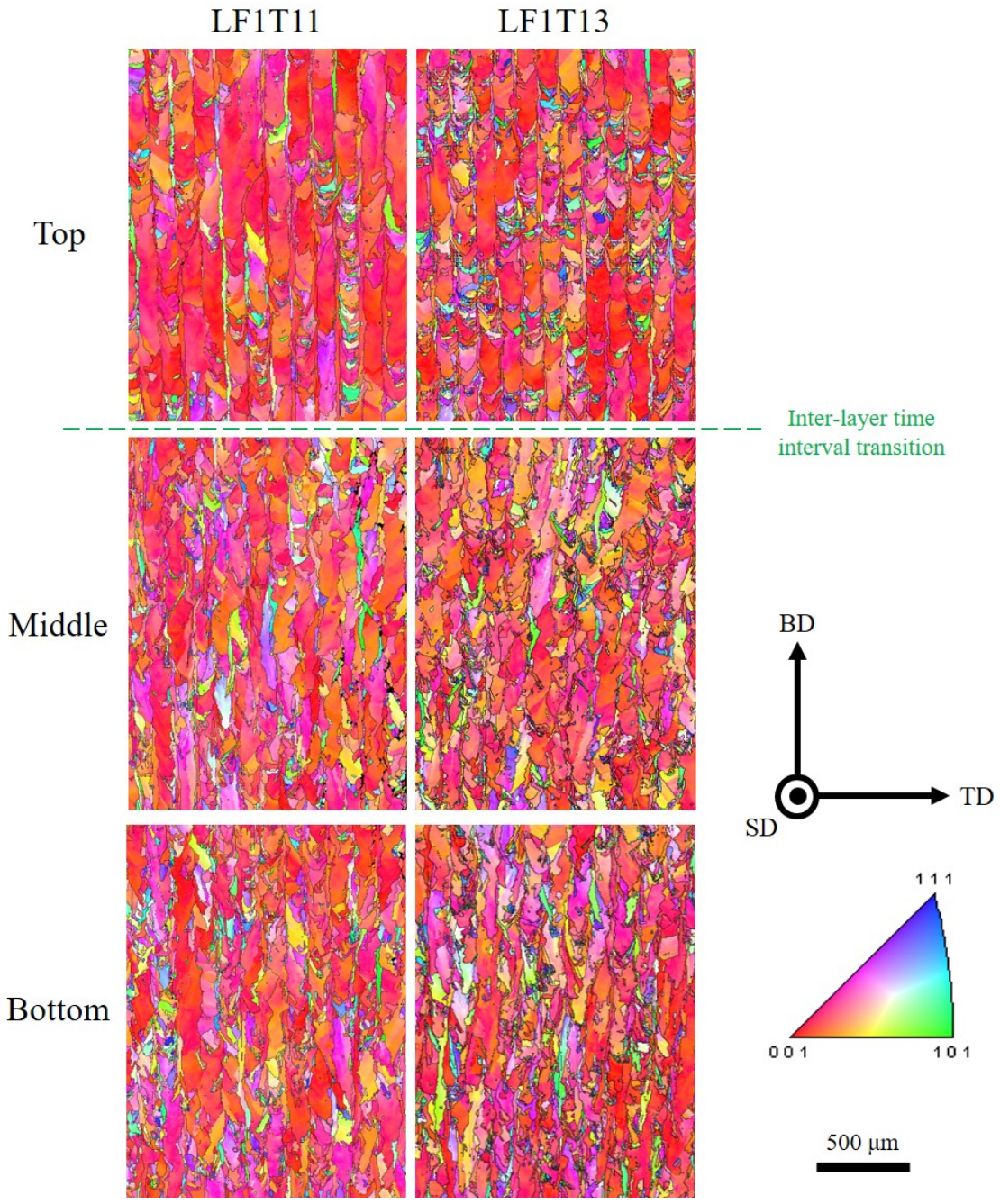


Figure 4.4: Build direction IPF maps for the bottom, middle, and top regions in two different triangular prism samples. LF1T11 is the sample built closest to the center of the build plate and LF1T13 is the sample build closest to the edge of the build plate.

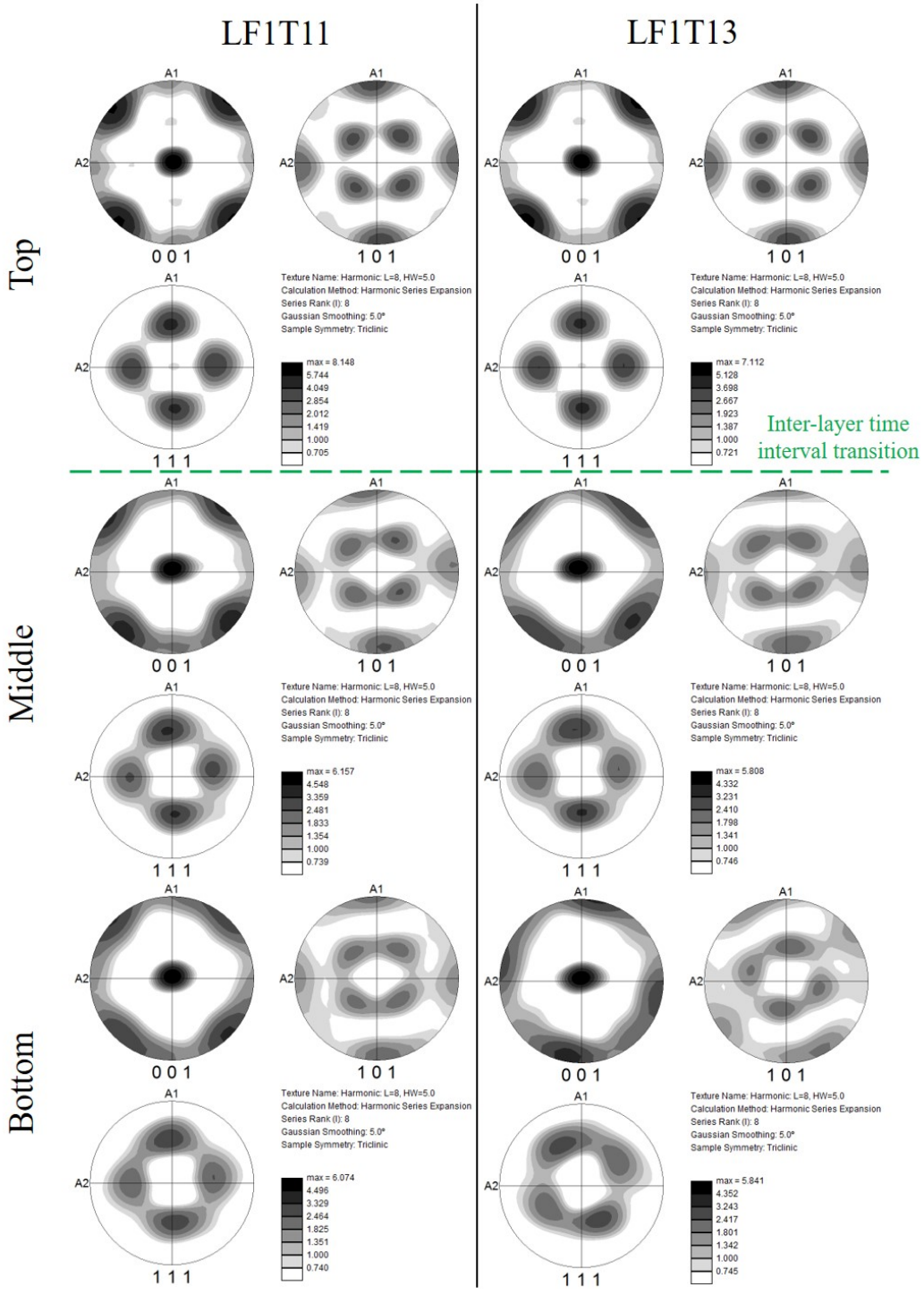


Figure 4.5: TD-BD pole figures obtained at eack of the three scan regions for each triangular prism sample. A1 and A2 axes are equivalent to the BD and TD, respctively.

order to see if the ILTI had any effect on the bulk composition of the material. All major alloying elements were found to be within the compositional ranges of IN718 for every region. At high magnification, micro-segregation was found at varying degrees throughout each sample. This is seen in Figure 4.6. The white regions are Nb, Mo, and Ti rich, as well as sparse inclusion of Ni, Cr, and Fe. These micro-segregation regions are seen in all regions and do not seem to be affected by the ILTI. Micro-segregation is seen throughout literature for SLM IN718 [78, 79]. Tao et al. state that the segregation of alloying elements in inter-dendritic regions could result in the precipitation of Laves phase, which is a deleterious precipitate to mechanical properties [78].

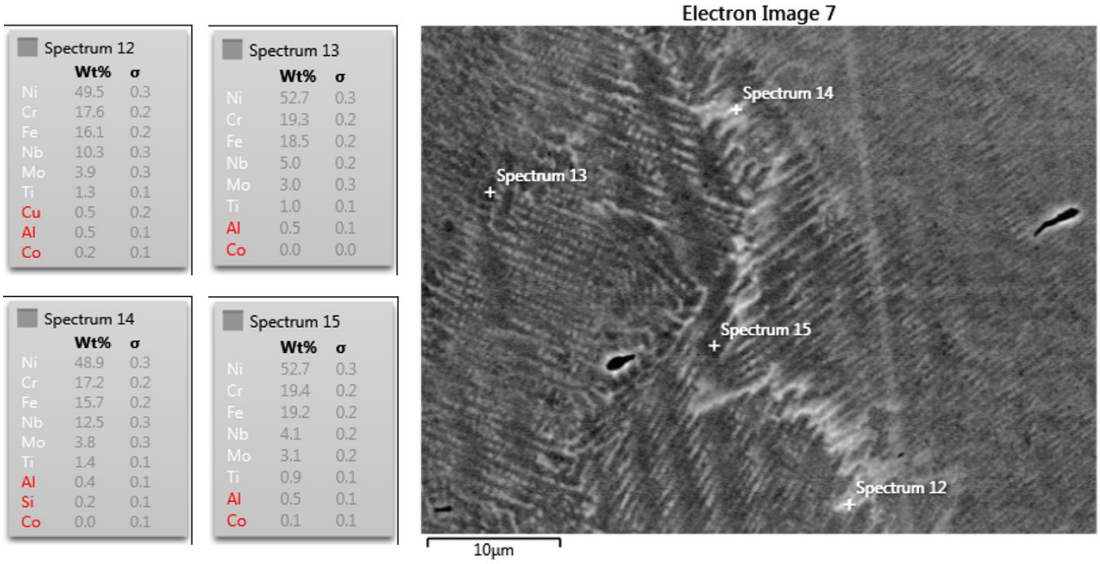


Figure 4.6: Micro-segregation seen in the triangular prism samples (LF1T13). Spectrum 12 and 14 are point and IDs of the white inter-dendritic regions showing higher amounts of Nb, Mo, and Ti.

### Mechanical Properties Characterization

Microhardness measurements were performed on both the LF1T11 and LF1T13 samples, in order to develop a base-line understanding of the effect that the ILTI has on the mechanical properties. A single trace of measurements up the center line of the samples was used. The results are shown in Figure 4.7. It can be seen that there is insignificant change in hardness for both samples, indicating that both the build height and ILTI do not impact the hardness of the material. The average hardness was measured to be 315 HV0.2 and 324 HV0.2, for the LF1T11 and LF1T13 samples,

respectively.

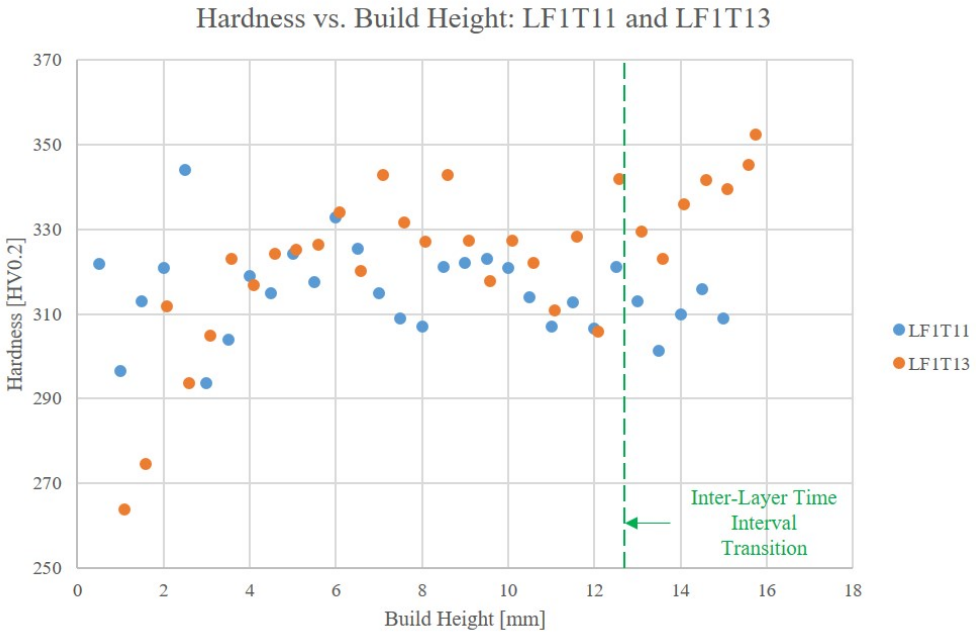


Figure 4.7: Vickers microhardness measurements up the centerline of the triangular prisms. Measurements were spaced by 0.5 mm unless the location was obstructed by excessive porosity.

### Porosity Characterization

The porosity in the triangular prism samples was analyzed visually using both optical microscopy and scanning electron microscopy. The amounts of porosity were not quantified for these samples, but the types and locations of porosity were identified for each of the time intervals, in order to gain insights regarding the formation mechanism. Figure 4.8 shows the various types of pores found in the triangular samples at different time intervals. The majority of pores found below the transition were classified as lack-of-fusion pores shown in Figure 4.8a, while the majority of pores found above the transition were keyhole pores shown in Figure 4.8b. Figure 4.8a highlights a melt pool that failed to fuse to the previous layer below it, resulting in a pore with a sharp corners, as opposed to a round shape. It can be noted that the tip of the triangular prism appears to play a large role in porosity formation, as there are many large circular pores found in that region due to melt pools entering the keyhole mode. Throughout the entire build there were also small circular pores that are not shown in Figure 4.8. These pores can be formed for a multitude of reasons, such as

gas entrapment during processing, poor packing factor of powder, or porosity in the powder feed stock.

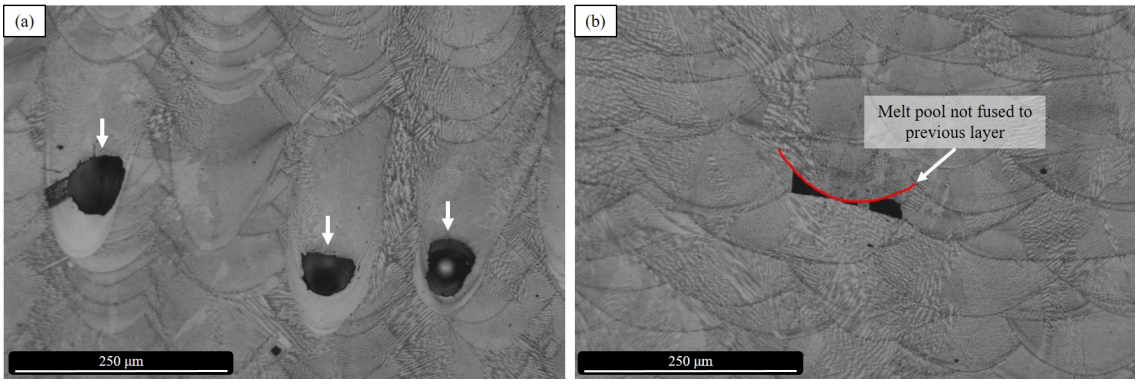


Figure 4.8: Various types of porosity found in the different time interval regions of the triangular prism samples. (a) Keyhole porostiy found near the tip of the triangle indicated by the white arrows, and (b) lack-of-fusion porosity found below the transition in the bottom region. The red line highlights a melt pool boundary that did not fuse to the previous layer.

### 4.1.2 Results from Second Build Design

The samples of interest from this build are the two tall rectangular prisms that were discussed in Section 3.4.2. These are the yellow squares depicted in Figure 3.7. Each of these samples have two step-changes in the ILTI due to samples being completed at build heights of 6.35 mm and 12.7 mm. Figure 4.9 shows the sample geometry along with the ILTIs and where their interfaces are located. It can be seen that at a build height of 6.35 mm the ILTI changes from 126 to 59 seconds, and at a build height of 12.7 mm it changes from 59 to 13 seconds. This time interval of 13 seconds matches the one used in the top of the triangular prism samples that were previously discussed in Section 4.1.1. The difference in these samples is that the cross-sectional area of the part, or in other words the layer scan area, remains constant within each of the three regions. Each region was characterized using various techniques to evaluate the effect of the ILTI.

#### Microstructural Characterization

Similar melt pool behavior that was observed in the triangular prism samples was also discovered in the tall rectangular prism samples (R2 samples as they will be referred to). The melt pools show an abrupt change in shape and stacking when the

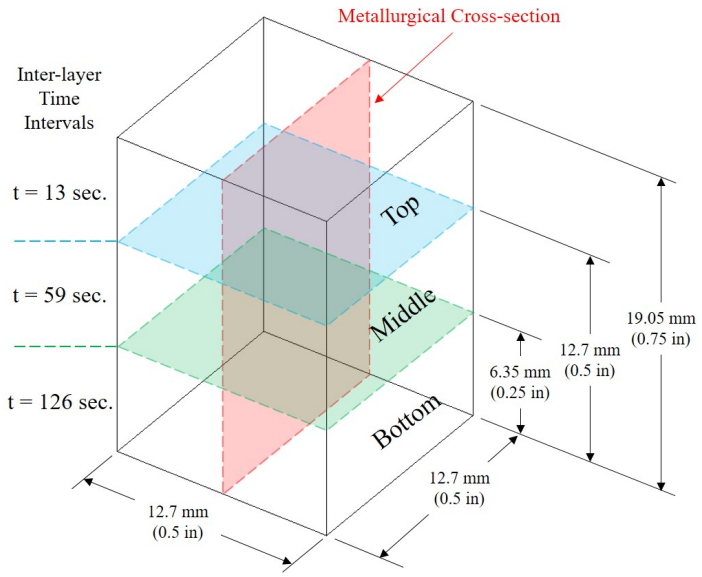


Figure 4.9: Tall rectangular prism sample geometry with inter-layer time intervals at the different regions in the build. The green and blue planes represent where the time interval changes. The red plane is where these samples were sectioned using EDM for metallurgical analysis.

ILTI changes. This was characterized by measuring the melt pool's radii of curvature (ROC) as described in Section 3.2. The result of this characterization is shown in Figure 4.10.

It can be seen from the figure that the melt pool ROC remains relatively unchanged from the bottom to middle regions, averaging 91 µm in the bottom region and 93 µm in the middle region. Therefore, the difference between an ILTI of 126 and 59 seconds is not evident in the shape of the melt pools. However, at further decreases in the ILTI, a significant change in the ROC is observed. At an ILTI of 13 seconds in the top region of the samples, the ROC is found to average 54 µm. This results in a percent change of -41%. At an ILTI somewhere between 59 and 13 seconds there is a significant change in the process, affecting the melt pool behavior.

Figure 4.10 also shows micrographs of the melt pools in the top and middle regions. It can be observed that the stacking of the melt pools differ going from the middle to the top regions. It should be noted that the bottom and middle regions exhibits similar melt pool stacking. Recalling the scan strategy used in the production of this build, discussed in Section 3.4, the melt pools should be stacked one on top of the other. The top region of the R2 samples, shown in Figure 4.10a, has melt pools that are near perfectly stacked on top of one another. The middle region on the other hand, shown in Figure 4.10b, has melt pools that are more staggered in appearance.

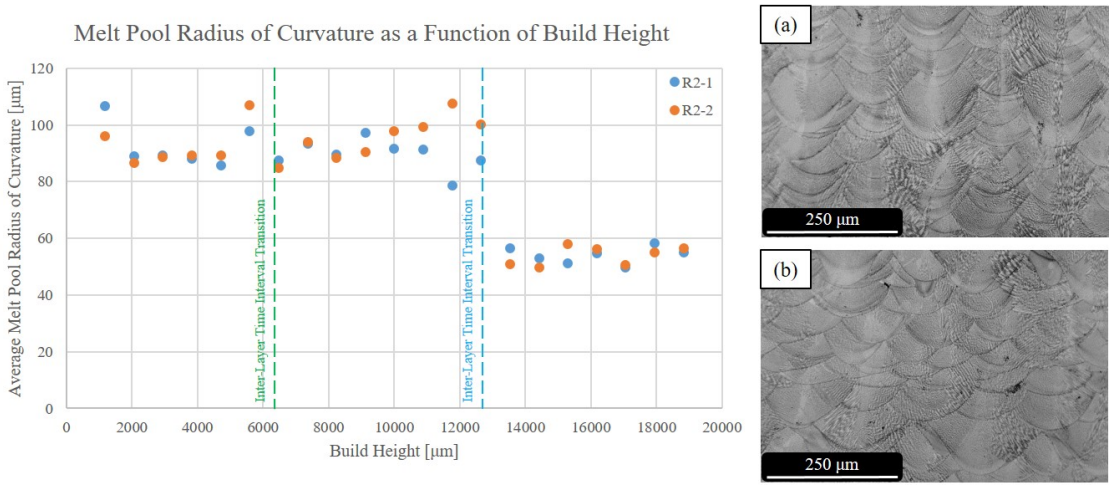


Figure 4.10: Melt pool radius of curvature as a function of build height for the tall rectangular prism samples built from the second build design. (a) Micrograph of melt pools in the 13 second time interval (top region) and (b) micrograph of melt pools in the 59 second time interval (middle region).

Given the sizable difference in the melt pools of the builds, the microstructure was characterized further using EBSD. The EBSD data was used to analyze the grain size and shape, as well as the texture of the material. Each R2 sample was scanned three times, once in each of the three ILTI regions. The scan direction inverse pole figure (SD-IPF) maps for each of these regions are shown in Figure 4.11.

Figure 4.11 shows the grain structure in each of the time interval regions for both R2 samples. From a visual perspective, the two samples are similar in grain size and shape for the bottom and middle regions, while the top regions show minimal variation. It can be observed in the top region of R2-1 that the grains are very columnar and stacked one on top of another with smaller, thinner grains separating them laterally. These grains can be correlated to the melt pools, where the thin 'separator' grains are aligned with the centers of the melt pools. This will be covered further in the discussion section to follow. In the top region of the R2-2 samples there are similar columnar grains, however they sometimes grow into an adjacent column of grains unlike R2-1. Given the fallibility of the human eye, further grain size and shape information obtained from EBSD and the OIM software is shown in Table 4.2.

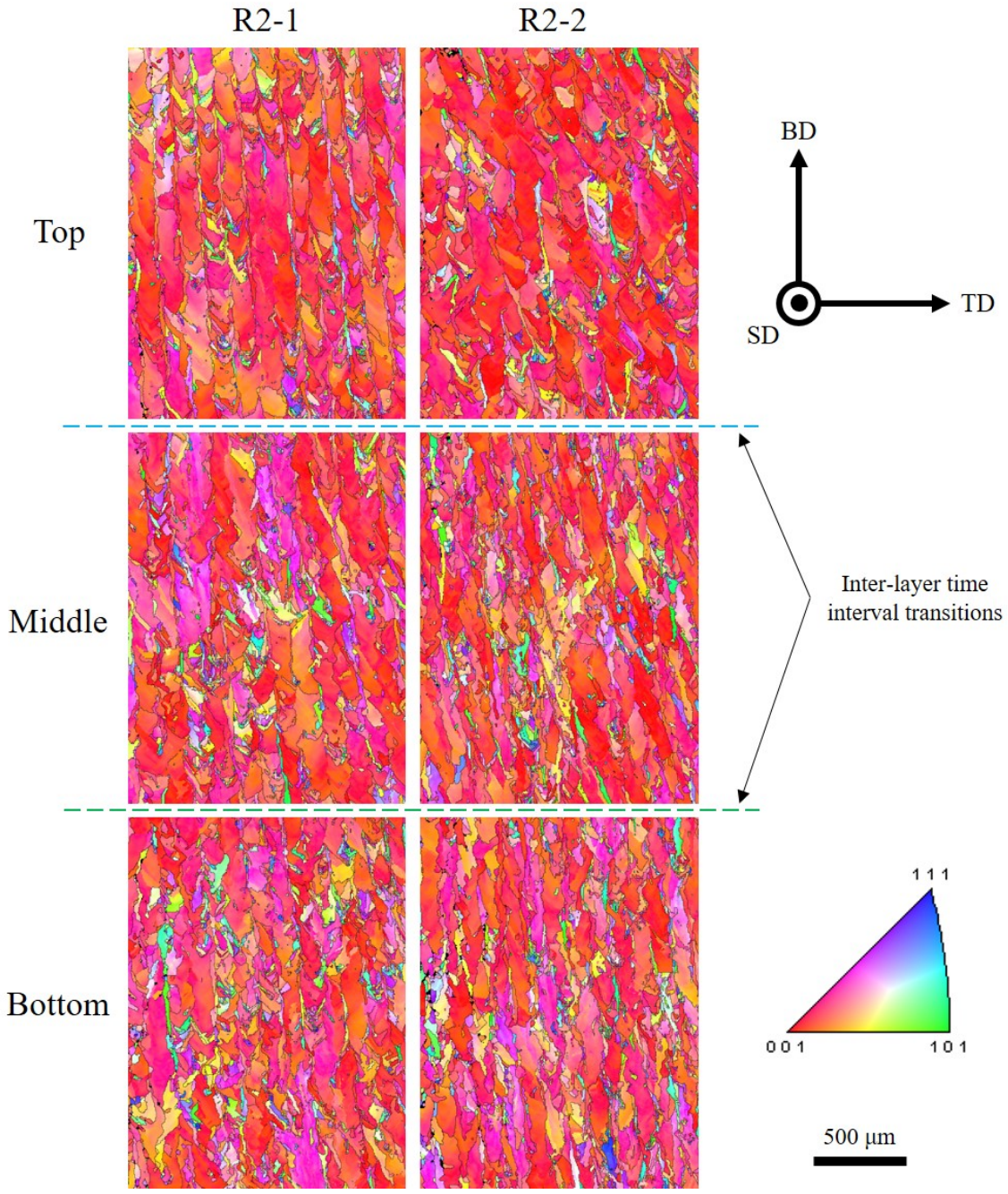


Figure 4.11: SD-IPF maps for the bottom, middle, and top regions in two different tall rectangular prism samples.

Table 4.2: Average grain sizes for the tall rectangular prism samples obtained from OIM post-processing software.

| **Grain Size Information** | **R2-1** | | | **R2-2** | | |
|---|---|---|---|---|---|---|
| | **Bottom** | **Middle** | **Top** | **Bottom** | **Middle** | **Top** |
| Horizontal Intercept Length [μm] | 24 | 26 | 26 | 23 | 22 | 27 |
| Vertical Intercept Length [μm] | 37 | 40 | 44 | 41 | 40 | 40 |
| Average Grain Area [$\mu m^2$] | 1101 | 1310 | 1331 | 1136 | 1097 | 1394 |

From Table 4.2 it can be seen that the grain size increases slightly from the bottom region to the top region. While the change in intercept lengths is minimal, the change in grain area is sufficient to signify a change in grain size. It can also be noted that the horizontal intercept length for sample R2-2 shows a larger increase from the middle to the top regions. This quantitatively suggests that the large columnar grains grow into the adjacent columns.

Pole figures were also obtained through the OIM post-processing software in order to provide information about the material's texture. The pole figures represent texture in the build direction-transverse direction (BD-TD) plane and are shown in Figure 4.12. The texture that developed in the SLM process is a 45 degree rotated cube texture, (001)[100] oriented in the scan direction. It can be seen by the maximum values of the pole figures that the texture strengthens when the ILTI decreases.

Electron dispersive spectroscopy (EDS) was also performed on both R2 samples at each of the regions; bottom, middle, and top. Area scans were taken in order to see if the ILTI had any effect on the bulk composition of the material. All major alloying elements were found to be within the compositional ranges of IN718 for every region. At high magnification, micro-segregation was found at varying degrees throughout each sample, similar to the triangular prism samples from previous build design.

### Mechanical Properties Characterization

A microhardness trace up the center-line of both R2 samples was performed in order to characterize the effect that the time interval has on mechanical properties.

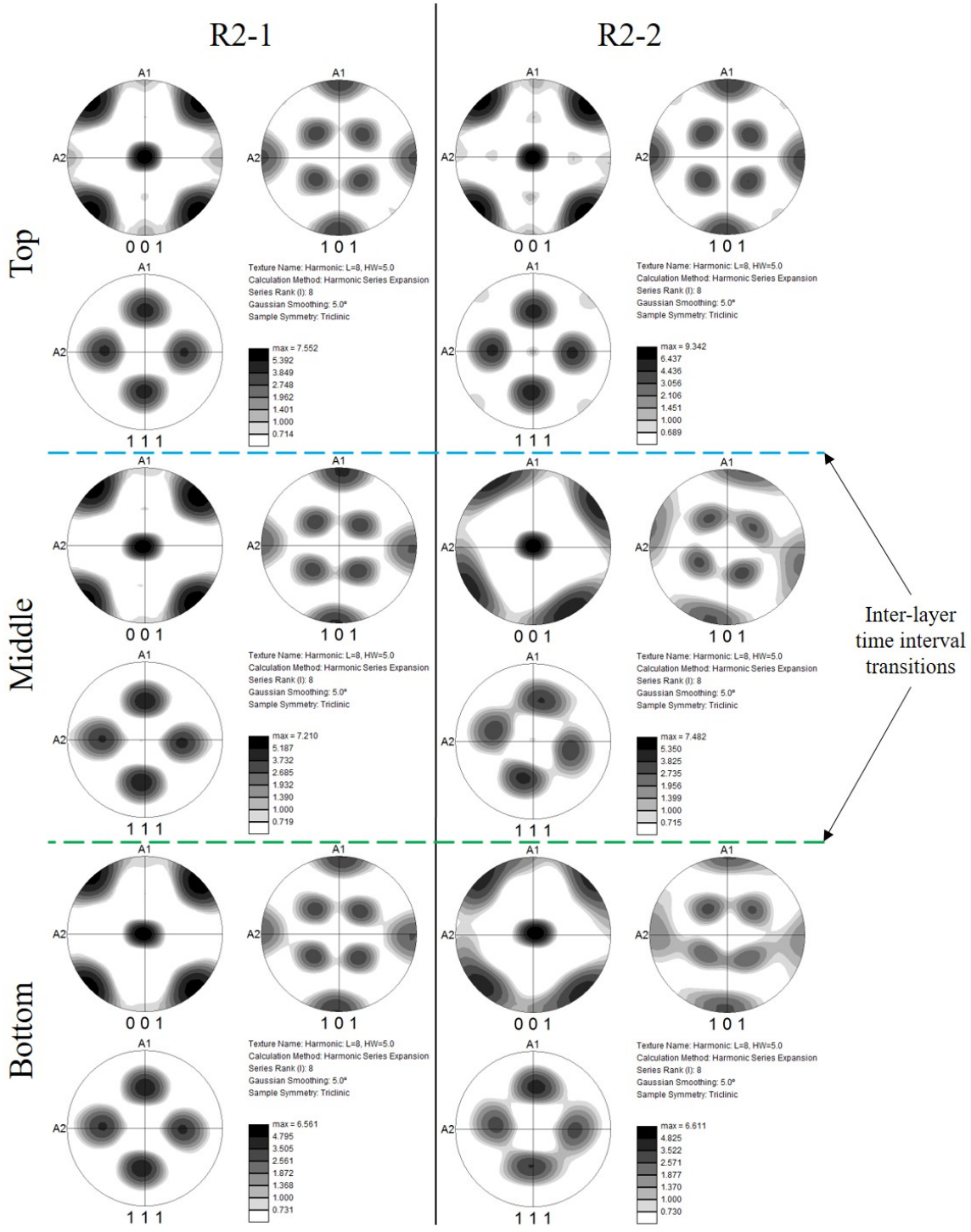


Figure 4.12: TD-BD pole figures obtained at eack of the three scan regions for each tall rectangular prism sample.

The results are shown in Figure 4.13. It can be seen that the microhardness showed no statistically significant change due to build height or ILTI. The average hardness was found to be 314 HV0.2 and 316 HV0.2 for the R2-1 and R2-2 samples, respectively. Essentially no change in the material's hardness is expected after seeing no bulk compositional changes from EDS. In order to confirm that these hardness values at a specific build height were accurate and not changing in the lateral direction, a grid of 3 by 8 indents was performed on the R2-1 sample. These indents were laterally and vertically spaced by 2 mm. It was found that the hardness measurements do not vary laterally, confirming that the single wide indent trace was an accurate representation.

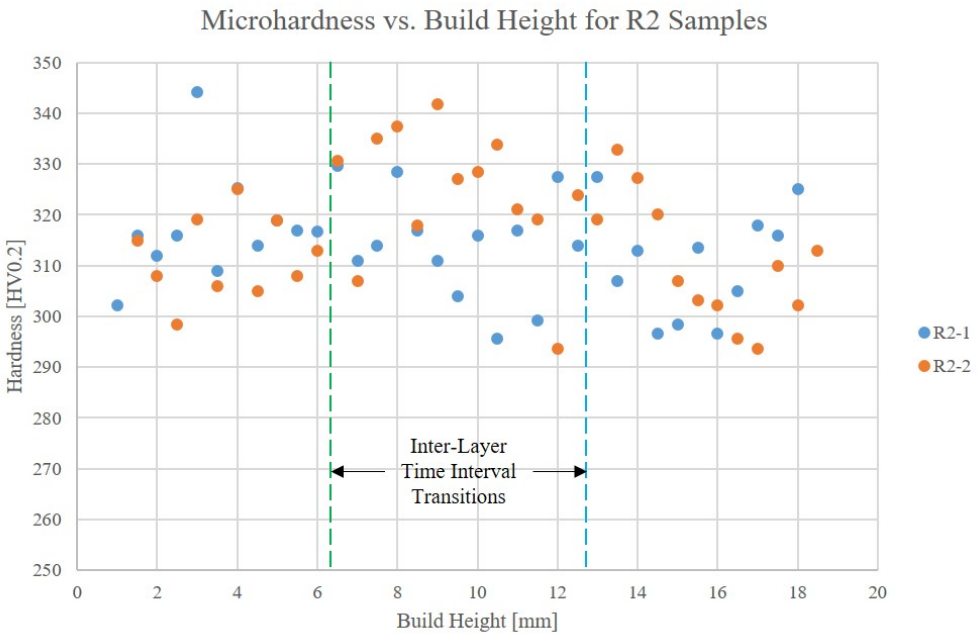


Figure 4.13: Vickers microhardness measurements up the centerline of the tall rectangular prisms. Measurements were spaced by 0.5 mm.

In addition to hardness testing, tensile samples were built within two ILTIs; 126 and 59 seconds. Samples were tested as discussed in Section 3.2. The resulting stress-strain curves are shown in Figure 4.14, and the yield strengths, tensile strengths, elastic moduli, and elongations are reported in Table 4.3. Note that the 0.5-1 specimen failed inside of the grip section, and therefore was omitted.

It can be observed in both Figure 4.14 and Table 4.3 that the tensile properties vary between each sample, showing no clear difference due to the two different time intervals. It should be noted that samples labeled 0.25 were within the 126 second time interval, while samples labeled 0.5 were within the 59 second time interval. There may however be a slight difference in the samples' elongation, where the '0.5' samples

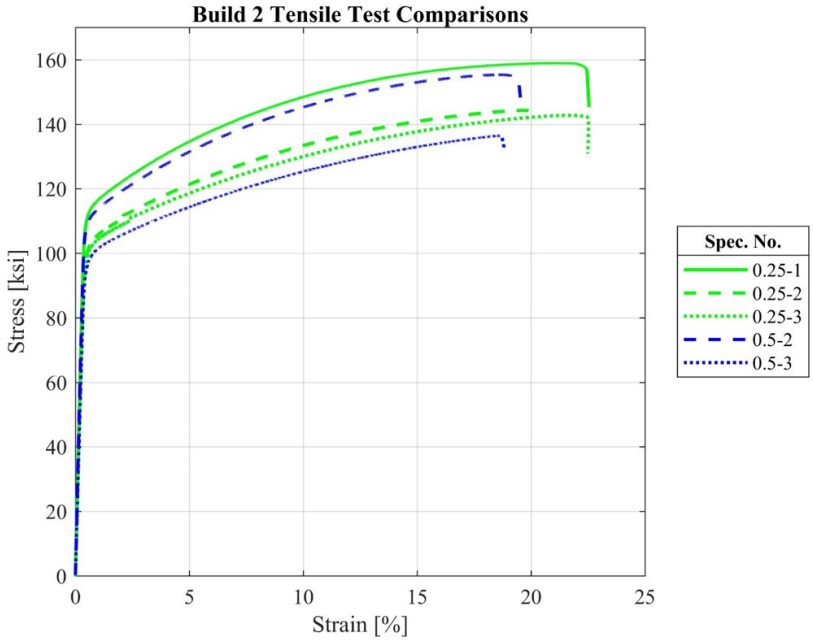


Figure 4.14: Stress-strain curves for the second build design samples.

Table 4.3: Tensile properties obtained form the tensile testing of the samples produced in the second build design.

| Specimen Number | ILTI [s] | UTS [ksi] | YS [ksi] | E [Msi] | e [%] |
|---|---|---|---|---|---|
| 0.25-1 | 126 | 159.0 | 112.0 | 30.0 | 23 |
| 0.25-2 | 126 | 144.3 | 101.5 | 26.9 | 20 |
| 0.25-3 | 126 | 142.8 | 100.3 | 26.5 | 23 |
| 0.5-1 | 59 | - | - | 24.7 | - |
| 0.5-2 | 59 | 155.4 | 109.8 | 29.8 | 20 |
| 0.5-3 | 59 | 136.4 | 97.5 | 25.7 | 20 |

seem to have slightly less elongation than the '0.25' samples. This may be due to the varying levels of porosity found in each of the regions. It is important to note that tensile samples built with an ILTI of 13 seconds were not able to be produced due to various reasons. From the testing of such samples it is expected that more substantial differences would be observed.

### Porosity Characterization

Varying levels of porosity were discovered in samples on this build. The porosity found in the R2 samples was characterized using optical and scanning electron microscopy, as well as x-ray computed tomography (XCT). Most of the melt pools

observed in the R2 samples were not in proximity to the keyhole region, therefore keyhole porosity was not found in the cross-sections that were analyzed, however, both lack-of-fusion and gas-filled pores were found. In order to quantify the different levels of porosity due to the different ILTIs, XCT slices were used to count number of pores per area. This analysis was performed as described in Section 3.2 averaging 10 XCT slices per region spaced 500 µm apart. The results are shown in Figure 4.15.

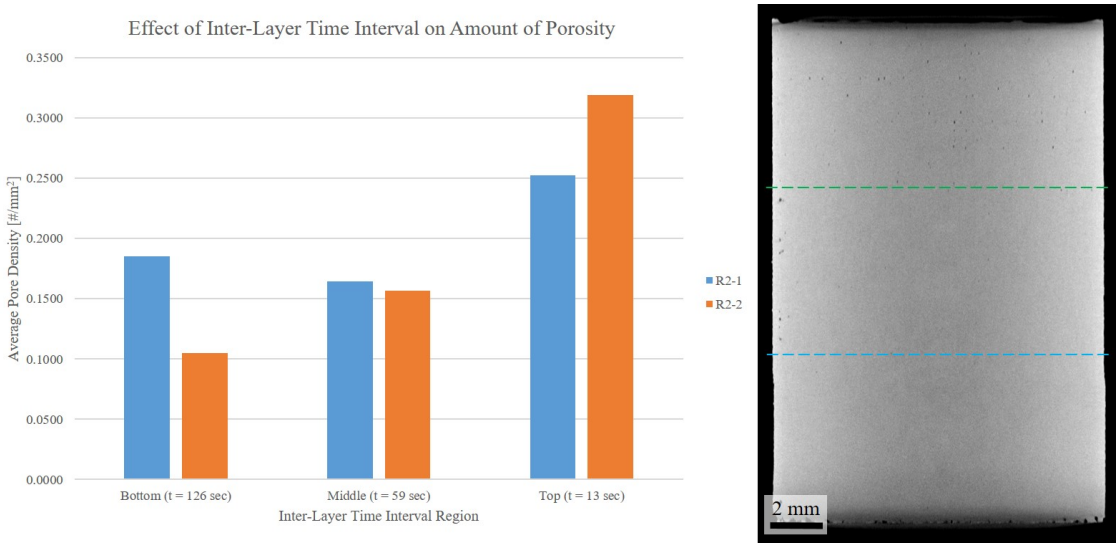


Figure 4.15: Pore density calculated using XCT data for each of the three inter-layer time intervals.

It is shown in this analysis that there is a greater population of pores in the top region (13 second time interval) than any of the other regions. It should be noted that the edge porosity caused by different border parameters, as well as laser starts and stops were not included in this analysis. These numbers represent the bulk of each region. It is also important to note that the resolution of the XCT scan was about 11 µm, therefore any pores below that size would not show up in the data and are not included in the analysis.

From Figure 4.16 it can be observed that different types of pores are found in all regions. Gas-filled porosity was found in all three regions and is shown in Figure 4.16a and c for the top and middle regions, respectively. Lack-of-fusion porosity was also found throughout the entire build and is shown in Figure 4.16b and d for the top and bottom regions, respectively. Keyhole porosity was not observed in the metallurgical cross-section shown, unlike the what was observed at the top of the triangular prism samples.

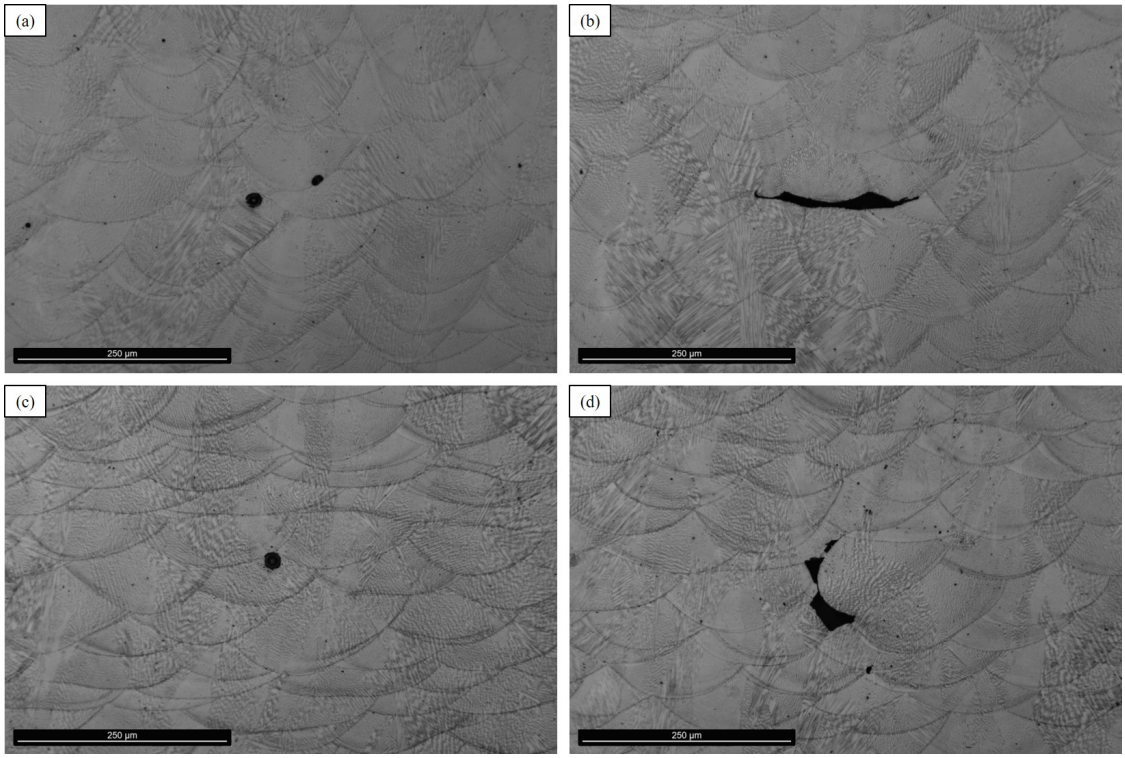


Figure 4.16: Various types of pores found in the tall rectangular prism samples. The micrographs show (a) gas-filled porosity found in the top region, (b) lack-of-fusion porosity found in the top region, (c) gas-filled porosity found in the middle region, and (d) lack-of-fusion porosity found in the bottom region.

## 4.2 Discussion

### 4.2.1 Melt Pools

Analysis of the melt pools that comprise a SLM build can give an immense amount of information regarding the scan strategy, welding mode, and amount of remelt. Data was collected on the melt pools' staggering, as well as their radii of curvature in order to provide this type of information.

**Melt pool staggering**, or the organization of scan tracks from layer to layer, was found to be different throughout the several builds discussed above. Based on the scan strategy used (shown in Section 3.4), the melt pools should reside one on top of the other for the entire build height. This would result in the columnar formation of melt pools as observed in the upper region of the triangular prism samples. A summary of the melt pool staggering within the triangular prism and tall rectangular prism samples is shown in Figure 4.17.

In this figure the yellow lines represent the intended locations of the melt pool

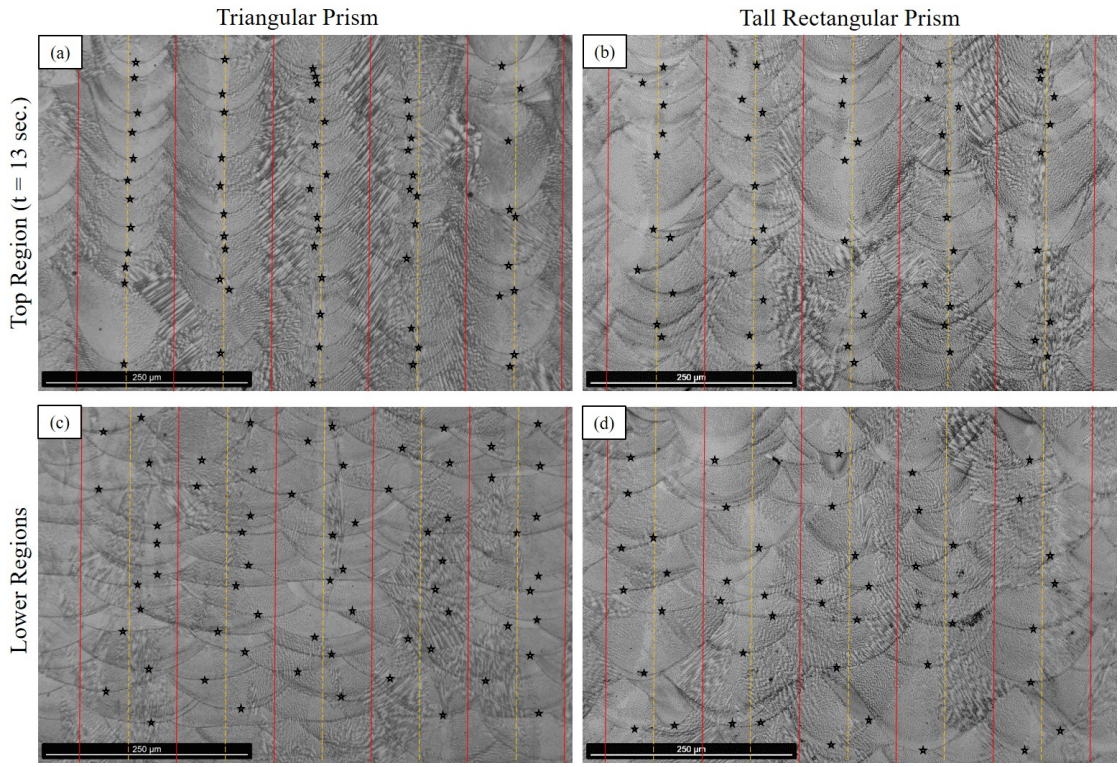


Figure 4.17: Various degrees of melt pool staggering found in both the triangular prism samples and tall rectangular prism samples. The yellow lines represent the inteded melt pools centerlines spaced 120 µm appart (hatch spacing) and the red lines separate the melt pool columns. The black stars are placed on the bottom of each melt pool indicating its actual centerline. This is shown for the (a) triangular prism top region, (b) rectangular prism top region , (c) triangular prism lower region, and (d) rectangular prism middle region.

centerlines, or in other words the designed scan strategy, and the black stars are the actual locations of each melt pool's center. The top region of the triangular prism samples, shown in Figure 4.17a, has nearly perfect column registration of the melt pools. The top region of the tall rectangular prism samples, shown in Figure 4.17b, appears to decrease in the column registration when compared to the triangular prism's top region. Both of these regions have an ILTI of 13 seconds, therefore the ILTI can be ruled out as the cause for this difference. The only major difference between the regions is the geometry. The triangular geometry could play a role in added heat accumulation as compared to the rectangular prism, potentially leading to this difference. It is expected that the lower regions away from the edges of the sample would experience similar heat accumulation to the rectangular sample, however, the top of the triangle begins to greatly reduce the cross-sectional slice area, reducing the path for the conduction of heat.

When comparing the top and lower regions there is a large difference in the organization of melt pools. The lower regions of both the triangular prism and tall rectangular prism samples have staggered melt pools such that melt pools on consecutive layers do not sit one on top of the other. It can be observed in Figure 4.17 that the top region's melt pool centerlines are near or on the designed scan track line shown in yellow, while the lower region's melt pool centerlines vary from being on the designed scan track line to about 50 μm offset. The only differences between the top and lower regions are the ILTI and the build height, both of which could play a role in this staggering difference.

It was found that for samples with constant ILTIs the melt pool staggering experienced negligible change throughout the build height. Therefore, the abrupt change in melt pool staggering seen in the top regions is dominated by the ILTI. One possible explanation for this is that the top regions have the same amount of melt pool staggering as the lower regions, but are much deeper, causing more remelt and hiding the staggered appearance. It is suspected that the mode of welding changes when going from longer ILTIs to an ILTI of 13 seconds. This mode change from conduction mode to transition mode is what causes the melt pools to be deeper and hide this appearance. This change in melt pool mode will be further discussed in the next section. Additional data and experiments are needed to further understand the staggering seen in these samples.

**Melt pool shape** was also found to change in the different regions of the samples of interest. Traditionally melt pool shape is defined by its width and depth, however with multi-layer builds this information is difficult to obtain. For this reason the radii of curvature at the bottom of the melt pools were measured in order to give information on the melt pools' shapes. A large radius of curvature would indicate the width being greater than the depth, which is characteristic of conduction mode welding. A small radius of curvature would indicate the depth-to-width ratio is increasing, which would be seen when entering the transition and keyhole modes of welding.

It was shown in Section 4.1, that the radius of curvature decreases when the ILTI reaches 13 seconds. Comparing the top regions of the triangular prism and the tall rectangular prism, the average radii of curvature are 59 μm and 54 μm, respectively. The melt pool radii of curvature in the bottom and middle regions of the tall rectangular samples are very similar, averaging 93 μm. The radii of curvature in the lower region of the triangular prism averaged 131 μm. These lower region radii of curvature are on the same order of magnitude and may only differ due to the geometry of the sample.

In order to better understand this melt pool behavior, thermal modeling was done to compare theoretical melt pool shapes to the actual ones seen in this study. There are several ways that this is done in literature, from analytical models [80, 81, 82] to computational models [83, 84]. For this research analytical models were explored. The Rosenthal model for temperature fields produced by a traveling point source was first explored to look at the effect heat accumulation has on the melt pool shape [80]. From the Rosenthal solution, an equation for the melt pool width and depth can be obtained shown in Equation 4.2.1 [85, 86],

$$W/2 = \sqrt{\frac{2Q}{e\pi\rho C(T_m - T_0)v}} \tag{4.2.1}$$

where W is the melt pool width, Q is the product of laser absorptivity and laser power ($Q = AP$), e is Euler's number, ρ is the material density, C is the specific heat, $T_m$ is the melting temperature, $T_0$ is the initial temperature, and $v$ is the scan speed of the heat source. In this model, melt pool depth is assumed to be half that of the melt pool width. From this equation the melt pool width and depth are plotted against the initial temperature of the surrounding material using Inconel 718 thermal properties and the actual process inputs used in the builds. This is shown in Figure 4.18.

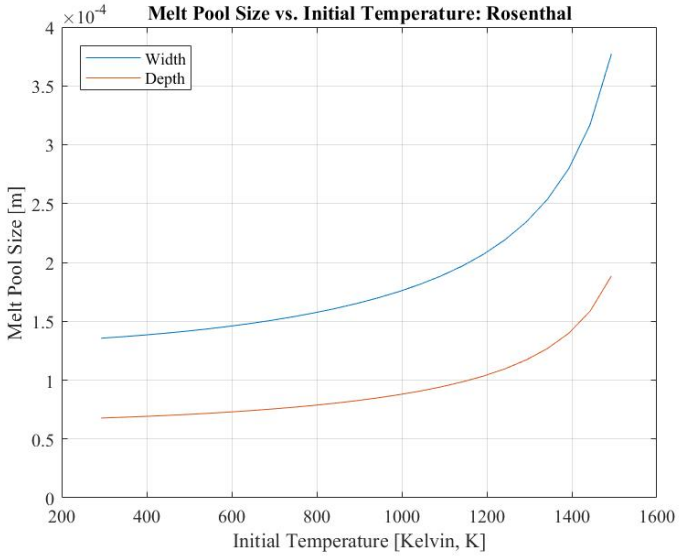


Figure 4.18: Melt pool width and depth vs. initial temperature of the surounding material using the Rosenthal model.

It can be seen that with increasing background temperature the size of the melt pool increases, however the Rosenthal model assumes a semi-circular melt pool caus-

ing the depth to always be half that of the width. Therefore this model is limited in capturing the melt pools radius of curvature and aspect ratio.

For this reason, the Eagar-Tsai model for temperature fields produced by a traveling distributed heat source was used [81]. This model is a modification of the Rosenthal model using a Gaussian distributed heat source as opposed to a point source. The solution of the temperature distribution for a Gaussian heat source moving on a semi-infinite plate with no change in phase is given in Equation 4.2.2,

$$T - T_0 = \int_0^t dt'' \frac{Q}{\pi\rho C(4\pi a)^{\frac{1}{2}}} \frac{t''^{-\frac{1}{2}}}{2at'' + \sigma^2} e^{-\frac{w^2+y^2+2wvt''+v^2t''^2}{4at''+2\sigma^2} - \frac{z^2}{4at''}} \tag{4.2.2}$$

where T is the temperature at any location within the semi-infinite plate, $T_0$ is the initial temperature of the surrounding material, Q is the product of absorptivity and power ($Q = AP$), $\rho$ is the material density, C is the specific heat, a is the thermal diffusivity calculated by $a = \frac{k}{C\rho}$, k is the thermal conductivity, $\sigma$ is the distribution parameter or heat source radius, $v$ is the scan speed of the heat source, w is the distance in the x-direction in a moving coordinate of speed $v$ ($w = x - vt$), y is the distance in the y-direction, z is the distance in the z-direction, and t" is a simplifying term of time. The values used in the following analysis are given in Table 4.4.

Table 4.4: Thermal properties for IN718 used in the Eagar-Tsai Analysis.

| **Thermal Property** | **Variable** | **Value/$T_0$ Dependent Equation** |
|---|---|---|
| Laser Absorptivity | A [%] | 0.3 (minimum) [87] |
| Laser Power | P [W] | 200 |
| Density | $\rho$ [g/m$^3$] | (-3.923x10$^2$)$T_0$ + 8.305x10$^6$ [88] |
| Specific Heat | C [J/gK] | (2.044x10$^{-4}$)$T_0$ + 0.38116 [88] |
| Thermal Conductivity | k [W/mK] | -0.676 + 0.0332$T_0$ + (-9.000x10$^{-6}$)$T_0^2$ [88] |
| Laser Beam Radius | $\sigma$ [m] | 4.0x10$^{-5}$ |
| Laser Scan Speed | $v$ [m/s] | 0.9 |

The temperature fields were plotted as contour plots using MATLAB for initial temperatures ranging from 298 K or room temperature, to 1198 K, at an interval of 100 K. This produced ten temperature field plots that show the effect of the initial temperature on the melt pool shape, one of which is shown in Figure 4.19.

Figure 4.19 shows the temperature field for the SLM processing of IN718 when the initial temperature of the surrounding material is at room temperature, 298 K. All three planes are shown in order to get an accurate measurement of the maximum width and depth, as well as the radius of curvature. It should be noted that this

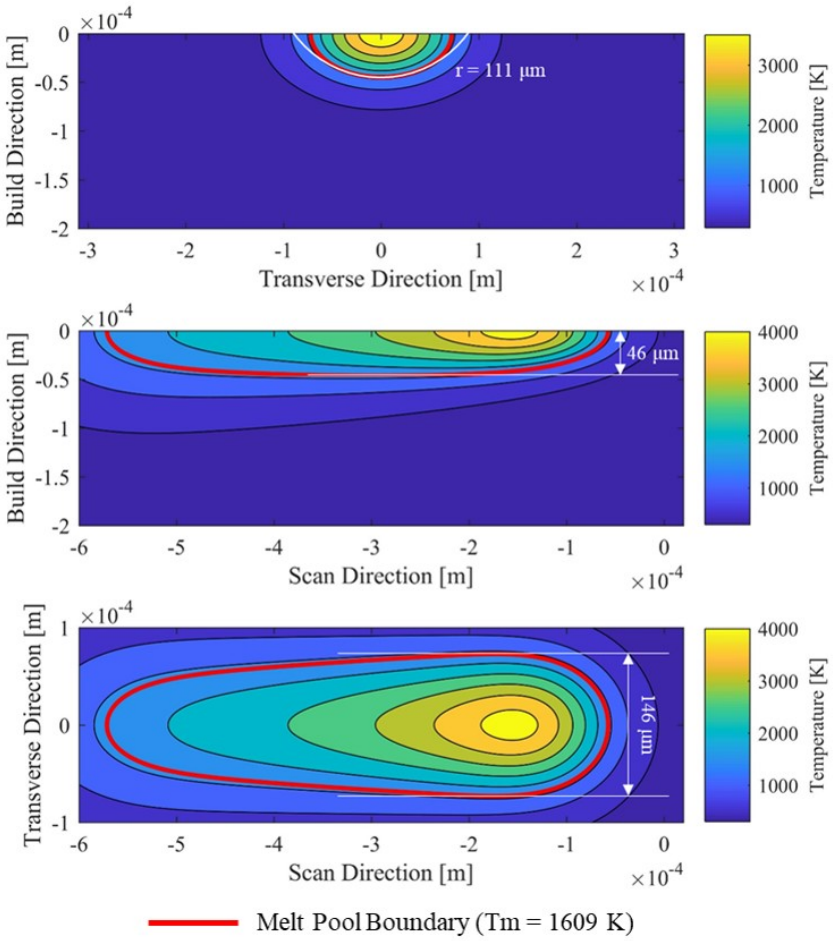


Figure 4.19: Temperature field for the SLM processing of IN718 at an initial temperature of 298 K produced using the Eagar-Tsai solution. The TD-BD, SD-BD, and SD-TD planes are shown in the top, middle, and bottom plots respectively. The red contour line represents the melt pool boundary plotted at 1609 K and melt pool width, depth, and radius of curvature are measured.

solution does not predict an infinite temperature at the center line of the melt pool as the Rosenthal solution does, however, temperatures may often exceed the boiling temperature of the metal, which is not realistic [81]. It can be seen in Figure 4.19 that the center of the melt pool reaches a temperature of 4000 K. While this is not accurate, it does not affect the melt pool boundary which is the primary interest of this study.

These measurements of melt pool depth, width, and radius of curvature were made for the ten different initial temperatures. The melt pool dimensions were then plotted against the initial temperature in order to be evaluated. These plots are shown in Figure 4.20 along with the melt pool's aspect ratio.

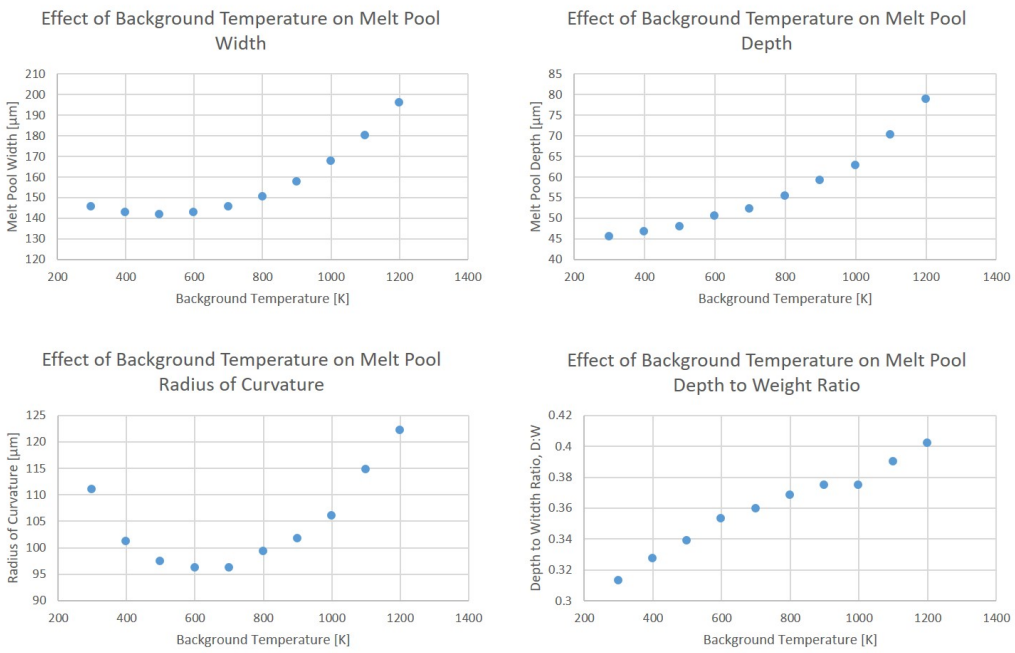


Figure 4.20: Melt pool width, depth, radius of curvature, and aspect ratio vs. the initial temperature of the surroundings.

It can be seen that the melt pool width and radius of curvature initially decrease as the initial temperature increases, but then begin to increase after about 600 K. Both the depth and aspect ratio continually increase as the initial temperature increases. When the ILTI decreases to 13 seconds there is less amount of time for the part to fully cool, leading to heat accumulation that results in a deeper melt pool with a depth to width ratio greater than 0.5. The Eagar-Tsai model does not predict this due to its limitation to conduction mode welding.

Conduction mode welding is one of two welding modes and occurs at low laser energy densities. The melt pool that is created is usually more stable, reducing the number of defects. At higher laser energy densities the melt pool enters keyhole mode, which is less stable causing porosity and material evaporation [27]. Qi et al. determine that there is a transition mode that bridges the gap between conduction and keyhole modes. They show that the melt pool depth to weight ratio remains relatively constant in conduction mode, then increases throughout the transition mode before reaching a maximum in keyhole mode [89]. This provides evidence that the melt pools in the top regions of the sample in this study are no longer in conduction mode and are more than likely somewhere in the transition mode.

It should be noted that the Eagar-Tsai model does accurately predict the size and shape of the melt pools in the lower regions. As mentioned before, the melt pool

width and depth are difficult to measure in a multi-layer build, however the width should be greater than the hatch spacing (120 μm) to allow for sufficient overlap, and the depth should be greater than the layer thickness (30 μm) to allow for remelt of the previous layer. For an initial temperature of 298 K, the melt pool width was predicted to be 146 μm and the depth was predicted to be 46 μm, both of which are greater than their respective process parameter, making them realistic values. As for the melt pool radius of curvature, the Eagar-Tsai model was able to predict a value very comparable to the values measured using optical microscopy. The radius of curvature predicted in the model for an initial temperature of 298 K was 111 μm, while the measured values averaged 93 μm and 131 μm for the bottom regions of the tall rectangular prism and the triangular prism samples, respectively.

### 4.2.2 Porosity

As discussed briefly in the above melt pool subsection, the welding mode, either conduction, transition, or keyhole, can play a large role in the amount and types of porosity that arise in the SLM process. Conduction mode has a relatively stable melt pool that reduces the generation of gas-filled porosity. However, because of the lower penetration depth characteristic of conduction mode welding, lack-of-fusion porosity between consecutive layers is more common. Keyhole mode welding is characterized by a high aspect ratio melt pool that is highly unstable, causing both material evaporation and gas entrapment. The transition mode is the middle ground between the two modes, where the depth-to-weight ratio is increasing.

It was found using XCT analysis that the upper regions of the tall rectangular samples had a larger population of porosity than the lower regions. In fact, at a 13 second ILTI the population of porosity was nearly doubled when compared to the 59 and 126 second regions. It was stated above that the top region was most likely in the transition welding mode because of its melt pool shape, while the bottom regions were most likely in the conduction mode due to their agreement with the Eagar-Tsai model. This difference in welding mode could explain the difference in the amount of porosity, since the transition mode is more unstable than conduction mode, resulting in a larger population of gas-filled pores to arise.

No trends were found in terms of a specific type of porosity in a certain region. Both lack-of-fusion and gas-filled porosity was found in all regions of the triangular prism and tall rectangular prism samples. One difference between the two sample geometries was the fact that the melt pools at the very tip of the triangular prism

entered the keyhole mode, seen in Figure 4.8. These keyhole welds often contained a large gas-filled pore in the tip of the melt pool. Keyhole welds of this magnitude were not observed in the tall rectangular prism samples, therefore the sample geometry of the triangular prism sample had to have played a major role. At the tip of the triangular prism samples the solidified material is surrounded by powder and gas, which provide cooling through conduction, radiation, and convection. However, heat transfer through these modes are minimal compared to the conduction of heat through the previously deposited layers. With conduction through the sample being the dominant component of heat dissipation, a continuously decreasing cross-sectional scan area will give heat a smaller path to dissipate through, leading to slower cooling. This would result in higher temperatures at the tip of the triangular prism sample, leading to the formation of keyhole welds.

### 4.2.3 Grain Size and Shape

The microstructure of a SLM build is generally composed of fine columnar grains elongated in the build direction. For the two sample geometries in this study this was found to be the case. However, as the ILTI decreased there were differences in the grain size and shape.

Comparing all lower regions of the two build geometries, the grain size and shape were approximately the same. The samples exhibited a columnar grain structure with randomly distributed fine, more equiaxed grains. The small variation in grain size and shape came when the time interval dropped to 13 seconds for both sample geometries. The grain structure was characterisitcally more columnar than the lower regions, where very tall, thin grains grew along the center line of the melt pools in the build direction through multiple layers, and thicker columnar grains filled the gap between them. This microstructure is seen in literature for samples that are built with scan tracks directly on top of one another [90, 91, 63]. These two grain shapes are due to thermal gradients within each melt pool and the epitaxial growth that occurs from layer to layer. This will be discussed in more detail in the next section.

The reason for this change in grain structure could be due the difference in melt pool staggering discussed above. Accuracy in the melt pool alignment will aid in the formation of grains from the existing underlying material layer. The bottom regions in these samples had more staggered melt pools which exhibited a reduced level of epitaxial growth, resulting in slightly smaller columnar grains and the formation of a larger population of fine, equiaxed grains. This is a result of a balance between

epitaxial growth of grains and nucleation of new grains.

Since it is clear that these grains closely follow the melt pool ordering, their size will be greatly determined by the scan strategy parameters such as hatch spacing. The tall, thin grains that run up the center line of the melt pool stacks are spaced by approximately 120 μm, which is the hatch spacing in these samples. Therefore the width of the grains that fill the area between the tall, thin grains will generally have similar widths on the order of 100 μm. The grain heights however, are determined by the degree of epitaxial growth from layer to layer or if the nucleation of new grains occurs. This is dependent on both the melt pool staggering and the amount of remelt into the previous layer.

### 4.2.4 Texture

The crystallographic texture of these samples was analyzed using EBSD. The results show that there are two main texture components throughout the samples. The stronger of the two textures is a cubic component rotated 45 degrees about the scan direction (SD), with $< 001 >$ in the SD. The second component is a cubic component where the $< 001 >$ is aligned in the build direction (BD) and scan direction (SD). These crystallographic orientations are shown in Figure 4.21.

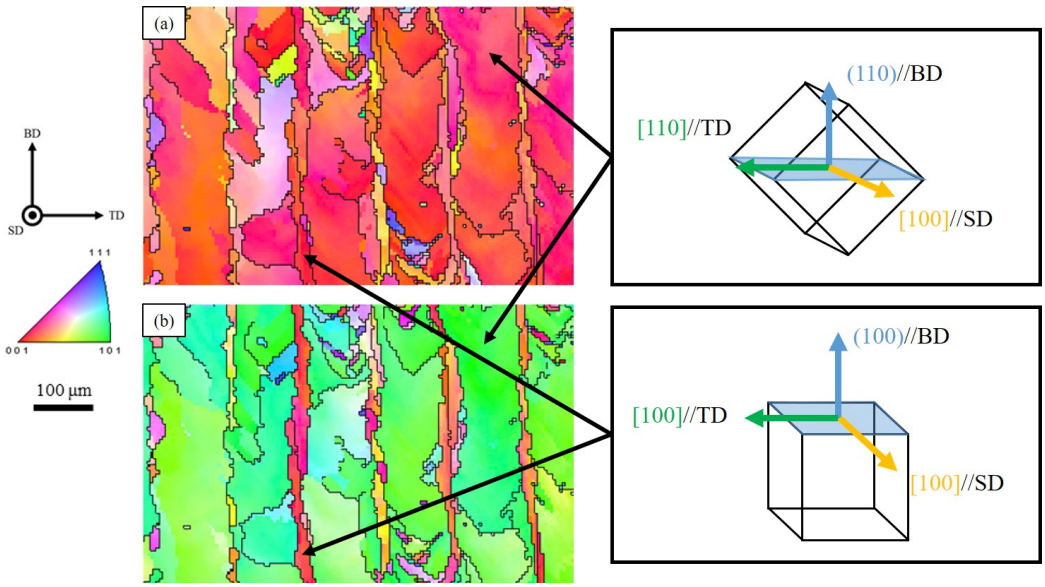


Figure 4.21: Representation of the crystallographic texture present in the samples in this research where (a) is a SD-IPF map and (b) is a BD-IPF map

The rotated cube component is seen in the wider grains that form in the overlap regions of the melt pools. The non-rotated cubic component is seen in the thin grains

that run along the center line of the stacked melt pools. Figure 4.21a is a SD-IPF map, showing that both grain types present a cubic texture, $\{100\} < 001 >$, in this direction denoted by the red color. Figure 4.21b is a BD-IPF map, showing that the wider grains present a Goss texture, $\{110\} < 001 >$, in the build direction and the thin grains have a cubic texture in the build direction represented by green and red, respectively.

It is known from solidification theory that the preferred growth direction of a FCC crystal is $< 001 >$ and that grain growth occurs in the direction of the greatest thermal gradient. Thermal gradients can arise from several different factors, but most influential are the thermal gradients formed in the scan direction and radially within the melt pool. For both crystallographic orientations talked about above, the $< 001 >$ direction is aligned with the scan direction due to the thermal gradient induced by the high scan speed. The difference between the two texture components is explained when looking at the thermal gradients within the melt pool. The thermal gradients within a melt pool are radial, where the lowest temperature is at the melt pool boundary and the highest is at the center of the melt surface. Therefore, crystal growth occurs perpendicular from the melt pool boundary toward the center of the melt surface. This causes crystal growth to occur in a variety of directions that are dependent on the melt pool shape. Figure 4.22 depicts this grain growth specifically for the top regions of the samples in this study.

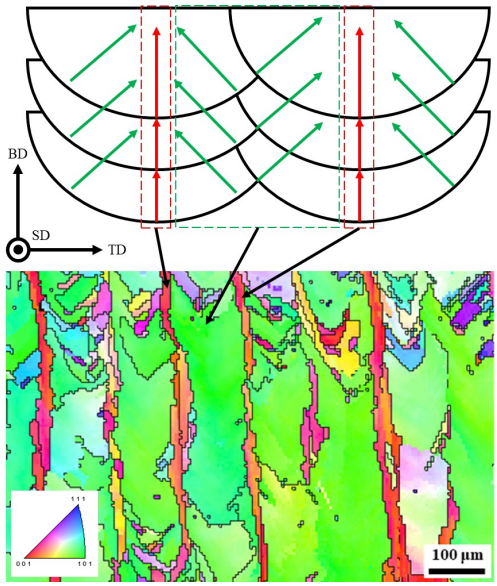


Figure 4.22: Grain growth mechanism that occurs in the top regions of both sample geometries.

It can be observed from Figure 4.22 that there are two main crystal growth di-

rections based on the thermal gradients that are present in the melt pools. The first direction is the thermal gradient in the build direction located at the center of the melt pool. This thermal gradient results in $< 001 >$ growth in the build direction. This growth mode combined with the thermal gradient in the scan direction, resulted in the formation of the cubic texture in these thin grains. With melt pools stacked right on top of one another and significant amounts of remelt of the previous layer, epitaxial growth takes place resulting in the formation of thin grains that extend up the build height. The other dominant thermal gradient is approximately 45 degrees from the build direction as depicted by green arrows in Figure 4.22. The other radial directions are not a factor because of remelt from the subsequent layer and epitaxial growth. Therefore, $< 001 >$ growth occurs 45° from the build direction causing the 45° rotated cubic texture.

It was observed that with decreases in the ILTI, the texture of the material strengthened. This result suggests that at least three different aspects of the build process factored into this texture strengthening; melt pool staggering, melt pool depth, and the temperature of the build, all of which influence the ratio of epitaxial growth versus heterogeneous nucleation occurs.

Melt pool staggering results in the misalignment of the melt pool centerlines. This misalignment does not favor epitaxial growth from the previous layer. Therefore, it is speculated that when there is an increased amount of melt pool staggering, there will be less epitaxial growth and more pronounced heterogeneous nucleation of new grains. This is observed in the bottom regions of both sample geometries and is depicted in Figure 4.23.

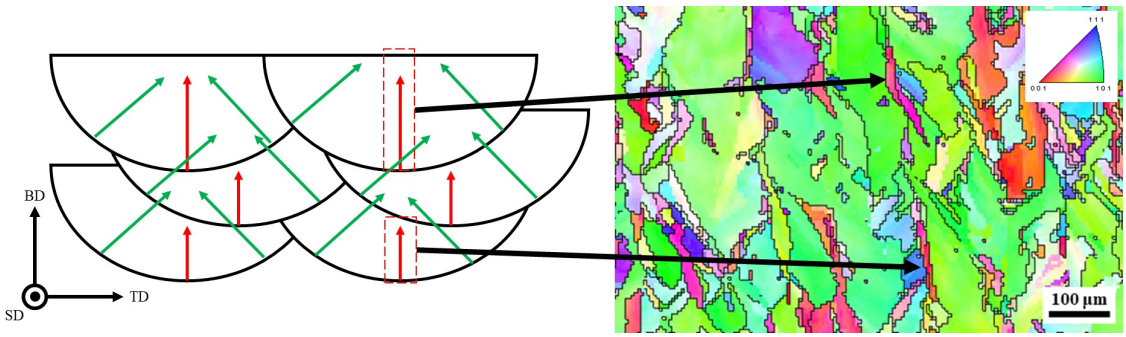


Figure 4.23: Grain growth/nucleation mechanism that occurs in the bottom regions of both sample geometries.

It can be observed from the melt pool depiction in Figure 4.23 that melt pool misalignment results in the thermal gradient in the build direction located at the centers of the melt pools to be staggered. This results in the termination of thin

grains with cubic texture instead of continued growth epitaxially up the build height. This is directly related to the EBSD data that was taken from a bottom region of the samples in this study, which were shown to have greater melt pool staggering. The decrease in epitaxial growth can result in the nucleation of new grains with different crystallographic orientation, resulting in a weaker texture. The amount of staggering can also have an effect on the grain size as mentioned in the previous subsection. With increased levels of heterogeneous nucleation of new grains the average grain size will decrease.

Melt pool depth affects both the amount of remelt and the angle of the thermal gradient. Andreau et al. state that at every layer there is a competition between heterogeneous nucleation of new grains following the thermal gradient, and the epitaxial growth of previously formed crystals [90]. The melt pool shape determines the angle of the thermal gradients, and Andreau et al. state that at low angular deviations, epitaxial growth is dominant. Therefore, if two subsequent melt pools are of similar shape, the angle of the thermal gradients will be similar and epitaxial growth will occur. However, if melt pool depths vary, the angles of the thermal gradients will vary, and nucleation of a new grain could occur. This thermal gradient misalignment is shown below in Figure 4.24. It can be seen that the melt pool highlighted in yellow is deeper than those surrounding it, causing its thermal gradients to have a different angle. This may provide additional insights regarding the random breaks in the rotated cube grains. When the melt pool shape is inconsistent, the angular deviation of the thermal gradient increases resulting in the directional nucleation of new grains.

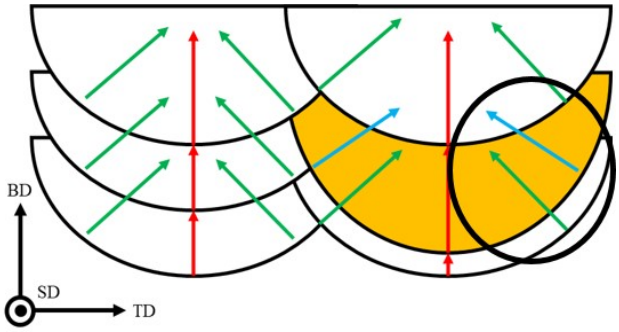


Figure 4.24: Diagram showing the effect that the melt pool shape has on the thermal gradients produced within the melt pools.

The temperature of the sample also plays a role in the amount of epitaxial growth that occurs. At higher temperatures the diffusion of an atom is made easier and can therefore organize into the same crystallographic orientation as the adjacent crystal. When the ILTI is decreased, there is more heat accumulation, resulting in higher

temperatures and higher atom mobility.

### 4.2.5 Composition and Mechanical Properties

The composition of a material manufactured using any AM process has the potential to experience alloy losses due to the high energy inputs. This material is not known to have these issues and the ILTI did not have any effect on the bulk composition, which was measured with EDS to be within specifications set for IN718.

Microhardness tests performed in the different ILTI regions showed an average microhardness of 315 HV0.2 over both of the tall rectangular prism samples and 319 HV0.2 over both of the triangular prism samples. In both sample types the microhardness was found to not change with variation of the ILTI. These values were comparable to literature, where Tucho et al. found as-printed samples to average about 300 HV depending on the samples' print orientation [62]. Amato et al. reported a hardness of around 385 HV (3.8/3.9 GPa) [68]. Chlebus et al. found the hardness to be 297 HV, 319 HV, and 322 HV, measured in the xy, xz, and yz-planes, respectively [65]. Popovich et al. report a hardness of 320 HV and 287 HV for laser sources of 250 W and 950 W, respectively [64]. Lastly, Jia and Gu report that with increasing the linear laser energy density from 180 J/m to 330 J/m the harness increases from 331.9 HV0.2 to 395.8 HV0.2 [26]. Even though there are some significant differences in the hardness found in literature based on the different process parameters, the hardness found in this study falls within this range.

In order to further characterize the effect that the ILTI has on the mechanical properties, tensile tests were performed. It was determined that there was no statistically significant difference in the yield strength, ultimate strength, and modulus of elasticity, however there was a slight difference in the elongations. The tensile samples manufactured with an ILTI of 59 seconds had a slightly lower elongation than tensile samples manufactured with a 126 second time interval. This difference was most likely due to a small difference in the amount of porosity, as discussed above. It should be noted that these tensile samples were not built in an orientation that took advantage of the strong texture directions, therefore texture strengthening is not expected to have played a role. It should also be noted that minimal variation was expected to be seen between the 59 and 126 second samples, since the all other material characteristics were relatively similar. The differences discussed in the previous sections were observed in the 13 second time interval region, however samples were not tested from this region in this study due to the complexity of the build

set-up. Future work will address this, in order to evaluate the mechanical behavior of a sample build with an ITLI of 13 seconds.

Overall, the tensile properties that were measured in this study were comparable to values found in literature. Literature values are summarized in Table 4.5. It can be seen that the tensile properties found in literature vary slightly. This is mainly due to all the different process parameters that go into an SLM build. One difference in process parameters can make a huge difference in the tensile properties. The tensile properties measured in this study, found in Table 4.3, fall within the ranges found in literature.

Table 4.5: Comparison of as-built SLM IN718 tensile properties found in literature.

| **Source** | **YS [MPa]** | **UTS [MPa]** | **E [GPa]** | **e [%]** |
|---|---|---|---|---|
| Wang [66] | 889-907 | 1137-1148 | 204 | 19.2-25.9 |
| Chlebus (Series B) [65] | 643±63 | 991±62 | 193±24 | 13±6 |
| Popovich (250 W) [64] | 668±16 | 1011±27 | 173±13 | 22±2 |

These tensile properties and hardness values are found to be slightly lower than both cast and wrought IN718 properties, however this is because these are as built samples and have not gone through post-process heat treatment. Heat treatment will allow for the precipitation of the strengthening phases $\gamma$' and $\gamma$", as well the the disolution of deleterious phases such as $\delta$ and laves.

As mentioned above, the tensile specimens in this study were not tested in an orientation that took advantage of either of the texture directions. These samples were tested 45 degrees from the $\{100\} < 001 >$ texture oriented in the scan direction. It is stated in literature that for a $\{111\} < 110 >$ slip system, crystallographic orientations near the $< 001 >$ direction are weaker than orientations near $< 111 >$ and/or $< 110 >$ [92, 93]. Therefore, in order to obtain the highest properties from these samples, they would have to be tested such that they are pulled along the build direction, with the $\{110\} < 001 >$ Goss texture.

# Chapter 5

# Conclusions

In this research the effect of the inter-layer time interval (ILTI) on the overall SLM build quality is investigated. Based on the results obtained, the following conclusions are drawn:

1. Melt pool staggering was found to be nearly eliminated in the top regions of both build geometries. The scan strategy should have resulted in melt pools one on top of the other, however this was not the case in the lower regions. It is speculated that the welding mode and the depth of penetration could effect the appearance of staggering, however more data is needed in order to definitively discern the cause for this.

2. Melt pool shape was found to change as the ILTI was varied. Melt pools were found to have a smaller radius of curvature at lower time intervals. It is believed that the smaller radius of curvature is indicative of a deeper melt pool that is no longer in the conduction welding mode. This was supported by the Eagra-Tsai model, where it was suggested that the melt pools of longer ILTIs were in conduction mode, while the melt pools of the 13 second ILTI were more consistent with the transition mode.

3. The grain size and shape was found to change as the ILTI was varied. There is a slight increase in the average grain area when the ILTI is decreased and the grains become more elongated in the build direction. This is attributed to the balance between epitaxial growth and homogeneous nucleation of new grains, which is shown to be affected by the degree of melt pool staggering and shape.

4. The crystallographic texture was found to strengthen as the ILTI was decreased.

This is attributed to the amount of epitaxial growth that occurs as opposed to the nucleation of new grains. The amount of epitaxial growth was found to be determined by the degree of melt pool staggering and the shape of the melt pool.

5. The amount of porosity was found to increase when the ILTI when from 59 to 13 seconds. This is attributed to the welding mode that occurs in each of the two cases. At an ILTI of 13 seconds the melt pools are suspected to have entered the transition welding mode, making them less stable and more prone to inducing porosity into the sample.

6. The variations in the material's bulk composition, hardness, and mechanical properties were statistically insignificant as the ILTI was changed. From this, it is suspected that strengthening phases were not precipitated nor was there any increase in deleterious phases during the SLM process.

From this research it is clear that the ILTI has an effect on the microstructure of SLM IN718. This is a process parameter that SLM users should be aware of in the future especially when making complex parts for aerospace use.

**Future Work**

In order to draw stronger conclusions, more research needs to be put into this topic. The following future work is suggested:

1. In order to eliminate the build height effects that could have potentially influenced the current samples, at minimum two more SLM builds are needed. The only difference between the two builds will be the number of samples on the build plate. The sample geometries will be remain the same with only the ILTI changing. The comparison of one sample from each new build plate will show the differences associated with the ILTI.

2. In order to further understand the effect of the ILTI on the mechanical properties, at least two new vertical builds are needed. This will allow the samples to be tested along directions exhibiting the strongest texture. The difference between the two builds will again be the number of samples in order to alter the ILTI and assess the effect of the shortest time interval.

3. In order to better understand the tensile properties and material hardness, further evaluation of the precipitate phases that arise during the SLM process of IN718, especially in different ILTI regions, is needed. This further analysis can be performed on both existing samples and new samples that are discussed above. The amounts of both strengthening and deleterious precipitate phases formed within the different ILTI regions will assist in explaining the potential differences in the tensile and hardness properties.

4. In order to determine the exact ILTI at which these microstructural differences begin to occur, multiple builds will be needed. In this research the it is determined that these differences occur somewhere between 39 seconds and 13 seconds. Obtaining samples with ILTI times between this range will help narrow down the time at which these differences occur.

5. In order to fully understand the melt pool staggering that was seen in this research, an open source SLM machine can be used, giving full control over the scan strategy. This will eliminate concerns that the machine is inducing this staggering and allow for the root cause to be determined.

6. In order to have a better understanding about the heat accumulation that occurs due to a smaller ILTI, thermal data should be recorded during the build process. This can be done with either thermocouples on the base plate, or using thermal imaging. Analysis using thermal imaging can give insight into the effect of local heating from an adjacent scan track versus the bulk heating from layer to layer.

# Bibliography


[1] Paul R. Gradl, Sandy E. Greene, Christopher Protz, Brad Bullard, James Buzzell, Chance Garcia, Jessica Wood, Robin Osborne, James Hulka, and Kenneth G. Cooper. *Additive Manufacturing of Liquid Rocket Engine Combustion Devices: A Summary of Process Developments and Hot–Fire Testing Results.* 2018 Joint Propulsion Conference, July 2018.

[2] Robert Schafrik and Robert Spraque. Saga of gas turbine materials: Part iii. *Advanced Materials and Processes*, 162:29–33, May 2004.

[3] Tresa M. Pollock and Sammy Tin. Nickel-based superalloys for advanced turbine engines: Chemistry, microstructure and properties. *Journal of Propulsion and Power*, 22:361–374, March 2006.

[4] Matthew J. Donachie and S. Donachie. *Superalloys: A Technical Guide.* ASM International, 2002.

[5] Dunyong Deng. *Additively Manufactured Inconel 718 : Microstructures and Mechanical Properties.* 01 2018.

[6] D.F. Paulonis and J.J. Schirra. Alloy 718 at Pratt & Whitney: Historical Perspective and Future Challenges. volume 1, pages 13–23. TMS, 01 2001.

[7] J.R. Davis and A.S.M.I.H. Committee. *Nickel, Cobalt, and Their Alloys.* ASM specialty handbook. ASM International, 2000.

[8] ASTM B670-07. *Standard Specification for Precipitation-Hardening Nickel Alloy (UNS N07718) Plate, Sheet, and Strip for High-Temperature Service.* ASTM International, West Conshohocken, PA, 2018.

[9] Metallic Materials Properties Development and Standardization (MMPDS). *Chapter 6 - Heat-Resistant Alloys.* BMI - Battelle Memorial Institute, 2017.

[10] J Zhao. *The Use of Ceramic Matrix Composites for Metal Cutting Applications*, pages 537–569. 02 2014.

[11] Terry Wohlers and Tim Gornet. History of additive manufacturing. *Wohlers Report 2016*, 2016.

[12] ISO/ASTM 52900:2015(E). *Standard Terminology for Additive Manufacturing - General Principles*. ASTM International, West Conshohocken, PA, 2015.

[13] F. Calignano, D. Manfredi, E. P. Ambrosio, S. Biamino, M. Lombardi, E. Atzeni, A. Salmi, P. Minetola, L. Iuliano, and P. Fino. Overview on additive manufacturing technologies. *Proceedings of the IEEE*, 105(4):593–612, April 2017.

[14] Tracy McMahan. NASA 3-D Prints First Full-Scale Copper Rocket Engine Part, April 2015. [Online; updated August 2017].

[15] GE Additive. New manufacturing milestone: 30,000 additive fuel nozzles, October 2018.

[16] Timothy J. Horn and Dr Ola L. A. Harrysson. Overview of current additive manufacturing technologies and selected applications. *Science Progress*, 95(3):255–282, 2012.

[17] P.D. Olson. 100,000 Patients Later, The 3D-Printed Hip is a Decade Old and Going Strong, March 2018.

[18] T. Monaghan, A.J. Capel, S.D. Christie, R.A. Harris, and R.J. Friel. Solid-state additive manufacturing for metallized optical fiber integration. *Composites Part A: Applied Science and Manufacturing*, 76:181 – 193, 2015.

[19] C.Y Kong, R.C Soar, and P.M Dickens. Optimum process parameters for ultrasonic consolidation of 3003 aluminium. *Journal of Materials Processing Technology*, 146(2):181 – 187, 2004.

[20] William E. Frazier. Metal additive manufacturing: A review. *Journal of Materials Engineering and Performance*, 23(6):1917–1928, Jun 2014.

[21] John O. Milewski. *Additive Manufacturing of Metal: From Fundamental Understanding Technology to Rocket Nozzles, Medical Implants, and Custom Jewelry*. Springer, 2017.

[22] Mostafa Yakout, Andrea Cadamuro, M. A. Elbestawi, and Stephen C. Veldhuis. The selection of process parameters in additive manufacturing for aerospace alloys. *INTERNATIONAL JOURNAL OF ADVANCED MANUFACTURING TECHNOLOGY*, 92(5-8):2081 – 2098, n.d.

[23] Haijun Gong, Khalid Rafi, Hengfeng Gu, Thomas Starr, and Brent Stucker. Analysis of defect generation in ti6al4v parts made using powder bed fusion additive manufacturing processes. *Additive Manufacturing*, 1-4:87 – 98, 2014. Inaugural Issue.

[24] Umberto Scipioni Bertoli, Alexander J. Wolfer, Manyalibo J. Matthews, Jean-Pierre R. Delplanque, and Julie M. Schoenung. On the limitations of volumetric energy density as a design parameter for selective laser melting. *Materials & Design*, 113:331 – 340, 2017.

[25] Joaquim Ciurana, Luis Hernandez, and Jordi Delgado. Energy density analysis on single tracks formed by selective laser melting with cocrmo powder material. *The International Journal of Advanced Manufacturing Technology*, 68(5):1103–1110, Sep 2013.

[26] Qingbo Jia and Dongdong Gu. Selective laser melting additive manufacturing of inconel 718 superalloy parts: Densification, microstructure and properties. *Journal of Alloys and Compounds*, 585:713 – 721, 2014.

[27] Eurico Assuncao, Stewart Williams, and David Yapp. Interaction time and beam diameter effects on the conduction mode limit. *Optics and Lasers in Engineering*, 50(6):823 – 828, 2012.

[28] Luke N. Carter, Christopher Martin, Philip J. Withers, and Moataz M. Attallah. The influence of the laser scan strategy on grain structure and cracking behaviour in slm powder-bed fabricated nickel superalloy. *Journal of Alloys and Compounds*, 615:338 – 347, 2014.

[29] Yanjin Lu, Songquan Wu, Yiliang Gan, Tingting Huang, Chuanguang Yang, Lin Junjie, and Jinxin Lin. Study on the microstructure, mechanical property and residual stress of slm inconel-718 alloy manufactured by differing island scanning strategy. *Optics & Laser Technology*, 75:197 – 206, 2015.

[30] A.M. Mancisidor, F. Garciandia, M. San Sebastian, P. lvarez, J. Daz, and I. Unanue. Reduction of the residual porosity in parts manufactured by selective

laser melting using skywriting and high focus offset strategies. *Physics Procedia*, 83:864 – 873, 2016. Laser Assisted Net Shape Engineering 9 International Conference on Photonic Technologies Proceedings of the LANE 2016 September 19-22, 2016 Frth, Germany.

[31] Fabian Geiger, Karsten Kunze, and Thomas Etter. Tailoring the texture of in738lc processed by selective laser melting (slm) by specific scanning strategies. *Materials Science and Engineering: A*, 661:240 – 246, 2016.

[32] Shi-Hai Sun, Koji Hagihara, and Takayoshi Nakano. Effect of scanning strategy on texture formation in ni-25at.alloys fabricated by selective laser melting. *Materials & Design*, 140:307 – 316, 2018.

[33] Wei Chen. Effect of the particle size of 316l stainless steel on the corrosion characteristics of the steel fabricated by selective laser melting. *International Journal of Electrochemical Science*, 13:10217–10232, 11 2018.

[34] Lawrence E. Murr, Edwin Martinez, Jennifer Hernandez, Shane Collins, Krista N. Amato, Sara M. Gaytan, and Patrick W. Shindo. Microstructures and properties of 17-4 ph stainless steel fabricated by selective laser melting. *Journal of Materials Research and Technology*, 1(3):167 – 177, 2012.

[35] Chantal K. Sudbrack, Bradley A. Lerch, Timothy M. Smith, Ivan E. Locci, David L. Ellis, Aaron C. Thompson, and Benjamin Richards. Impact of powder variability on the microstructure and mechanical behavior of selective laser melted alloy 718. In Eric Ott, Xingbo Liu, Joel Andersson, Zhongnan Bi, Kevin Bockenstedt, Ian Dempster, Jon Groh, Karl Heck, Paul Jablonski, Max Kaplan, Daisuke Nagahama, and Chantal Sudbrack, editors, *Proceedings of the 9th International Symposium on Superalloy 718 & Derivatives: Energy, Aerospace, and Industrial Applications*, pages 89–113, Cham, 2018. Springer International Publishing.

[36] G. Yablokova, M. Speirs, J. Van Humbeeck, J.-P. Kruth, J. Schrooten, R. Cloots, F. Boschini, G. Lumay, and J. Luyten. Rheological behavior of -ti and niti powders produced by atomization for slm production of open porous orthopedic implants. *Powder Technology*, 283:199 – 209, 2015.

[37] Rustam Baitimerov, Pavel Lykov, Dmitry Zherebtsov, Ludmila Radionova, Alexey Shultc, and Konda Gokuldoss Prashanth. Influence of powder charac-

teristics on processability of alsi12 alloy fabricated by selective laser melting. *Materials*, 11(5), 2018.

[38] Maurizio Iebba, Antonello Astarita, Daniela Mistretta, Ivano Colonna, Mariacira Liberini, Fabio Scherillo, Carmine Pirozzi, Rosario Borrelli, Stefania Franchitti, and Antonino Squillace. Influence of powder characteristics on formation of porosity in additive manufacturing of ti-6al-4v components. *Journal of Materials Engineering and Performance*, 26(8):4138–4147, Aug 2017.

[39] B. Ferrar, L. Mullen, E. Jones, R. Stamp, and C.J. Sutcliffe. Gas flow effects on selective laser melting (slm) manufacturing performance. *Journal of Materials Processing Technology*, 212(2):355 – 364, 2012.

[40] Ahmad Bin Anwar and Quang-Cuong Pham. Selective laser melting of alsi10mg: Effects of scan direction, part placement and inert gas flow velocity on tensile strength. *Journal of Materials Processing Technology*, 240:388 – 396, 2017.

[41] Tomasz Kurzynowski, Edward Chlebus, Bogumia Kunicka, and Jacek Reiner. Parameters in selective laser melting for processing metallic powders. *Proceedings of SPIE*, 8239:823914, 02 2012.

[42] X.J. Wang, L.C. Zhang, M.H. Fang, and T.B. Sercombe. The effect of atmosphere on the structure and properties of a selective laser melted al12si alloy. *Materials Science and Engineering: A*, 597:370 – 375, 2014.

[43] S. Dadbakhsh, L. Hao, and N. Sewell. Effect of selective laser melting layout on the quality of stainless steel parts. *Rapid Prototyping Journal*, 18(3):241–249, 2012.

[44] E. Fitzgerald and W. Everhart. The effect of location on the structure and mechanical properties of selective laser melted 316l stainless steel. 2016 Solid Freeform Fabrication Symposium, 2016.

[45] Fude Wang. Mechanical property study on rapid additive layer manufacture hastelloy x alloy by selective laser melting technology. *The International Journal of Advanced Manufacturing Technology*, 58(5):545–551, Jan 2012.

[46] Bi Zhang, Yongtao Li, and Qian Bai. Defect formation mechanisms in selective laser melting: A review. *Chinese Journal of Mechanical Engineering*, 30(3):515–527, May 2017.

[47] Nicholas P.; Khairallah Saad A.; Wang Jenny; Depond Phillip J.; Fong Anthony Y.; Thampy Vivek; Guss Gabe M.; Kiss Andrew M.; Stone Kevin H.; Tassone Christopher J.; Nelson Weker Johanna; Toney Michael F.; van Buuren Tony; Matthews Manyalibo J. Martin, Aiden A.; Calta. Dynamics of pore formation during laser powder bed fusion additive manufacturing. *Nature Communications*, 1987:87 – 98, 2019.

[48] Lijin Huang, Xueming Hua, Dongsheng Wu, and Fang Li. Numerical study of keyhole instability and porosity formation mechanism in laser welding of aluminum alloy and steel. *Journal of Materials Processing Technology*, 252:421 – 431, 2018.

[49] Ruidi Li, Jinhui Liu, Yusheng Shi, Li Wang, and Wei Jiang. Balling behavior of stainless steel and nickel powder during selective laser melting process. *The International Journal of Advanced Manufacturing Technology*, 59(9):1025–1035, Apr 2012.

[50] Ruidi Li, Yusheng Shi, Zhigang Wang, Li Wang, Jinhui Liu, and Wei Jiang. Densification behavior of gas and water atomized 316l stainless steel powder during selective laser melting. *Applied Surface Science*, 256(13):4350 – 4356, 2010.

[51] Kun V. Yang, Paul Rometsch, Tom Jarvis, Jeremy Rao, Sheng Cao, Chris Davies, and Xinhua Wu. Porosity formation mechanisms and fatigue response in al-si-mg alloys made by selective laser melting. *Materials Science and Engineering: A*, 712:166 – 174, 2018.

[52] Dongdong Gu, Yves-Christian Hagedorn, Wilhelm Meiners, Guangbin Meng, Rui Joo Santos Batista, Konrad Wissenbach, and Reinhart Poprawe. Densification behavior, microstructure evolution, and wear performance of selective laser melting processed commercially pure titanium. *Acta Materialia*, 60(9):3849 – 3860, 2012.

[53] Yang Liu, Yongqiang Yang, and Di Wang. A study on the residual stress during selective laser melting (slm) of metallic powder. *The International Journal of Advanced Manufacturing Technology*, 87(1):647–656, Oct 2016.

[54] Xiaoming Zhao, Xin Lin, Jing Chen, Lei Xue, and Weidong Huang. The effect of hot isostatic pressing on crack healing, microstructure, mechanical properties

of rene88dt superalloy prepared by laser solid forming. *Materials Science and Engineering: A*, 504(1):129 – 134, 2009.

[55] Johannes Gnther, Stefan Leuders, Peter Koppa, Thomas Trster, Sebastian Henkel, Horst Biermann, and Thomas Niendorf. On the effect of internal channels and surface roughness on the high-cycle fatigue performance of ti-6al-4v processed by slm. *Materials & Design*, 143:1 – 11, 2018.

[56] Anton Jansson, Amir Reza Zekavat, and L Pejryd. Measurement of internal features in additive manufactured components by the use of computed tomography. 06 2015.

[57] Karolien Kempen. Dimensional accuracy of internal channels in slm produced parts. 04 2014.

[58] Xiaoqing Wang, Xibing Gong, and Kevin Chou. Review on powder-bed laser additive manufacturing of inconel 718 parts. *Proceedings of the Institution of Mechanical Engineers, Part B: Journal of Engineering Manufacture*, 231(11):1890–1903, 2017.

[59] K. Moussaoui, W. Rubio, M. Mousseigne, T. Sultan, and F. Rezai. Effects of selective laser melting additive manufacturing parameters of inconel 718 on porosity, microstructure and mechanical properties. *Materials Science and Engineering: A*, 735:182 – 190, 2018.

[60] Brooke Sarley, Albert C. Manero, Jose Cotelo, Janine Wischek, John Okasinski, Peter Kenesei, Jon Almer, Marion Bartsch, and Seetha Raghavan. Real-time evolution of selective laser melted (slm) inconel 718 with temperature through synchrotron x-rays. 01 2017.

[61] Tahira Raza, Joel Andersson, and Lars-Erik Svensson. Microstructure of selective laser melted alloy 718 in as-manufactured and post heat treated condition. *Procedia Manufacturing*, 25:450 – 458, 2018. Proceedings of the 8th Swedish Production Symposium (SPS 2018).

[62] Wakshum M. Tucho, Priscille Cuvillier, Atle Sjolyst-Kverneland, and Vidar Hansen. Microstructure and hardness studies of inconel 718 manufactured by selective laser melting before and after solution heat treatment. *Materials Science and Engineering: A*, 689:220 – 232, 2017.

[63] Naresh Nadammal, Sandra Cabeza, Tatiana Mishurova, Tobias Thiede, Arne Kromm, Christoph Seyfert, Lena Farahbod, Christoph Haberland, Judith Ann Schneider, Pedro Dolabella Portella, and Giovanni Bruno. Effect of hatch length on the development of microstructure, texture and residual stresses in selective laser melted superalloy inconel 718. *Materials & Design*, 134:139 – 150, 2017.

[64] V.A. Popovich, E.V. Borisov, A.A. Popovich, V.Sh. Sufiiarov, D.V. Masaylo, and L. Alzina. Impact of heat treatment on mechanical behaviour of inconel 718 processed with tailored microstructure by selective laser melting. *Materials & Design*, 131:12 – 22, 2017.

[65] E. Chlebus, K. Gruber, B. Kunicka, J. Kurzac, and T. Kurzynowski. Effect of heat treatment on the microstructure and mechanical properties of inconel 718 processed by selective laser melting. *Materials Science and Engineering: A*, 639:647 – 655, 2015.

[66] Zemin Wang, Kai Guan, Ming Gao, Xiangyou Li, Xiaofeng Chen, and Xiaoyan Zeng. The microstructure and mechanical properties of deposited-in718 by selective laser melting. *Journal of Alloys and Compounds*, 513:518 – 523, 2012.

[67] Xibing Gong, Xiaoqing Wang, Zachary Jones, Kenneth Cooper, Vernon Cole, and Kevin Chou. Characterization of microstructure and mechanical property of inconel 718 from selective laser melting. 01 2015.

[68] K.N. Amato, S.M. Gaytan, L.E. Murr, E. Martinez, P.W. Shindo, J. Hernandez, S. Collins, and F. Medina. Microstructures and mechanical behavior of inconel 718 fabricated by selective laser melting. *Acta Materialia*, 60(5):2229 – 2239, 2012.

[69] L. Costa, R. Vilar, T. Reti, and A.M. Deus. Rapid tooling by laser powder deposition: Process simulation using finite element analysis. *Acta Materialia*, 53(14):3987 – 3999, 2005.

[70] Aref Yadollahi, Nima Shamsaei, Scott M. Thompson, and Denver W. Seely. Effects of process time interval and heat treatment on the mechanical and microstructural properties of direct laser deposited 316l stainless steel. *Materials Science and Engineering: A*, 644:171 – 183, 2015.

[71] Brian Torries and Nima Shamsaei. Fatigue behavior and modeling of additively manufactured ti-6al-4v including interlayer time interval effects. *JOM*, 69(12):2698–2705, Dec 2017.

[72] Yashwanth Kumar Bandari, Yousub Lee, Peeyush Nandwana, Bradley S. Richardson, Adeola I. Adediran, Lonnie J. Love, and Katherine T. Gaul. Effect of inter-layer cooling time on distortion and mechanical properties in metal additive manufacturing (am).

[73] Erik R. Denlinger, Jarred C. Heigel, Pan Michaleris, and T.A. Palmer. Effect of inter-layer dwell time on distortion and residual stress in additive manufacturing of titanium and nickel alloys. *Journal of Materials Processing Technology*, 215:123 – 131, 2015.

[74] Mohamad Mahmoudi, Alaa Elwany, Aref Yadollahi, Scott M. Thompson, Linkan Bian, and Nima Shamsaei. Mechanical properties and microstructural characterization of selective laser melted 17-4 ph stainless steel. *Rapid Prototyping Journal*, 23, 2017.

[75] George Vander Voort and Elena Manilova. Metallographic techniques for superalloys. *Microscopy and Microanalysis - MICROSC MICROANAL*, 10, 08 2004.

[76] ASTM F3055-14a. *Standard Specification for Additive Manufacturing Nickel Alloy (UNS N07718) with Powder Bed Fusion*. ASTM International, West Conshohocken, PA, 2014.

[77] ASTM E8/8M-16a. *Standard Test Methods for Tension Testing of Metallic Materials*. ASTM International, West Conshohocken, PA, 2016.

[78] Pan Tao, Huaixue Li, Baiying Huang, Quandong Hu, Shuili Gong, and Qingyan Xu. The crystal growth, intercellular spacing and microsegregation of selective laser melted inconel 718 superalloy. *Vacuum*, 159:382 – 390, 2019.

[79] Erica L. Stevens, Jakub Toman, Albert C. To, and Markus Chmielus. Variation of hardness, microstructure, and laves phase distribution in direct laser deposited alloy 718 cuboids. *Materials & Design*, 119:188 – 198, 2017.

[80] D. Rosenthal. *The Theory of Moving Sources of Heat and Its Application to Metal Treatments*. ASME, 1946.

[81] T.W. Eagar and N.S. Tsai. Temperature fields produced by traveling distributed heat sources. *Weld. Res. Suppl.; (United States)*.

[82] Elham Mirkoohi, Daniel E. Sievers, Hamid Garmestani, Kuoning Chiang, and Steven Y. Liang. Three-dimensional semi-elliptical modeling of melt pool geometry considering hatch spacing and time spacing in metal additive manufacturing. *Journal of Manufacturing Processes*, 45:532 – 543, 2019.

[83] I.A. Roberts, C.J. Wang, R. Esterlein, M. Stanford, and D.J. Mynors. A three-dimensional finite element analysis of the temperature field during laser melting of metal powders in additive layer manufacturing. *International Journal of Machine Tools and Manufacture*, 49(12):916 – 923, 2009.

[84] Dongyun Zhang, Pudan Zhang, Zhen Liu, Zhe Feng, Chengjie Wang, and Yanwu Guo. Thermofluid field of molten pool and its effects during selective laser melting (slm) of inconel 718 alloy. *Additive Manufacturing*, 21:567 – 578, 2018.

[85] Ming Tang, P. Chris Pistorius, and Jack L. Beuth. Prediction of lack-of-fusion porosity for powder bed fusion. *Additive Manufacturing*, 14:39 – 48, 2017.

[86] Jitka Metelkova, Yannis Kinds, Karolien Kempen, Charlotte de Formanoir, Ann Witvrouw, and Brecht Van Hooreweder. On the influence of laser defocusing in selective laser melting of 316l. *Additive Manufacturing*, 23:161 – 169, 2018.

[87] Patcharapit Promoppatum, Shi-Chune Yao, P. Chris Pistorius, and Anthony D. Rollett. A comprehensive comparison of the analytical and numerical prediction of the thermal history and solidification microstructure of inconel 718 products made by laser powder-bed fusion. *Engineering*, 3(5):685 – 694, 2017.

[88] John Romano, Leila Ladani, and Magda Sadowski. Laser additive melting and solidification of inconel 718: Finite element simulation and experiment. *JOM*, 68(3):967–977, Mar 2016.

[89] Ting Qi, Haihong Zhu, Hu Zhang, Jie Yin, Linda Ke, and Xiaoyan Zeng. Selective laser melting of al7050 powder: Melting mode transition and comparison of the characteristics between the keyhole and conduction mode. *Materials & Design*, 135:257 – 266, 2017.

[90] Olivier Andreau, Imade Koutiri, Patrice Peyre, Jean-Daniel Penot, Nicolas Saintier, Etienne Pessard, Thibaut De Terris, Corinne Dupuy, and Thierry Baudin.

Texture control of 316l parts by modulation of the melt pool morphology in selective laser melting. *Journal of Materials Processing Technology*, 264:21 – 31, 2019.

[91] H.Y. Wan, Z.J. Zhou, C.P. Li, G.F. Chen, and G.P. Zhang. Effect of scanning strategy on grain structure and crystallographic texture of inconel 718 processed by selective laser melting. *Journal of Materials Science & Technology*, 34(10):1799 – 1804, 2018.

[92] Wesley A. Tayon, Ravi N. Shenoy, MacKenzie R. Redding, R. Keith Bird, and Robert A. Hafley. Correlation Between Microstructure and Mechanical Properties in an Inconel 718 Deposit Produced Via Electron Beam Freeform Fabrication. *Journal of Manufacturing Science and Engineering*, 136(6), 10 2014.

[93] Dong Ma, Alexandru D. Stoica, Zhuqing Wang, and Allison M. Beese. Crystallographic texture in an additively manufactured nickel-base superalloy. *Materials Science and Engineering: A*, 684:47 – 53, 2017.

# Appendix A

# Drawings

This appendix provides the engineering drawings for the seeded defect cube featured in this thesis. The dimensions here are in inches and give information of the exact locations and size of each defect.

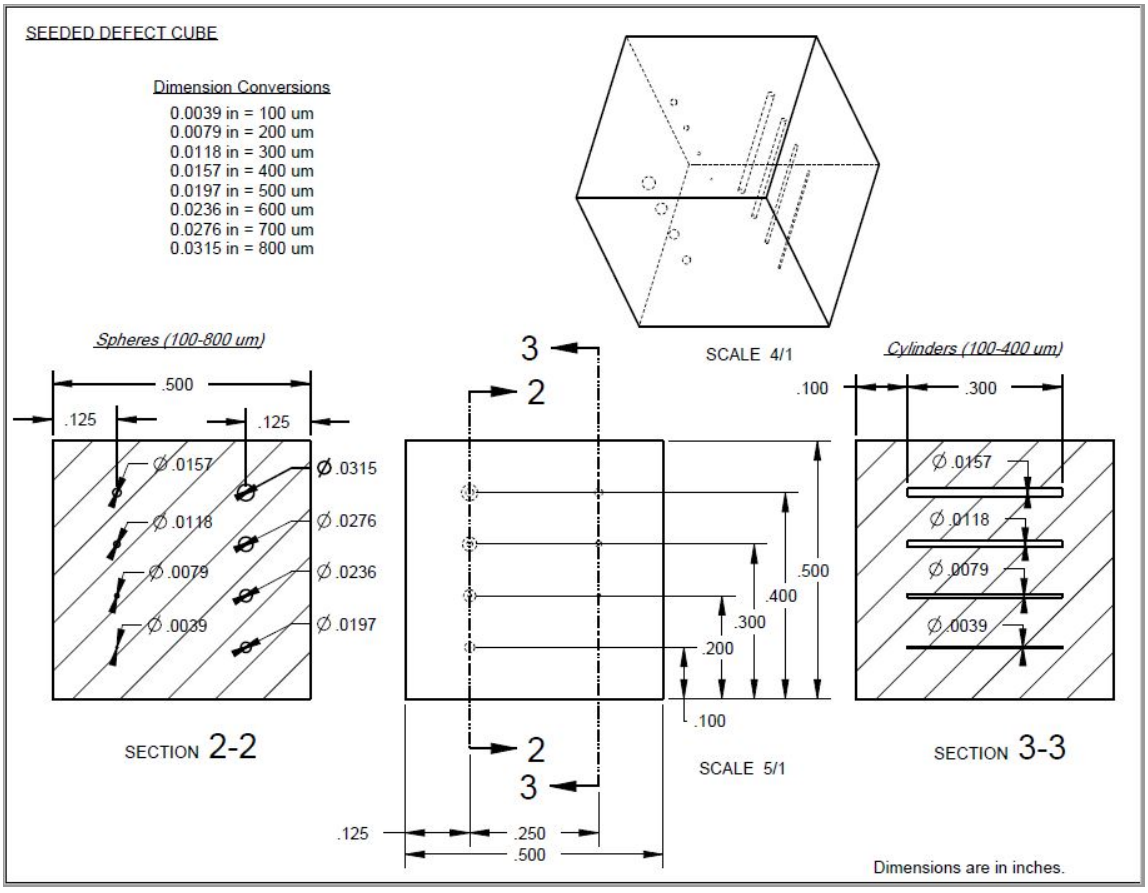


Figure A.1: Seeded defect cube drawing.